Deposition and Analysis of Thin Films
FB502

2018

Contents

Preface

The presented text is intended for the same-named course for postgraduate students of Plasma Physics. The chapters consist of a brief presentation of the physical background, fundamental properties, strengths and weaknesses of different deposition and analysis methods and techniques available at the Department of Physical Electronics at the Faculty of Science of the Masaryk University.

Part I

Deposition methods

Thin film deposition process can be generally described as happening in three consecutive steps [1]:

1. **Creation of gaseous phase of the deposited material.** Several different ways of gaseous phase generation can be utilized, such as evaporation, sputtering or applying of chemical gases and vapours.

2. **Vapour transport from source to substrate.** Atoms, atomic clusters or molecules of the deposited material can be transported either in ballistic mode (mutual collisions and collisions with background gas atoms can be neglected) and/or in diffusion/thermal mode (collisions during the transport can not be neglected). Crossover between these modes is not sharp and the transport mode may not be easily distinguished.

3. **Film growth on the substrate.** This step accounts for the growth process of the film from the first nucleation to a continuous film. The composition and microstructure of the film can be affected by impinging ion bombardment of the growing film during the deposition.

The deposition methods are usually divided into two branches depending on the specific way of obtaining the gaseous phase of the deposited material from the source. These two branches are PVD (*Physical Vapour Deposition*) methods and CVD (*Chemical Vapour Deposition*) methods.

PVD methods are atomistic in nature. The coating is deposited from individual atoms or their small clusters and the reactions take place on the substrate.
PVD methods:

- vacuum evaporation — deposited material is placed in a vacuum chamber and resistively heated until evaporation occurs
- sputtering — deposited material is sputtered from a target by energetic ions supplied by an electric discharge
- pulsed laser deposition — deposited material is evaporated using high power laser beam
- electron beam deposition — deposited material is evaporated using energetic electron beam
- cathode arc deposition — material of the cathode is evaporated by high-current low-voltage arc discharge

CVD methods are characterized by chemical reactions of molecules in the volume as well as on the substrate surface. The temperatures needed for

activation of chemical reactions are often in the range of 800 – 1000 °C. CVD methods:

- atmospheric pressure CVD — chemical vapour depositions at high pressures and generally high temperatures
- atomic layer epitaxy/deposition — continual deposition of crystalline monolayers from gas precursor(s) copying the crystalline structure of the substrate or previous layer
- plasma enhanced CVD — CVD, where the energy needed for chemical reactions is supplied by a discharge, temperatures can be closer to ambient level

Chapter 1

Magnetron sputtering

Mgr. Pavel Souček, Ph.D.

1.1 Sputtering principle

The basic physical principle of sputtering is knocking out of atoms from a cathode (also called target) by incident energetic particles [2]. The sputter yield Y is defined as the ratio of the number of particles ejected from the cathode (target) to the number of incident bombarding particles:

$$Y = \frac{\text{number of ejected particles}}{\text{number of incident particles}} \tag{1.1}$$

Sputtering can result from bombardment with a variety of incident species. The most commonly used are inert gas ions (e.g. Ar^+), but use of other species such as neutrals, electrons or photons is possible.

The sputtering process consists of kinetic collisions — first between the incident energetic particle and one or a few atoms of the target, and then subsequent collisions between the atoms of the target (so called collision cascades). The kinetic energy and the momentum of the incident particle are redistributed to the target atoms. If, during the last interaction, the momentum direction is oriented in an outward direction from the surface of the target and enough energy is supplied to the atom to break the bonds with other atoms, sputtering occurs (see Fig. 1.1).

Depending on the kinetic energy of the incident particle, different physical results can occur [3]:

- *Low energy* (0 eV $< E <$ 20 – 50 eV) This regime is known as *sub-threshold regime*. The energy of incident particles is too low to sputter the target. For a long time, it was observed that sputtering seemed to have a threshold of $\sim$ 40 eV for most materials, below which no sputtering occurred. This was due to dramatic fall-off in the sputtering

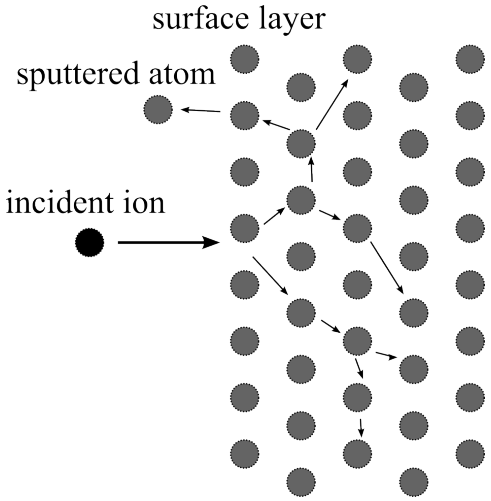

Figure 1.1: Principle of sputtering.

yield as the incident particle energy decreases. Experimentally a low intensity sputtering was observed in dense plasma such as ECR. The sputtering yield is very low — in the order of 10^{-6}.

- *Moderate energy* (50 eV $< E <$ 1000 eV) This range is also called the *knock-on sputtering regime*. It covers most of the practical applications in PVD. The incident particle impacts a target atom, which recoils and strikes one or more atoms, which recoil and the process continues. The sequence of collisions will differ greatly for each incoming particle because each particle will hit in a different place with regard to the specific position of surrounding atoms. The sputter yield depends strongly on the incident particle mass (more exactly on the ratio of incident particle mass to the target atom mass) and the kinetic energy, as well as on the target orientation. The target temperature does not play a crucial effect in the sputtering yield as long as it is not close to the melting temperature of the target material [4, 5].

- *High energy* (1 keV $< E <$ 50 keV) The incident particle causes a dense cascade of secondary particles (target atoms) after the initial impact. Within this cascade volume, all of the bonds between the particles are broken and the region can be treated with statistical mechanics.

- *Very high energy* ($E >$ 50 keV) At these energies, the incident particle penetrates deep into the target many atomic layers before causing a significant number of collisions and is effectively implanted into the bulk of the target. The volume of the material affected by the collisions lies deep in the target and only a few if any target atoms are sputtered.

The sputtering yields of materials of interest can be found in tables [6], papers dealing with similar elements (such as carbon [7]) or can be simulated for example by the SRIM/TRIM program [8] based Monte Carlo simulation method.

Since the basic principle of magnetron sputtering is the momentum and energy transfer between the incident particle and the target atoms, the particular species used are of great importance. The first reason is that the binding energy of the target atoms differers for different target atoms species. A general trend of higher sputtering yields for materials with low binding energies and a correlation between low binding energy and low melting point materials is observed [3]. The second reason is that the momentum transfer efficiency corresponds to the ratio of mass of the incident particle and the mass of the target atom $m_{incident}/M_{target}$. Therefore the momentum transport is most efficient for incident and target atoms of the same species (*self-sputtering*), whereas it is inefficient (hence the sputtering yield is low) if the incident and the target atoms are strongly mismatched in the atomic mass. Self-sputtering mode can be employed in DC sputtering [9, 10] and is of major concern in HiPIMS discharges [11].

1.2 Transport of sputtered atoms, gas rarefaction

The type of sputtered atoms transport is governed by the configuration of the sputtering device and the working pressure, particularly by the comparison of the target-to-substrate distance and the mean free path of the sputtered particle [12, 13].

If the pressure is low enough, the sputtered particle does not undergo significant number of collisions, if any. Thus it arrives at the deposition surface with near the original kinetic energy. This transport mode is called *ballistic* transport. Films deposited in this transport mode are generally small grained and dense, they also often have good adhesion to the substrate and show compressive stress. Ballistic transport is also directional, this can be utilized with directional filtering. Ballistic deposition is preferred for industrial applications [3].

At higher pressures the sputtered atom undergoes a significant number of collisions and quickly looses its initial kinetic energy. This mode is known as *diffusive* or *thermal* transport. The sputtered atoms progressively loose energy and get cooler while the background gas is heated. Thermalized deposition can lead to significantly different films compared with ballistic depositions. The main reason is that the incident sputtered atoms arrive on the deposition surface with virtually no kinetic energy [14]. Films prepared by thermalized depositions show similar features to those prepared by evap-

oration — in both the grain size and the stress. Compared with the ballistic depositions the grain size is generally larger and the stress is more tensile.

The temperature of the background gas can increase quite significantly especially in the volume in the vicinity of the target. As hot gas atoms leave the volume in the vicinity of the target faster than cooler gas atoms arrive from further away, local *gas rarefaction* can occur. This phenomenon can be quite significant and can decrease the original gas density down to as low as 15 % of the original value [15]. Gas rarefaction can be an important factor in scaling issues — high rate sputtering may have similar characteristics to low pressure sputtering, while low sputtering yield processes at moderate pressures can be significantly different as the sputtering power is scaled up and the effective gas density is reduced. Gas rarefaction can also be modelled by Monte Carlo method [16, 17]. Gas rarefaction does significantly influence especially HiPIMS discharges, where high power is delivered in a short time [18]. It can lead to draining of charge carriers and switch to a DCMS-like regime [19] and to changes in transport processes during deposition [20].

1.3 Planar magnetron

The aforementioned basic sputtering principle in section 1.1 is valid regardless of the presence or absence of a magnetic field at the sputtered cathode. This sputtering design consisting only of an anode and a cathode without the presence of any magnetic field is the so called diode sputtering and is limited by low deposition rate, low ionization efficiency in the plasma and strong substrate heating [3].

Magnetron sputtering enhances diode sputtering by adding a magnetic field parallel to the cathode surface [21]. The magnets are arranged in a way that one pole of the magnet is in the centre of the cathode and the other pole is composed of magnets arranged on the outer edge of the target. The Lorentz force, given by the cross product of the electric and magnetic field $\boldsymbol{F} = \mathrm{e}\boldsymbol{E} \times \boldsymbol{B}$, is used to trap the electrons in the vicinity of the target. In the case of magnetron sputtering $\boldsymbol{E}$ is perpendicular to the target surface and applying $\boldsymbol{B}$ tangentially to the surface gives rise to electron velocity parallel to the target surface (so called $\boldsymbol{E} \times \boldsymbol{B}$ drift). The electrons undergo a cycloidal motion along the orbit path and can ionize the gas on a longer trajectory.

Fig. 1.2 depicts a typical magnetron configuration with magnets confining electrons into an annular closed path, which gives rise to an annulus of intensive plasma region. This results in an uneven erosion of the target material — a typical "racetrack" is formed (see Fig. 1.3). The edge of the

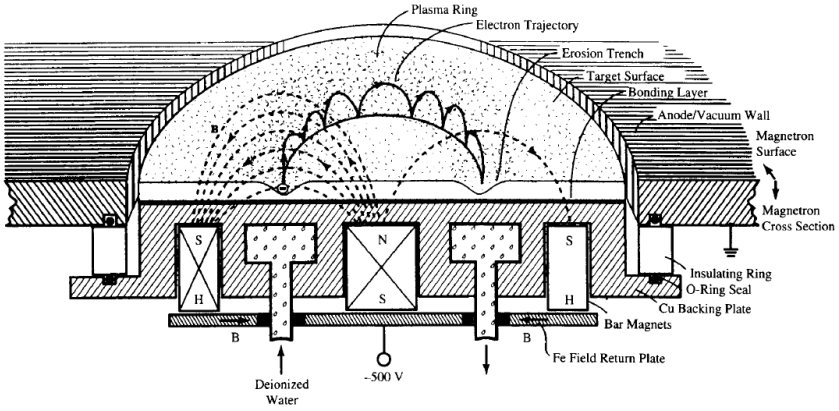

Figure 1.2: A typical configuration for magnetron sputtering [22].

racetrack is given by the local magnetic field array where $\boldsymbol{E}$ and $\boldsymbol{B}$ fields are nearly parallel and hence $\boldsymbol{E} \times \boldsymbol{B} \approx 0$. The cross-field confinement here is minimal and the electrons escape the region without causing localized dense ionization.

The design of planar source enables sputtering of magnetic as well as non-magnetic materials [23]. For the planar basic design the target material utilization is rather poor $\sim$ 25 – 35 % in the standard two pole magnetic configuration, but can be enhanced to $\sim$ 45 – 60 % in some special configurations [24]. Other designs like cylindrical cathodes with movable magnets are often used with material utilization $>$ 80 % [25].

1.4 Magnetic field configuration

Balanced magnetic field configuration of magnetron sputtering was developed in early 1970s [26, 27]. In this configuration the electrons are trapped in the vicinity of the target and the ionization efficiency is dramatically increased compared with diode sputtering. This results in a much denser plasma that can be sustained at lower pressure ($\sim 10^{-1}$ Pa compared to $\sim 10^{0}$ Pa) at lower voltage ($\sim$ 500 V compared to $\sim$ 2 – 3 kV) than in diode sputtering. The plasma region expands several tens of millimetres from the cathode (typically $\sim$ 60 mm) [28]. If the substrate is within this region during the deposition, ion flux on the substrate will be present. This additional energy can alter the structure and properties of the final film. If the substrate is outside of this region, it will be in a low ion concentration area. Typically the saturated ion current on the substrate in this case is $<$ 1 mA/cm^2, which is generally too low value to significantly alter the film properties. The energy of impinging ions can be increased by applying

Figure 1.3: Racetrack formed throughout the target life. a) top view b) side view

higher substrate bias value. Nevertheless, too high value of the bias can lead to an increased stress in the film and/or to creation of defects. A higher ion flux at a lower substrate bias is generally preferred.

In the late 1980s [29] an unbalanced configuration for magnetron sputtering was developed. This configuration makes reaching higher ion currents on the substrate (> 2 mA/cm^2) possible. Here, even at lower negative substrate bias < 100V, the impinging ion energy is sufficient to alter the parameters of the growing film. There are essentially two ways to alter the magnetic field, either to strengthen the central pole or the outer pole. The so-called type 1 unbalanced magnetron has stronger central pole compared to the outer pole. In this case the magnetic field lines which do not close in on themselves are directed to the chamber walls. This design is not commonly used due to low ion currents to the substrate. Type 2 unbalanced magnetron on the other hand utilizes stronger outer pole on the edge of the target. Using this design some of the magnetic field lines are directed towards the substrate. Some secondary electrons are drawn along these lines and as a result the plasma is less closely bound to the target and is allowed to flow onto the substrate. Consequently high ion currents can be extracted from the plasma without the need of external biasing of the substrate. The comparison of a balanced, type 1 unbalanced and type 2 unbalanced magnetic field configurations is schematically sketched in Fig. 1.4.

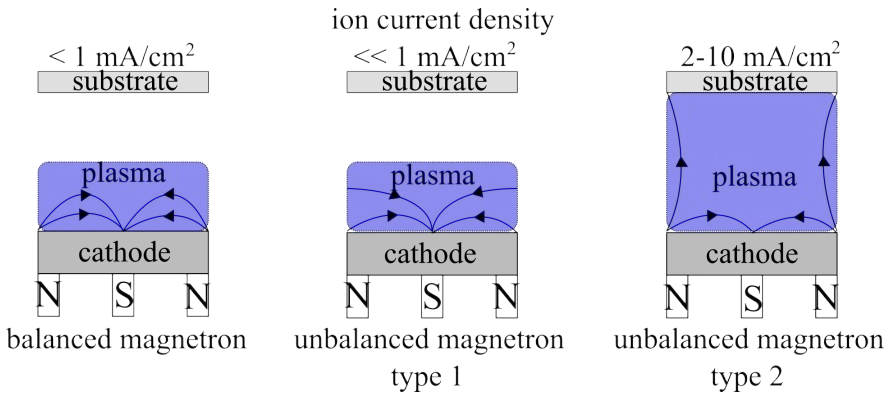

Figure 1.4: Comparison of a balanced, type 1 unbalanced and type 2 unbalanced magnetic field configurations.

1.5 Reactive magnetron sputtering

Reactive magnetron sputtering is a process where one of the coating species enters the deposition chamber in a gas phase. Typically nitrides (when introducing nitrogen) and oxides (when introducing oxygen) are synthesized in this manner. Such process has several advantages:

- compounds can be formed from simple single element targets
- insulating compounds can be prepared from conductive targets

However, the versatility of this process is gained at the expense of increasing the complexity of the deposition process itself [1].

Chemical reactions during reactive magnetron sputtering occur at the target, at the substrate and at the chamber walls. The relationship between the depositions process parameters and the reactive gas flow is generally very nonlinear as the growing film acts as an additional getter pump for the reactive gas. When the reactive gas floe is low, virtually all of the reactive gas atoms are incorporated in the growing film. The cathode processes are largely that of a simple Ar sputtering. The coatings are largely of the same composition as the target itself.

As the number of reactive gas atoms adsorbed per one metal atom reaches a ratio corresponding to stoichiometric film composition (e.g. ratio of 1:1 for TiN compound for sputtering of Ti target in N_2/Ar gas mixture), there is a sudden increase in the reactive gas partial pressure. This change in the composition of the sputtering gas results in a pronounced change of the processes on the cathode. A surface layer of the compound is formed on the target. The process is shifted to the so called *poisoned* state. This change of the target surface composition is also generally accompanied by changes

in the target voltage due to differences in the secondary electron coefficient of the target.

In order to shift back from the poisoned mode to the metallic mode a significant decrease of the reactive gas flow is required. The reactive gas flow needs to be much lower than in the situation of the reverse transition from metallic to the poisoned mode. This behaviour is called hysteresis.

1.6 Practical aspects of magnetron sputtering

Magnetron sputtering requires low pressure environment in order to reach high enough mean free paths of the sputtered particles. The typical operating pressure during the deposition is in the order of 10^{-1} to 10^{0} Pa. The base pressure of the deposition chamber is generally much lower in the order of 10^{-4} to 10^{-6} Pa. Therefore, a combination of a turbomolecular pump (previously diffusion pump) and a forepump is employed. The forepump can be a rotary oil pump, however, an oil–free pump such as scroll or Roots pump is generally preferred due to possible contamination of the apparatus by oil vapour.

Magnetron sputtering is a very versatile deposition technique. Nearly any solid material can be deposited onto any solid or powder substrate. However, the specifics of the process must be chosen accordingly. Sputtering by direct current (DC) is suitable for conductive e.g. metalic targets. If DC power would be used with non-conductive targets, those would get charged until an arc occurred. Therefore, a different power source has to be used. Radiofrequency (RF) power sources at 13.56 MHz can be utilized for such applications. Bi-polar pulsed DC power sources are also an option. Both enable the negative charge to be drained from the target either during the positive half-period in case of RF or during a short switching of the target to positive potential in case of the bi-polar pulsed DC.

1.7 Example of a deposition process

A deposition generally consists of several steps. First, the target needs to be cleaned by a discharge to eliminate any contaminants on the surface. The substrate itself needs to be cleaned as well to remove any surface contaminants such as the native oxide layer to promote the coating adhesion. These two steps can be done in parallel if the target and the substrate are separated by a shutter. Only then the deposition itself starts by setting the desired depositions parameters such as target powers, substrate bias, pressure, gas flows and temperature. If ceramic non-conductive targets are used, the power must be gradually ramped to avoid target fracture due to thermal

stress. After the desired deposition time, the power to the targets is cut and the gas valves are closed. The substrates generally need to cool down under vacuum. Then, the chamber may be evacuated and the deposited coating can be unloaded.

Chapter 2

Vacuum evaporation

doc. Mgr. Pavel Slavíček, Ph.D.

2.1 Vacuum evaporation principle

The deposition by the thermal evaporation method is simple and very convenient. The basic physical principle of evaporation is heating the material. Solid materials vaporize when heated to sufficiently high temperatures. The dependence of the vapour pressure on the temperature for evaporated materials is important for the deposition. The condensation of the vapour onto a substrate yields thin solid films.

Thin films of carbon deposited by evaporation inside an electric bulb were probably first observed by Edison in 1879 [30]. Vacuum deposition of metallic thin films was not common until the 1920s. Optically transparent vacuum-deposited anti-reflection (AR) coatings were patented by Macula (Zeus Optical) in 1935. [32].

A typical configuration for vacuum evaporation is shown in Fig. 2.1. Vacuum deposition normally requires vacuum better than 10^{-2} Pa in order to have a long mean free path between collisions. At this pressure there is still a large amount of concurrent impingement on the substrate by potentially undesirable residual gases that can contaminate the film. If film contamination is a problem, a high or ultra-high vacuum environment can be used to produce a film with the desired purity. Typical pumping system is a combination of rotary vane pump + diffusion pump or dry pump (scroll, multi-stage roots,..) + turbomolecular pump.

Some examples of the materials used for evaporation is shown in Tab. 2.1. Many elements evaporate, but many such as chromium (Cr), cadmium (Cd), magnesium (Mg), arsenic (As), and carbon (C) sublime, and many others such as antimony (Sb), selenium (Se), and titanium (Ti), are on the borderline between evaporation and sublimation [32]. Evaporation of alloys is problematic. The constituents of alloys and mixtures vaporize in a ratio

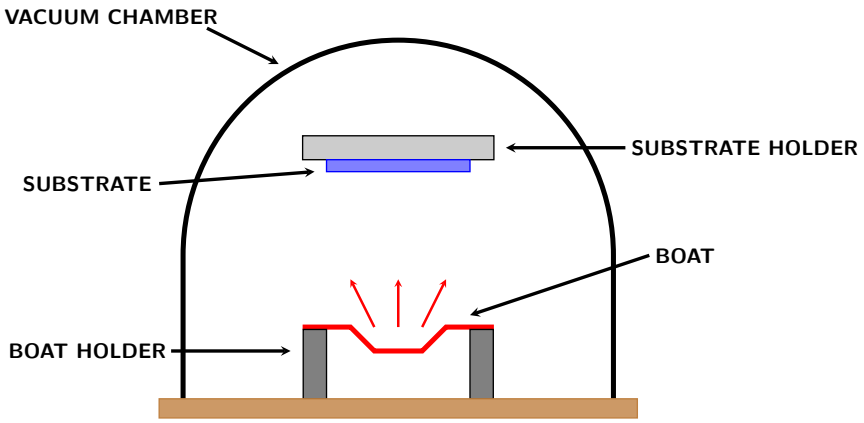

Figure 2.1: Deposition system configuration.

that is proportional to their vapour pressure. The high vapour pressure constituent vaporizes more rapidly than the low vapour pressure material.

Table 2.1: Examples of the materials for evaporation: M – molecular weight, d – density, T_m – melting temperature, T_e – temperature at which the deposition rate at 10 cm from a 1 cm^2 source will be 2.5 nm/s [31].

Element	Symbol	M	d [g cm^{-3}]	T_m [K]	T_e [K]
Aluminium	Al	27.0	2.70	930	1460
Chromium	Cr	52.0	7.20	3700	1700
Copper	Cu	63.5	8.92	1356	1580
Gold	Au	197.0	19.3	1336	1670
Silver	Ag	107.9	10.5	1230	1330
Iron	Fe	55.8	7.86	1810	1770
Nickel	Ni	58.7	8.90	1730	1810

2.2 Evaporation sources

Thermal evaporation requires that the surface and generally a large volume of material be heated to a temperature at which there is an appreciable vapour pressure. The most common way of heating materials that vaporize is by contact with a hot surface that is heated by passing a current through

a material (resistively heated). Direct and indirect heating are used. Evaporation sources must contain molten liquid without extensive reaction and the molten liquid must be prevented from falling from the heated surface. This is accomplished either by using a container such as a crucible or by having a wetted surface. The heated surface can be in the form of a wire, boat, basket, crucible etc. Wetting is desirable to obtain good thermal contact between the hot surface and the material being vaporized. Wetted sources are also useful for depositing downward and sideways.

Typical resistive heater materials for direct heating are W, Ta, Mo, C. These elements have a low vapour pressure at high temperature. Resistive heating is typically by low voltage and very high current (up to several hundreds of amperes) power supplies.

Example of various tungsten boats are depicted in Fig. 2.2. Tungsten spirals and basket are shown in Fig. 2.3. Molybdenum boats with covers are illustrated in Fig. 2.4.

Evaporation sources degradation can occur with time. This can be due to reaction of the evaporation material with the heated surface. When there is reaction between the molten source material and the heater material, the vaporization should be done rapidly. For example, palladium, platinum, iron, and titanium should be evaporated rapidly from tungsten heaters [32]. Solution to this problem can be used indirect heating. In this case crucibles of quartz, graphite, alumina, beryllia and zirconia are used with tungsten basket heater. Example of carbon, alumina and quartz crucibles are shown in Fig. 2.5.

2.3 Example of evaporation system

Home-made evaporation system is used in our laboratories, see Fig. 2.6. This device is assembled from standard vacuum components and few home-made parts. This system has sphere vacuum chamber with inner diameter of about 75 cm. The device is equipped with two holders for evaporation sources. Maximal current for evaporation is 400 A.

The system is equipped with a turbomolecular pump backed by a dry scroll pump and with a system of manually operated valves. The ultimate base pressure is about 2×10^{-4} Pa. Pressure is measured by Pirani manometer and ionization manometer with cold cathode. Layer thickness is measured during deposition by crystal sensor. The thickness of the deposited layers may be from 5 nm up-to several µm. This device can evaporate metals (Al, Au, Ag, Cr, Cu, Fe, Ni,...) and some alloys and compounds (NiCr, SiO, cryolite, MgF_2, ITO,...).

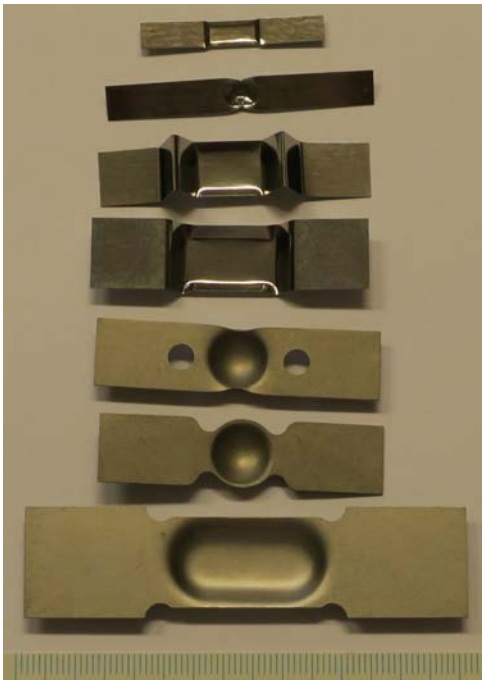

Figure 2.2: Tungsten boats.

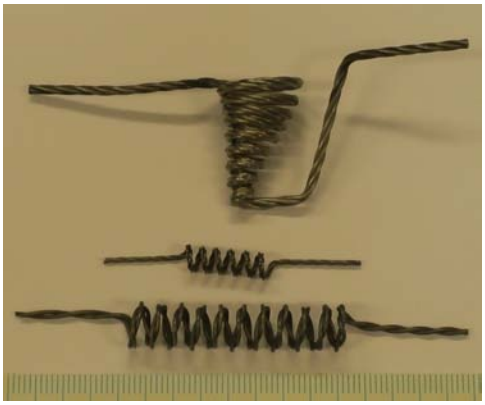

Figure 2.3: Tungsten spirals and basket.

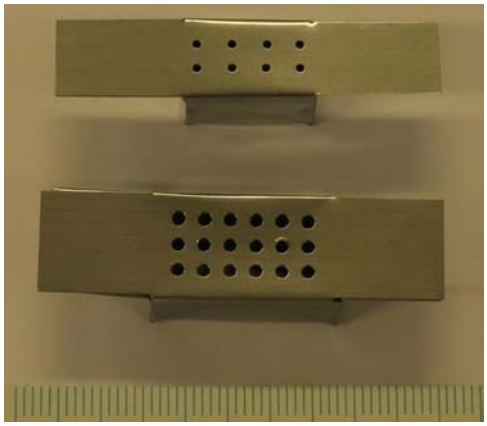

Figure 2.4: Molybdenum boats with covers.

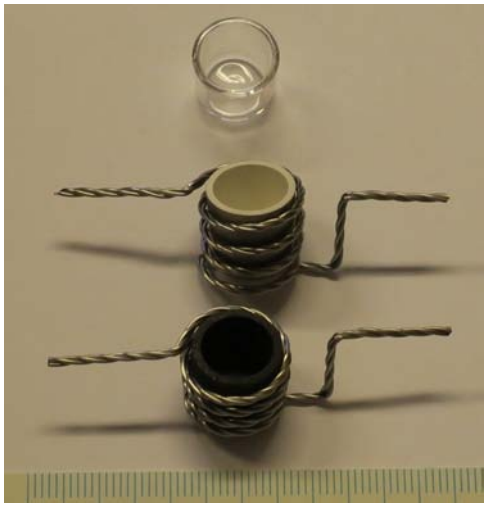

Figure 2.5: Crucibles: carbon, ceramic and quartz.

Figure 2.6: Evaporation system.

Chapter 3

Plasma enhanced CVD

doc. RNDr. Vilma Buršíková, Ph.D.

Plasma Enhanced Chemical Vapor Deposition (PECVD) is an important deposition method for the fabrication of thin films with very wide range of properties and potential applications. The first commercial application of PECVD originated for semiconductor technology in the 1960s. The PECVD technique has rapidly evolved and expanded and it is now used in many industries for many different applications. PECVD forms a kind of connecting area between physical and chemical deposition. The technique uses electrical energy to generate a glow discharge (plasma). The electrical energy is supplied to a neutral gas mixture causing formation of charge carriers. In PECVD techniques, there are various ways to supply energy to a neutral gas for plasma generation:

- Direct Current (DC) - DC electric fields are less frequently employed due to charging effects in case of electrically nonconducting substrates.

- Radio-frequency (RF) - RF electric fields are most commonly used to generate and sustain a plasma in a low-pressure environment for technical applications. Most commonly, a frequency of 13.56 MHz is used for plasma deposition, since this is the common standard in research and industry in order to avoid interference with telecommunication applications.

- Microwave (MW) - In the MW range electrons are accelerated and collisions are induced less efficiently as in the RF range due to the higher frequency. For this reason, the ignition of a MW plasma is more difficult and depends strongly on the pressure and the gas composition. (2.45 GHz was determined as the standard frequency for MW discharges.)

- Electron Cyclotron Resonance (ECR) - In order to overcome the above described problem of MW, often a magnetic field is additionally ap-

plied, forcing the electrons on helicon pathways. This concept is referred to as an electron cyclotron resonance (ECR) source.

- Dual frequency discharges (MW/RF, DC/RF, LF (low frequency)/RF) DF: For DF discharges, consisting of a MW discharge simultaneously superimposed by a RF signal, high deposition rates are reported [35] combined with the formation of a high voltage sheath. Dual DC/RF and LF/RF plasma systems show the advantage of a more flexible control of the ion current density and the ion kinetic energy.

The RF PECVD technologies are most commonly applied and for this reason they will be discussed more in detail. The RF PECVD techniques are further divided into two categories. The RF plasma may be capacitively (CCP) or inductively (ICP) coupled into the plasma according to the arrangement of electrodes used to generate the discharge. Inductive coupling is realized by a planar or a helical coil, mostly by external coupling through a dielectric wall or window rather than directly in the plasma zone. A time-variant magnetic field is induced by the RF powered coil, leading to electron acceleration. ICP is favorable if a high ion density and low ion bombardment of the adjacent walls is desired. Nevertheless, for most plasma processes, including deposition and etching, capacitive coupling is of advantage. Here, electrodes are arranged in parallel plate configuration. In the simplest case there is a bottom powered electrode and the grounded walls create the second electrode, as it is shown in Fig. 3.1.

Atmospheric pressure systems are also available however they are less common as high pressure plasmas are more difficult to sustain. Moreover, it is difficult to prepare homogeneous films using atmospheric pressure glow discharges. Nevertheless, recently the application of atmospheric pressure deposition methods has increasing tendency mainly because of the economic point of view.

The plasma most commonly used for PECVD is a non-isothermic plasma (glow discharge) that is excited in the gas in the presence of a high-frequency electric field at low pressure [33]. In a high-frequency electric field, the gas is partially ionized to electrons and ions. Electrons that are much lighter than other plasma components are therefore quickly accelerated to high energy level that corresponds to a value of 5000 K. As the electrons are very light, they do not greatly contribute to the overall plasma temperature. On the other hand, ions with their high mass and therefore considerable inertia are unable to respond to the rapidly changing direction of the electric field. As a result, the temperature of the ions is considerably lower than the electron temperature and the overall plasma temperature is also lower. For this temperature difference (electrons and ions), plasma is called non-isothermic. High energy electrons collide with gas molecules, dissociate them and form

	isothermal	*non-isothermal*
Discharge	spark	glow discharge
Frequency	1 MHz	50 kHz-13.56 MHz, 2.45 GHz (microwave)
Power	MW	kW
Flow rate	0	mg/s
El. concentration	$10^{14}/cm^3$	$10^9 - 10^{12}/cm^3$
Pressure	100 Torr $\sim$ atm.	<2 Torr
El. temp. [K]	10^4	10^4
Ion temp. [K]	10^4	$4x10^2$

Table 3.1: Comparison of properties of isothermal and non-isothermal plasma [33].

a chemical reaction mixture. In Tab. 3.1 the characteristics of isothermal (spark) and non-isothermal (glow) discharges are compared.

3.1 The characteristics of the PECVD process

PECVD has several advantages over conventional thermal CVD techniques. In particular, it is the low plasma temperature. This makes possible to apply the technique to substrates with relatively low melting temperatures, such as aluminum or organic polymers. The low deposition temperature is advantageous also for some types of steel materials which may undergo phase transformation at higher temperatures. In Tab. 3.2 the typical deposition temperatures for CVD and PECVD are compared. Another advantage is that the effect of different thermal expansion coefficients of the substrate and the layer is suppressed due to the lower temperature. The deposition rate is higher for PECVD. Uniformity of prepared layers is also high. The low pressures under which the layers are formed lead to the formation of amorphous or very pure crystalline structures. Further advantage of the PECVD is that it allows control of the plasma-chemical interactions in a wide range resulting in wide variation of film composition, microstructure and properties. Tailoring the energetic interactions between the plasma and the coated material surface, it is possible to prepare hard inorganic materials as well as soft polymer-like materials. The method enables to almost continuously vary the coating characteristics.

The disadvantages of PECVD are as follows: It is very difficult to create absolutely clean layers. This problem is mainly related to the low pressure and diffusion of gases from the environment into the apparatus as well as the release of impurities from the substrate. Sometimes, these impurities may

Material	Deposition temperature [°C]	
	Thermal CVD	**PECVD**
Epitaxial silicon	1000-1250	750
Polysilicon	650	200-400
Silicon nitride	900	300
Silicon dioxide	800-1100	300
Titanium carbide	900-1100	500
Titanium nitride	900-1100	500
Tungsten carbide	1000	325-525

Table 3.2: Comparison of typical deposition temperatures for thermal CVD and PECVD [33]

be desirable and lead to improvements in some properties, sometimes they may cause a substantial problem. Another disadvantage is the compressive stress which arise in the deposited layers due to ion bomardement. This is especially important for thicker layers where the compressive stress may cause film delamination and cracking until the film is completely peeled. The ion bombardment may also affect or damage the surface of the substrate, especially at an ion energy higher than 20 eV. To prepare uniform samples, the plasma above them must be very homogeneous. However, this problem is also related to the construction of the apparatus.

3.1.1 Plasma parameters

To ensure high quality and reproducibility of a given plasma deposition process, a lot of plasma parameters must be controlled. That include external parameters such as working pressure p, gas flow Q_g, discharge excitation frequency f, applied power p, as well as internal plasma parameters, such as the electron (plasma) density, n_e, the electron energy distribution function, $f_e(E)$ (EEDF), electrical potentials, and fluxes of different species toward the surfaces exposed to plasma. Gas-phase chemical processes are largely responsible for the chemical composition of the films deposited, along with plasma - surface interactions and substrate surface conditions, which are responsible for film microstructure and surface morphology [34, 35, 43]. The following variables are considered the main plasma parameters, i.e. their values characterize more or less accurately the plasma state.

Discharge excitation frequency
Depending on the value of the excitation frequency, f, discharges produced in the laboratories can be separated into direct current discharges if $f = 0$, and alternating discharges for any other value of the frequency. In case of alternating discharges the electrons and the ions oscillate in plasma at

characteristic frequencies, namely *electron plasma frequency*, f_{pe}, and *ion plasma frequency*, f_{pi}, respectively. The operation of the alternating mode depends on the excitation frequency f relative to the two values of plasma frequencies f_{pe} and f_{pi}. Radio frequency (RF) discharges correspond to a value of plasma frequency that satisfies the relation $f_{pi} < f < f_{pe}$ [34,35,39].

Plasma density
The abundance of species is quantified by their corresponding densities: density of electrons, n_e, positive ions, n_i^+, negative ions, n_i^-, and neutrals, n_g.

Ionization degree
The ionization degree X_{iz} is the ratio of the ion population to population of neutrals and ions:

$$X_{iz} = \frac{n_i}{n_g + n_i} \tag{3.1}$$

Plasmas are considered fully ionized when it is of the order of 1, while weakly ionized gases exhibit degrees lower than 10^{-3} [34].

Plasma temperature
Generally, temperatures of electrons, T_e, ions, T_i, and neutrals, T_g, are not identical, unless at thermodynamic equilibrium conditions in case of thermal plasma, where these temperatures are approximately equal. In case of non-isothermal plasma the relation between these temperatures is [33, 34]:

$$T_e \gg T_i \geq T_g \tag{3.2}$$

Plasma potential
Because of their low mass, the velocity of the electrons is higher than the velocity of the ions. At the initial time of discharge ignition, the flow of electrons on a wall is much larger than that of the ions. Because of this, the plasma acquires a residual positive charge due to the excess of positive ions, the plasma potential, $V_p(t)$. The plasma potential is the highest potential of the system and it is taken often as a reference potential (i.e. all the other potentials are expressed with respect to V_p). [34, 43].

Floating potential
The floating potential V_f is the mean potential which develops on an electrically isolated object immersed in plasma. It develops due to the fact that the surface of the electrically isolated object is charged negatively because of the larger mobility of electrons. The charge of the object will be stabilized at a floating potential when the balance between electronic and ionic flux is reached [34, 35, 39, 43].

Applied RF potential
The applied RF potential $V_{appl}(t)$ is measured at the exit of the power supply before the blocking capacitor (Fig. 3.1).

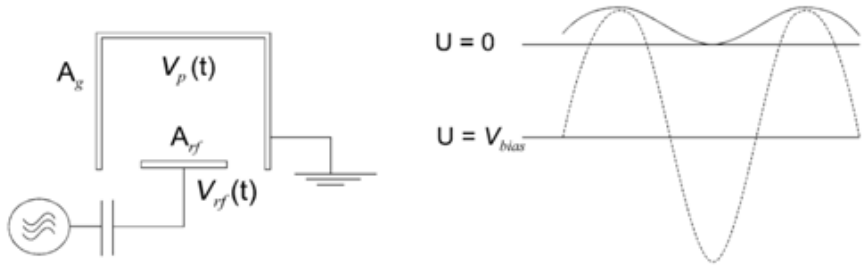

Figure 3.1: Scheme of the chosen reactor geometry for asymmetrical capacitively coupled RF discharge (on the left) ; Driving voltage, V_{rf} (dashed line on the right), and plasma potential, V_p (solid line on the right.) [39, 43]

Potential on powered electrode
The potential on the powered electrode $V_{rf}(t)$ is the potential on the RF electrode (Fig. 3.1) and it oscillates around the bias potential.

Negative self-bias potential
Most RF discharges are asymmetrical at low pressures, even if the area of parallel plate electrodes is the same because the RF current is confined not only by the electrodes, but also by the walls of the deposition chamber. The dc voltage between the plasma and the powered electrode is larger than that of between the plasma and the grounded electrode. A negative self-bias voltage, V_{bias}, is created on the powered electrode. Fig. 3.1 on the left shows the geometry of apparatus used to acquire capacitive RF discharges. On the right the idealized time dependent plasma potential $V_p(t)$ together with driving voltage $V_{rf}(t)$ is illustrated [43].

During the first half period of the positive cycle, the electrons are attracted to the cathode, causing an accumulation of the negative charge due to the existence of the blocking capacitor. In the negative half period a similar phenomenon but in opposite direction occurs for ions. After a few periods, equilibrium is reached between the electron and ion currents and the voltage at the cathode stabilizes at V_{bias}. The value of this voltage depends on the ratio of the areas between the grounded and powered electrode. This ratio is given by the following relationship:

$$V_{bias} = \left[1 - \left(\frac{A_g}{A_{rf}}\right)^n\right] . \bar{V_p}, \tag{3.3}$$

where A_g is the area of the grounded anode, A_{rf} is the area of powered cathode, $\bar{V_p}$ is the average plasma potential and n is a constant depending on the pressure. It can be shown that the ratio of the voltages on powered and grounded electrodes $\frac{\bar{V_{rf}}}{\bar{V_g}}$ is proportional to the ratio of the grounded

electrode area and the powered electrode area $\frac{A_g}{A_{rf}}$ [34, 40]:

$$\frac{\bar{V_{rf}}}{\bar{V_g}} \approx \left(\frac{A_g}{A_{rf}}\right)^q \quad q \leq 2.5 \tag{3.4}$$

3.1.2 Glow discharge

In Fig. 3.1 the schema of the apparatus with capacitive configuration of electrodes is shown. The application of potential difference between the electrodes causes collisions between electrons and molecules in the gas. If the generated potential difference is high enough, electron sources such as ionization and secondary electron emission from the cathode increase the electron population so much, that charge carriers are multiplied through an avalanche process and the discharge becomes ignited. The electrons emitted from the cathode by the bombardment of the accelerated ions arrive in the plasma, and give rise to excitation and ionization collisions with the gas atoms. The ionization collisions create new ion-electron pairs. The ions are again accelerated towards the cathode, giving rise to new electrons. The electrons can again produce ionization collisions, creating new electron-ion pairs. The above described processes make the glow discharge a self-sustaining plasma.

Plasma sheaths

Charged particles are lost by recombination or by diffusion to the electrodes and to the reactor wall. Because of the higher mobility of the electrons compared to the ions, the electron loss at the electrodes and wall is larger than the ion loss. Subsequently, the electrodes will be charged negatively with respect to the plasma. In front of both electrodes an electric field is formed between the plasma and the electrode, in which the electrons are repelled and the ions are accelerated towards the electrode. These positive space charge regions are called the sheaths [38]. In Fig. 3.2 the plot of potential profile along the x axis is illustrated. The role of plasma sheaths in material processing is critical [35]. The materials to be treated are placed in the boundary regions of plasmas. Therefore, ion bombardment in sputtering targets, deposition of atoms, ion etching and ion implantation are controlled by the shape and the potential drop in the sheaths. Several models of plasma sheaths have been developed. Eq. 3.5 provides the sheath potential, Φ, and ion and electron densities in a collisionless sheath [34]:

$$\frac{d^2}{dx^2}\Phi = \frac{en_x}{\varepsilon_0}\left[\exp\left(\frac{e\Phi}{kT_s}\right) - \left(1 - \frac{e\Phi}{\xi}\right)^{-\frac{1}{2}}\right] \tag{3.5}$$

where n_x is the electron or ion density at the sheath edge, T_e is the electron temperature, e is the elementary charge (1.602x10^{-19} C), k is the Boltzmann

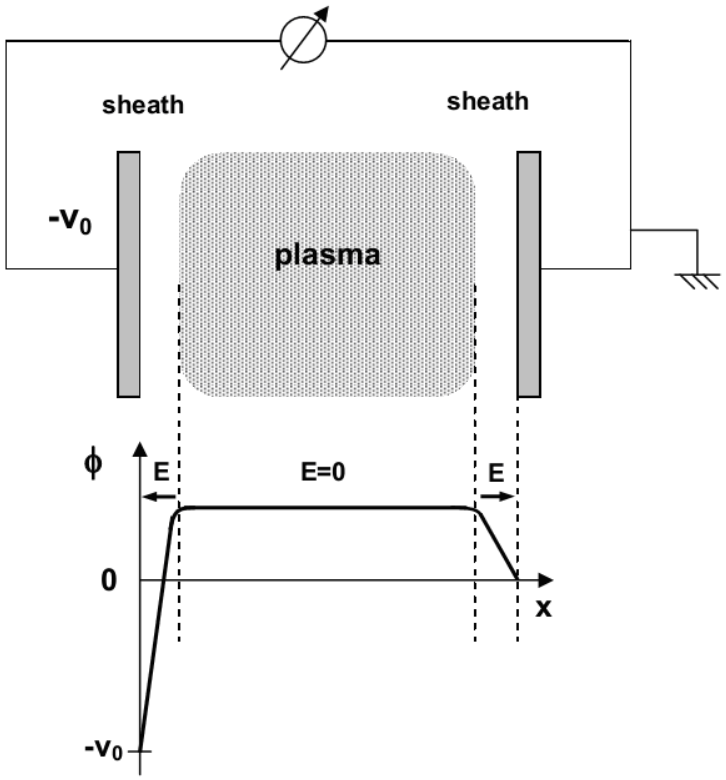

Figure 3.2: Scheme of the plasma generated in a capacitive configuration. The electric field associated to the sheaths promotes ion bombardment onto the electrodes [41].

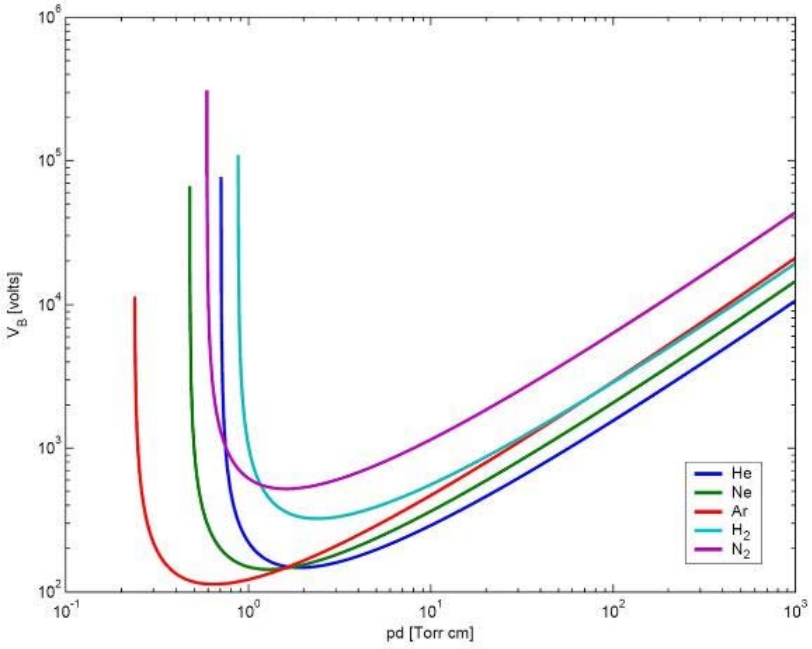

Figure 3.3: The Paschen curves for several different gases

constant (1.38x10^{-23} J/K), and ξ is the initial ion energy. Usually, sheath thickness can be estimated by using the high-voltage approaches of matrix sheath or Child Law sheath. These approximations point to thicknesses between 10 and 100 times the Debye length, while smaller values as pressure increases are observed in collisional sheaths [34, 40, 41].

Breakdown voltage The breakdown voltage, V_b, is the voltage which is necessary for the discharge to be self-sustained. It is a function of the product of the pressure p and the distance d between the electrodes, $p.d$. The plotted curve in Fig.3.3 $V_b(p.d)$ is called the Paschen curve, and shows a minimum at intermediate values of $p.d$. For too low or too high values of $p.d$ the discharge will not ignite.

Debye length The electron Debye length, λ_{De} , is the characteristic length scale in a plasma. The Debye length is defined by the following relations [37]:

$$\lambda_{De} = \left(\frac{\varepsilon_0 k T_e}{e n_0} \right) \tag{3.6}$$

It is the distance scale in plasmas over which potential gradients vanish.

$$\Phi(x) = \Phi_0 \exp\left(-\frac{abs(x)}{\lambda_{De}} \right) \tag{3.7}$$

For low-pressure plasmas, $\lambda_{De} \sim 0.1$ mm. T_e, n_e, and are fundamental parameters in plasmas. Along with plasma potential, their values are of

great utility in the discussion of glow discharge properties. The parameter restricts sheath dimensions and fulfills the relation:

$$\lambda_{De} = \frac{\upsilon_{T_e}}{\omega_{pe}} \tag{3.8}$$

where is the electron thermal velocity and is the electron plasma frequency:

$$\omega_{pe} = \left(\frac{e^2 n_0}{\varepsilon_0 m}\right) \tag{3.9}$$

with m being the electron mass. It can be considered the fundamental characteristic frequency of the plasma,ω_p , since vibrational amplitude of ions, ω_{pi} , is neglected as a consequence of infinite ion mass assumption:

$$\omega_p = \sqrt{\omega_{pe}^2 + \omega_{pi}^2} \approx \omega_{pe} \tag{3.10}$$

This frequency has a clear physical meaning. The electron cloud in plasma oscillates with respect to the ion cloud at this natural frequency, when both clouds are displaced as response of an external perturbation. This is a mechanism to keep the electric quasineutrality in plasmas.

Ion energies

Various approaches to quantitative description of the effect of ion bombardment on the the quality of films prepared by PECVD have been taken [35]. Martinu et al [36] proposed that there exist critical ion energies $(E_i)_c$ and critical ion to neutral flux ratios $(\frac{\Phi_i}{\Phi_n})_c$, which can be associated with transitions in the evolution of the film microstructure and properties. According to their research, the energy E_P delivered to the growing film per deposited particle can be adjusted to the same level by combining low and high $(E_i)_c$ and $(\frac{\Phi_i}{\Phi_n})_c$ values. It was suggested that good-quality (dense, hard, chemically stable, low-stress) films are obtained under conditions of low (10-50 eV) or intermediate (about 100 eV) ion energies, sufficient for densification $(E_i \sim (E_i)_c)$, but using high Φ_i. This reduces microstructural damage and gas entrapment yielding low values of stress. High fluxes are highly advantageous, especially when one aims at achieving high deposition rates (higher than 10 nm/s).

Plasma gas-phase reactions and plasma-surface interactions

Plasma gas-phase chemical reactions are largely responsible for the chemical composition of the deposited films along with plasma-surface interactions and substrate surface conditions, which control the film microstructure and surface morphology. During deposition, the bulk plasma parameters generally control the rate at which chemically active precursor species (molecular fragments free radicals) and energetic species (electrons, ions, photons) are created. Even for relatively simple gas mixtures involving two or three gases, several dozens of plasma reactions are taking place and many new species

are created [35]. Optimization of the PECVD processes involves identification of plasma parameters prospective for the formation of large densities of free radicals that diffuse toward the substrate surface, as well as to high concentrations of ions. The processes leading to the deposition of thin films in the plasma environment include reactions in the gas phase, transport toward the surface involving specific energetic considerations, and reactions at the surface, giving rise to film formation and microstructural evolution, providing specific film functional properties. In Tab. 3.3 examples of the basic reactions in active plasma environment are given [35].

Reaction	General equation	Example
Reactions with electrons		
Ionization	$e + A \rightarrow A^+ + 2e$	$e + N_2 \rightarrow {N_2}^+ + 2e$
Excitation	$e + A \rightarrow A^* + e$	$e + O_2 \rightarrow {O_2}^* + e$
Dissociation	$e + AB \rightarrow e + A + B$	$e + SiH_4 \rightarrow e + SiH_3 + H$
Dissociative ionization	$e + AB \rightarrow 2e + A^+ + B$	$e + TiCl_4 \rightarrow 2e + {TiCl_3}^+ + Cl$
Dissociative attachment	$e + AB \rightarrow A^- + B$	$e + SiCl_4 \rightarrow Cl^- + SiCl_3$
Three-body recombination	$e + A^+ + B \rightarrow A + B$	$e + H^+ + CH_4 \rightarrow H + CH_4$
Radiative recombination	$e + A^+ \rightarrow A + h\nu$	$e + Ar^+ \rightarrow Ar + h\nu$
Reactions between heavy species		
Charge exchange	$A^+ + B \rightarrow A + B$	${N_2}^+(fast) + N_2(slow) \rightarrow N_2(fast) + {N_2}^+(slow)$
Penning ionization	$A^* + B \rightarrow A + B^+ + e$	$He^* + O_2 \rightarrow He + {O_2}^+ + e$
Ionization by interchange	$A^+ + BC \rightarrow AB^+ + C$	$N^+ + O_2 \rightarrow NO^+ + O$
Combination	$A + B \rightarrow AB$ $AB + CD \rightarrow AC + BD$	$2SiH_3 \rightarrow Si_2H_6$ $SiH_2 + O_2 \rightarrow SiO + H_2O$
Heterogeneous interactions (with surfaces)		
Adsorption	$R_g + S \rightarrow R_S$	$CH_2 + S \rightarrow (CH_2)_S$
Metastable deexcitation	$A^* + S \rightarrow A + S$	${N_2}^* + S \rightarrow N_2 + S$
Sputtering	$A^+ + B_S \rightarrow A + B$	$Ar^+ + H_S \rightarrow Ar + H$
Secondary electron emission	$A^+ + S \rightarrow S + e$	$O^+ + S \rightarrow S + e$

Table 3.3: Basic reactions in active plasma environments R: radical; S: surface; g: gas [35].

Part II

Analysis methods

Chapter 4

Scanning Electron Microscopy

Mgr. Jana Jurmanová, Ph.D.

The scanning electron microscope (SEM) was invented in 1942, the first commercial models were constructed in 1965 by the Oatley Laboratory at Cambridge University in the UK. In Brno scanning electron microscopes are produced by three companies: Tescan, Thermo Fisher (formerly FEI) and Delong Instruments. Every third electron microscope in the world is made in Brno.

The SEM is used for observation and analysis of specimen surfaces. When the specimen is irradiated with a fine electron beam (called an electron probe) different signals are emitted from the specimen's surface and from a small depth under the surface. The electron beam is scanned by scanning coils over the surface of the specimen and an image is obtained from the entire field of view on the sample surface.

4.1 The advantages of SEM in comparison with optical microscope

- The electron microscope has a better resolution then optical. The resolution is determined by the wavelength of used particles - for photons it is about 200 nm, while for electrons it is about 1 nm (in dependence on the accelerating voltage and adjustment of the whole imaging system). The resolution determines the possible image magnification.

- The electron microscope has a larger depth of field (depth of focus), about several millimeters or more (in dependence on the numerical aperture of objective).

- The electron microscope uses more types of signals in comparison to

the optical microscope (secondary electrons, backscattered electrons, Auger electrons, cathodoluminescence, X-ray signals etc.).

4.2 SEM construction

In this part will be briefly describe the construction of important parts of the electron microscope. Many more details can be found in [44], [45], [46], [47] and [48], in Czech [49] and [56].

The block diagram of the microscope can be seen in Fig. 4.1.

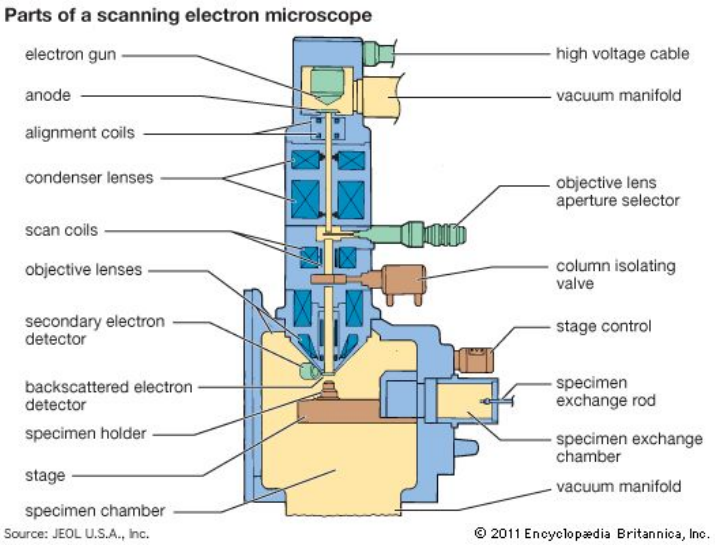

Figure 4.1: The set-up of a scanning electron microscope – taken from [53]

4.2.1 Gun

The electron gun produces the electron beam. More types of the guns exist, most often with thermionic emision (TE), field-emission (FE) and Shottky-emission (SE). The construction of these guns is schematically drawn in Fig. 4.2.

FE and SE are the most often used guns. The field emision gun has smaller electron source size (5 - 10 nm versus 15 - 20 nm), energy spread (0.3 eV versus 0.7∼1 eV) and lower lifetime (several years versus 1 to 2 years) in comparison with Shottky emission gun. The Shottky emission gun has smaller current fluctuation ($< 1\,\%$ versus $> 10\,\%$).

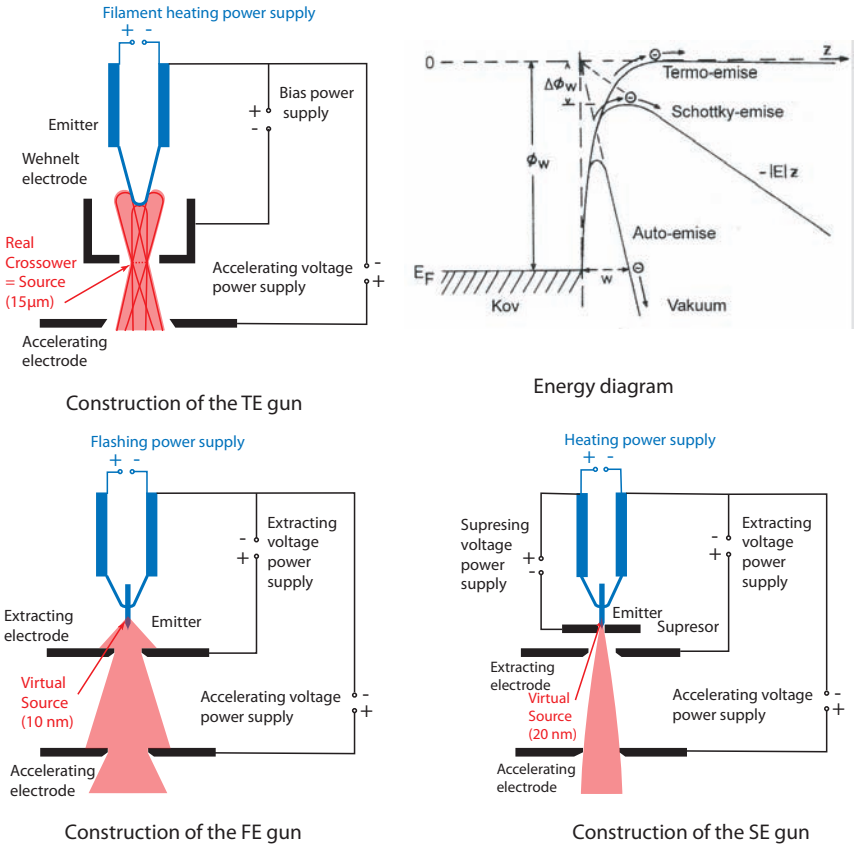

Figure 4.2: Construction of thermionic emision (TE), field-emission (FE) and Shottky-emission (SE) guns and the energy diagram of emissions from the metal to vacuum

4.2.2 Vacuum system

The inside of the electron optical system and the specimen chamber must be kept at high vacuum of 10^{-3} to 10^{-4} Pa. These components are evacuated by a turbomolecular pump backed by an oil-free pump (diffusion pump, scroll). FE or SE guns need ultrahigh vacuum and a sputter ion pump is used.

4.2.3 Electromagnetic lenses and scanning coils

The electron optical system for a SEM consists of four lenses – condenser lens, second condenser lens, objective lens, stigmators (see Fig. 4.1). The lenses are constructed based on the magnetic, the electromagnetic or the electrostatic principle. The focal length of lenses and the size of the beam spot can be changed by changing the current flowing through the coils.

Condenser lens – the adjustment of the excitation of this lens provides for changing of the electron beam diameter and the beam current.

Objective lens – is used for focusing, it determines the final diameter of electron beam.

Stigmators – lenses without spherical symmetry (quadrupole, octopole) reduce astigmatism of the beam.

Scanning coils – move the electron beam over the sample. High scanning speed is used to observe the field of view, lower speeds are used for image acquisition.

4.2.4 Detectors

The detectors process the signals generated in the sample by the electron beam. Usually we use a secondary electron detector, a backscattered electron detector and X-ray detectors.

The Everhart-Thornley detector is most often used for the detecting of electrons emitted from the specimen. The construction is shown in Fig. 4.3. The electrons from the specimen are attracted to the detector and hit the scintilator to create a light signal. This light is directed to a photo-multiplier tube throught a light guide. Then, the light is converted to electrons, and these electrons are amplified as a electric signal.

This detector is appropriate as the secondary electrons detector (with the positive voltage on the collector before the scintilator) or as the backscattered electrons detector (without the positive voltage on the collector and over the specimen). For the backscattered electrons, another detector constructions are also possible.

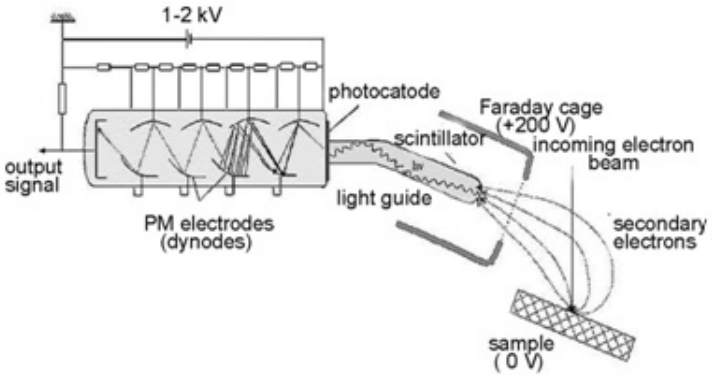

Figure 4.3: Construction of Everhart-Thorneley detector for secondary electrons – picture is published in http://www.technoorg.hu/news-and-events/articles/high-resolution-scanning-electron-microscopy-1

The X-ray detectors have usually two possible constructions - EDX (energy-dispersive X-ray spectroscopy) with SDD (silicon drift detector) detector and WDX (wave-dispersive X-ray spectroscopy) with the gas proportional counter type.

The EDX analyzer analyzes the characteristic X-ray spectra by measuring the energies of the X-rays. The X-rays emitted from the specimen enter the semiconductor detector, electron-hole pairs are generated whose quantities correspond to the X-ray energy. The X-ray analysis of all the elements from boron to uranium are made simultaneously. The EDX detector is shown in Fig. 4.4, more information about Oxford Instruments EDX detector is in [52].

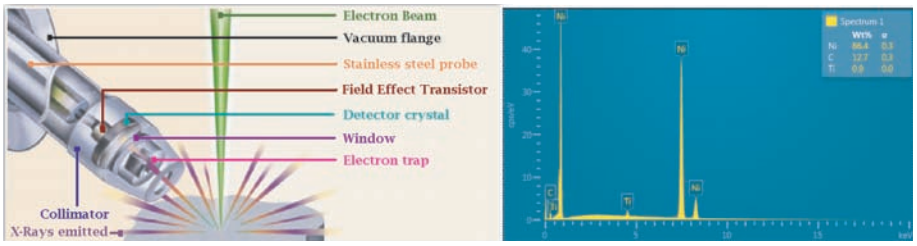

Figure 4.4: Construction of EDX detector and EDX spectrum

Inside the WDX spectrometer, crystals of specific lattice spacing are used to diffract the characteristic X-rays from the sample onto the detector (see Fig. 4.5). The wavelength of the X-rays diffracted into the detector may be selected by varying the position of the analysing crystal with respect to the sample, according to the Bragg's law

$$n\lambda = 2d \sin\theta, \tag{4.1}$$

where n is an integer referring to the order of the reflection; λ is the wavelength of the characteristic X-ray; d is the lattice spacing of the diffracting material; and θ is the angle between the X-ray and the diffractor's surface. A constructive interference and high intensity diffracted signal occurs only when this condition is met and therefore interference from peaks from other elements in the sample is inherently reduced. However, X-rays from only one element at a time may be measured by the spectrometer and the position of the crystal must be changed to tune the WDX to another element.

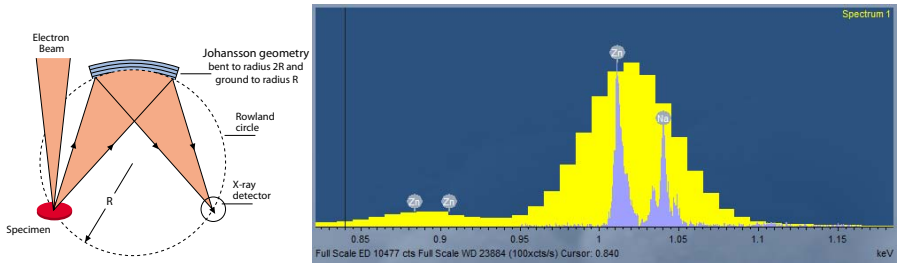

Figure 4.5: Construction of WDX detector and comparison of EDX and WDX spectra

4.2.5 Stage

The stage moves with the sample. The image sharpening is done by moving the stage in the vertical direction. The stage can be moved in x,y (horizontal plane) axes and in z-axis, can be rotated around z-axis and can be tilted around z-axis.

4.2.6 Scanning electron microscope Mira 3 – parameters

MIRA3 is a high performance SEM system which features a high brightness Schottky emitter for achieving high resolution and low-noise imaging. Its excellent resolution at high beam currents has proven to be especially advantageous for EDX, WDX. The MIRA3 configurations include GM chamber sizes with optimised geometry capable of both low and high vacuum operations.

Key features

- High brightness Schottky emitter for high-resolution/high current/low-noise imaging - resolution: 1 nm at 30 kV.
- Unique Wide Field Optics design with a proprietary Intermediate Lens (IML) offering a variety of working and displaying modes, for enhanced field of view or depth of focus, etc.

- Excellent imaging at short working distances with the powerful In-Beam detector.
- All MIRA3 chambers provide superior specimen handling using a 5-axis fully motorized compucentric stage and have ideal geometry for EDX.
- Investigation of non-conductive samples in variable pressure modes.

4.3 Sample preparation for SEM

SEM does not generally need a too sophisticated sample preparation. The sample will be glued to an imaging stub with a carbon adhesive tape and then inserted into the stage and screwed in.

- The sample has to be dust free.
- The sample has to be oil and water free.
- The operator wears dust-free latex gloves to work with samples and for inside the chamber - there is a risk of contamination of the chamber with fat and sweat from the fingers.
- For the observing of small particles (powders, nanopowders), the particles have to adhere securely to the specimen holder (new carbon tape) or fill the cavity in the holder. The sample must be blown over by a photo balloon before insertion into the chamber to remove any non-adherent powder and dust.

4.3.1 Suitable samples

Suitable sample is dust free, oil and water free and conductive. Such sample will be microscoped and analysed easily.

4.3.2 Magnetic samples

Microscope without immersion objective, such as MIRA 3, allows the observation of magnetic sample. The operator has to be carefull with such sample in small working distance, and, especially, with the magnetic powders not to contaminate the microscope chamber and objective.

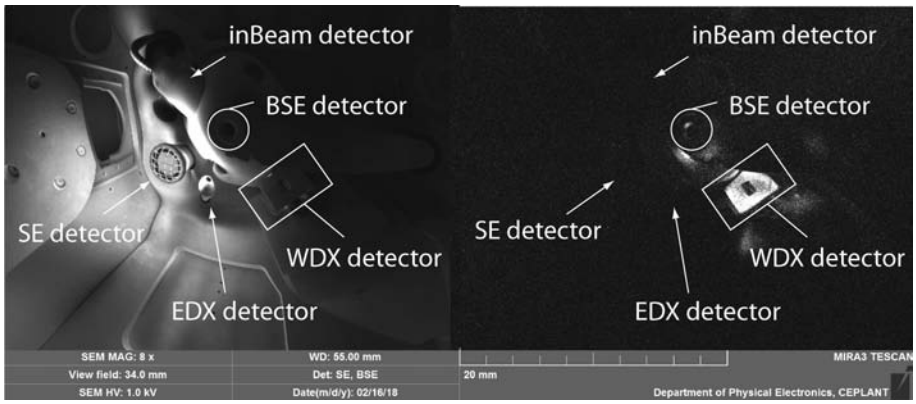

Figure 4.6: Electron mirror - image created by SE detector on the left, image obtained by BSE detector on the right

4.3.3 Non-conductive samples

The non conductive sample will be charged under the electron beam. This way we obtain an electron mirror (see Fig. 4.6) – the mirroring of the chamber on the electron layer over the sample and we will not obtain the photo of the sample surface.

A non conductive sample has to be observed carefully (low voltage, low beam density, image acquisition mode) or it has to be coated. We use the sputter/carbon coater Q150R ES [51] for sputtering with noble metals (Au, Au/Pd) and for carbon coating. The usual thickness of the conductive coating is 10 or 20 nm. The use of low-vacuum mode is appropriate for non conductive samples, whose surface cannot be coated.

4.4 SEM signals, their detection and use

The signals generated by the electron beam in the sample are schematically depicted in Fig 4.7.

The size of interaction volume is dependent on the accelerating voltage and on the chemical composition of the sample. The often detected signals are described hereunder.

4.4.1 Secondary electrons (SE)

SE have low energy (below 50eV) and are created near the surface of the specimen (about 5 nm). Topographic sensitivity and high spatial resolution make them the frequent choice for micrographic images that are sensitive

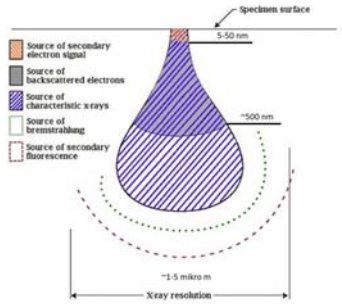

Figure 4.7: Interaction volume

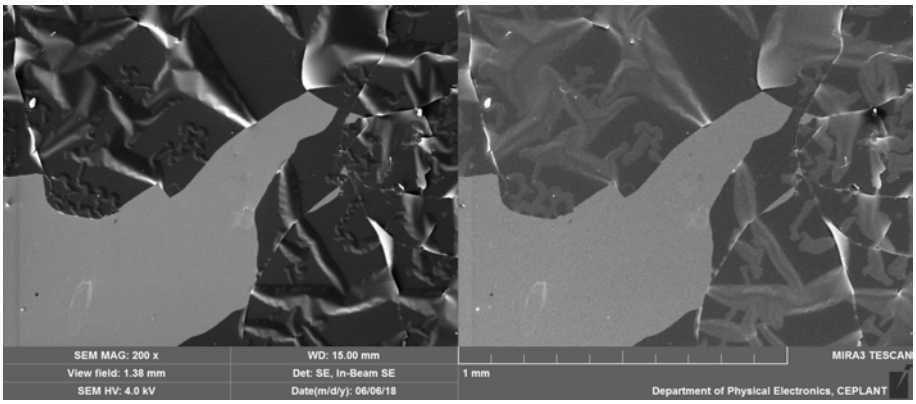

Figure 4.8: Thin delaminated carbon layer on silicon wafer. On the left: SE image, the detector is in the chamber under an angle to sample. On the right: SE image, the detector is in the beam axis above the sample

to the tilting of the sample and to the position of the used detectors - see Fig 4.8.

4.4.2 Backscattered electrons (BSE)

BSEs are more energetic than secondary electrons so they are able to escape from larger depth in the sample (dependent on the sample chemical composition and the electron beam energy). They carry information about the sample chemical composition (the brightness is proportional to the atomic number), but they are not as much topographic and have lower spatial resolution compared to secondary electrons - see Fig 4.9.

4.4.3 X-rays

X-rays are generated by elastic and inelastic electron scattering on sample nuclei. Generation of continuous spectrum of radiation (Bremsstrahlung) is

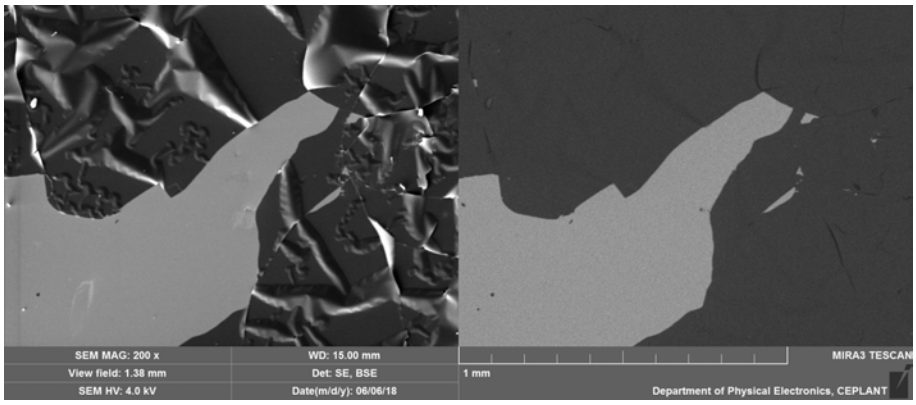

Figure 4.9: Thin partially delaminated carbon layer on silicon wafer. On the left: SE image with topographical contrast. On the right: BSE image without topographical contrast but with elemental contrast

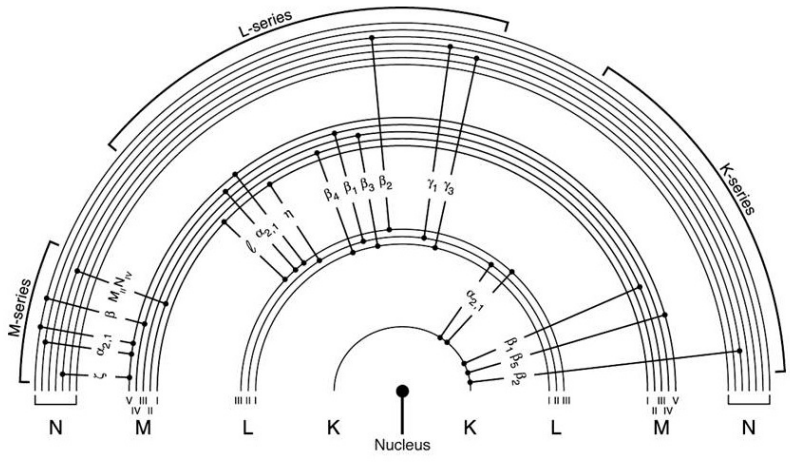

Figure 4.10: The classification of spectral lines. Concrete values for almost all elements see http://www.med.harvard.edu/jpnm/physics/refs/xrayemis.html

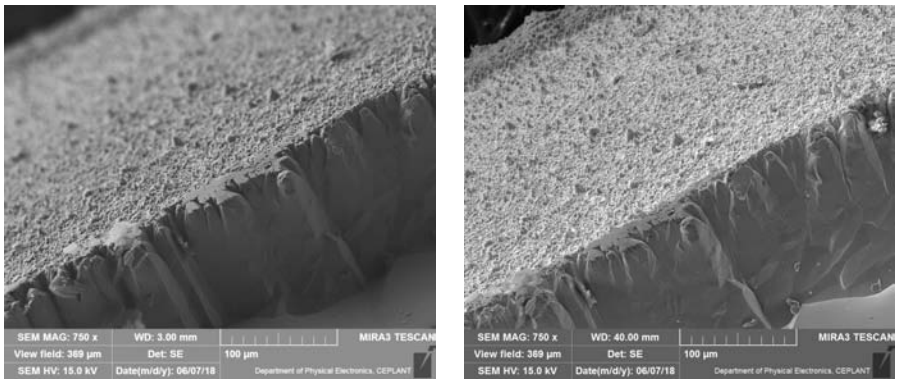

Figure 4.11: The resolution and depth mode - different depth of focus

the result of elastic scattering, while the consequence of inelastic scattering is generation of characteristic lines typical for individual elements. The X-ray generation depth is larger than that of SE or BSE and depends on the chemical composition of the sample. The used acceleration voltage has to be 1.5 to 2 times higher than the voltage needed to generate the required element line to ensure adequate excitation. The classification of spectral lines is in Fig. 4.10.

4.5 Examples of a thin layer analysis by means of SEM

This section describes how to get the most information about a sample composed of thin layers. The theory described above will be illustrated on specific examples.

4.5.1 How to obtain sharp photos with good resolution?

First we have to select the suitable working distance, accelerating voltage and imaging mode - resolution or depth. If we choose a smaller working distance, we will achieve greater magnification (and resolution) of the image, but less depth of field. In this case, we use the resolution mode — our microscope has the highest resolution at 30kV accelerating voltage. If we choose a larger working distance, we do not achieve such a high resolution, however the image has a greater depth of field, especially in the depth mode - see Fig 4.11. We use wide field mode for overviews.

Then it is necessary to adjust the microscope as best as is possible — to realise the gun centering, column centering, to set the working distance and the stigmators.

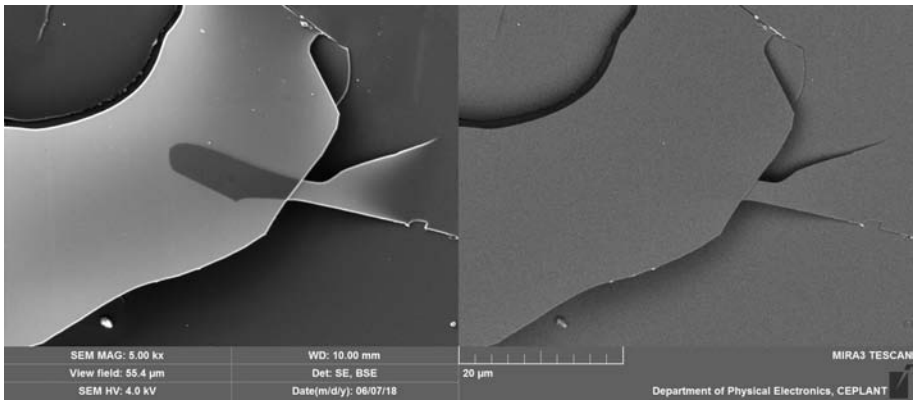

Figure 4.12: On the left: The thin carbon layer (37 nm) is transparent for secondary electrons accelerated by 4 kV accelerating voltage. On the right: The layer is chemically homogeneous, the bright surface on the left image is charged.

The accelerating voltage determines the final appearance of the image — how bright will be the edge effect (significant lightening edges of the sample), and whether the thin layers for the different types of electrons will be transparent – see Fig. 4.12.

4.5.2 How to discover the chemical homogeneity of the sample?

Backscattered electrons and X-rays provide information about the chemical composition of samples. Thus, for the first analysis the BSE detector is used. This detector distinguishes light elements from heavy ones, but can not determine specific elements included in the sample — it is necessary to perform EDX analysis. If the sample includes only elements with very close proton numbers in the sample, the shades of grey associated with these elements are difficult to distinguish and the sample looks chemically homogeneous – see Fig 4.13 and Fig 4.14.

4.5.3 The thickness of the layers and the cross section of the sample

The sample thickness can be determined by the means of imaging of a delaminated part of the layer suitably positioned against the lens of the microscope, or by imaging of the cross-section of the sample. The thickness of the delaminated layer is shown in Fig 4.15, the cross-section of the sample shown in Fig 4.16.

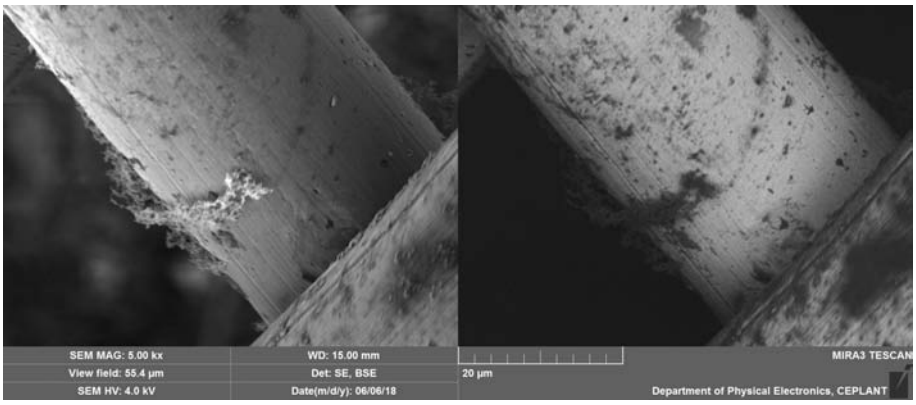

Figure 4.13: Carbon residue on steel mesh – the BSE detector shows the chemical contrast between mesh material and carbon clusters, but does not specify the exact chemical composition of the mesh.

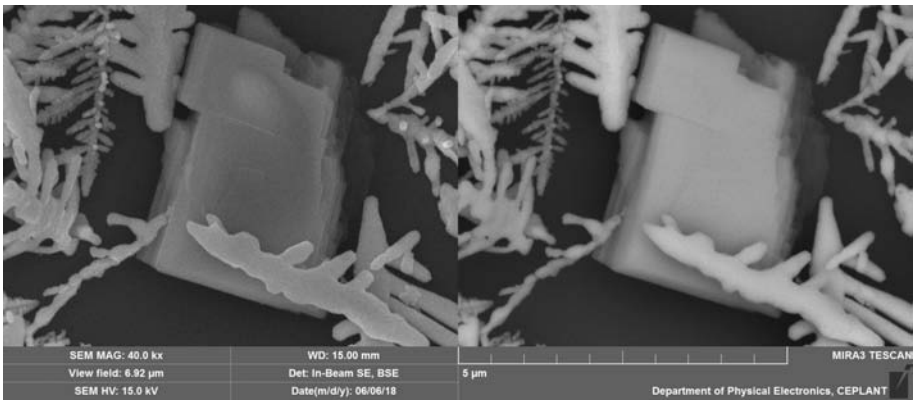

Figure 4.14: The crystals of teluroxide between silver little branches on silicon wafer - the contrast between silicon (atomic number 14) and heavy elements is visible, the contrast between tellurium (atomic number 52) and silver (atomic number 47) is very small.

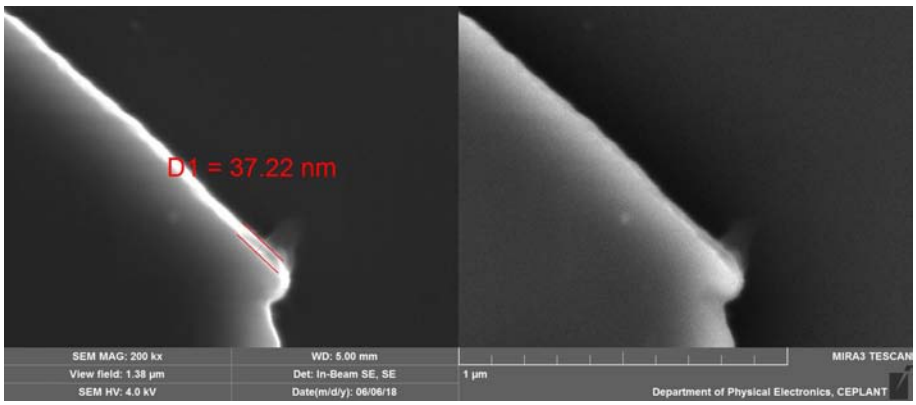

Figure 4.15: The thickness of a delaminated layer - SE and BSE images of this sample are Fig 4.8 and Fig 4.9

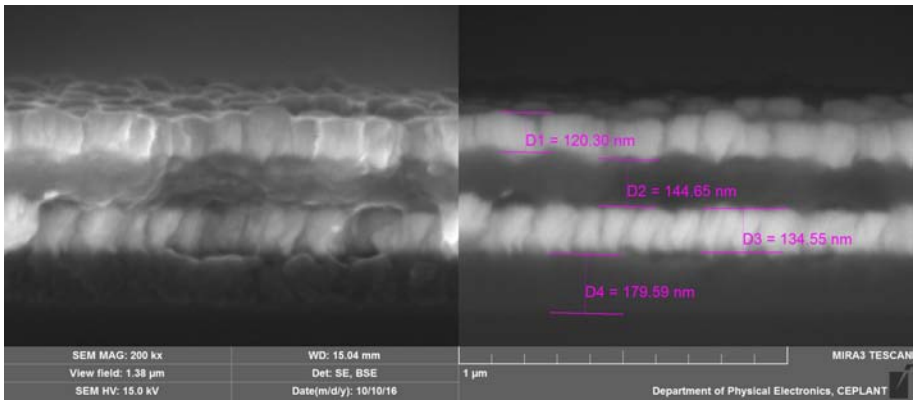

Figure 4.16: Sample cross-section. Layers are: silicon substrate, aluminum layer (thickness 180 nm), tungsten layer (thickness 135 nm), aluminum layer (thickness 145 nm), tungsten layer (thickness 120 nm). The topography of the cross section is visible in SE, BSE image separates the layers of lighter and heavier elements. For the specific determination of the elements of the different layers an X-ray analysis is required.

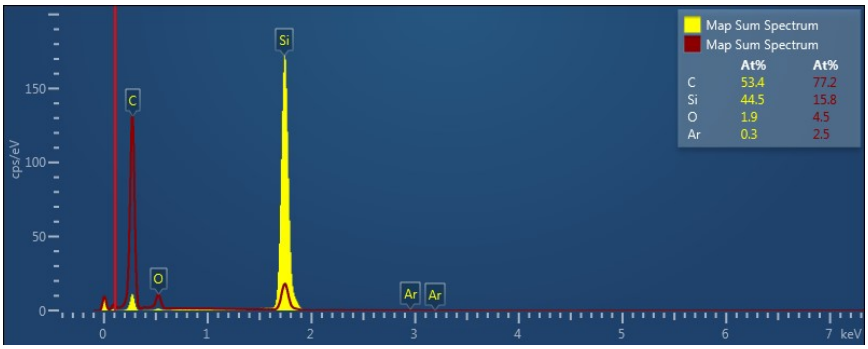

Figure 4.17: The map sum spectra of sample in Fig 4.8 measured at 4 kV (red) and 15 kV (yellow) – which results are correct?

4.5.4 The information obtained by X-ray analysis

X-ray spectroscopy can exactly determine the chemical composition of the sample — elements from boron to uranium can be measured. The results can be represented as a spectrum (chemical composition at a given location), a map (artificial colours for detected elements) or linescan (graph of the concentration of the elements on the position along the selected line).

The operator needs to choose the correct accelerating voltage to have one and a half to two times the electron's excitation energy to correctly determine the element. However,with increasing energy of the electron, the depth of penetration increases. If multiple thin layers are analysed, misinterpretations may occur by choosing to high acceleration voltage.

Spectrum and map

For example — a thin (about 40nm) carbon layer on a silicon wafer – see Fig. 4.8 and Fig. 4.9 — will be analysed. The first analysis was performed with an accelerating voltage of 15 kV in order to find all the expected elements and possible impurities. Silicon, carbon and oxygen were detected (argon is included in the deposition atmosphere). The characteristic energy for carbon, oxygen and silicon are 0.277 keV C-Kα1, 0.5249 keV O-Kα1 and 1.73998 keV Si-Kα1 (moreover Kα2 and Kβ1). At an accelerating voltage of 15 kV, the penetration depth into the silicon is much greater than the thickness of the layer — see Fig 4.18. The ratio between silicon and carbon concentration is therefore totally incorrect. The results obtained by the 4 kV analysis (2 times energy Si-Kα1) are more accurate.

The maps measured using these accelerating voltages are shown in Fig 4.19, Fig 4.20 and Fig 4.21. Obviously, using lower accelerating voltage leads to better results.

Linescan

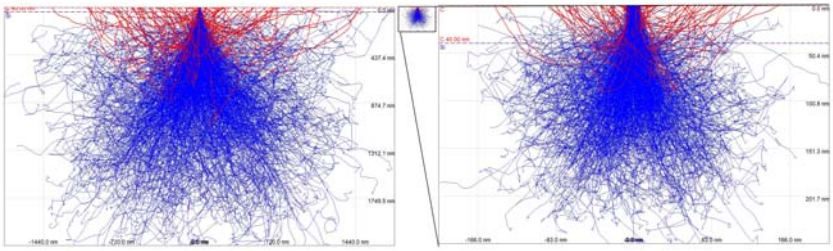

Figure 4.18: The Casino (monte CArlo SImulation of electroN trajectory in sOlids) simulates recorded signals (X-rays and backscattered electrons) in a scanning electron microscope for 4kV and 15kV accelerating voltages. The X-ray resolution and the signal depth are very diferent for these voltages.

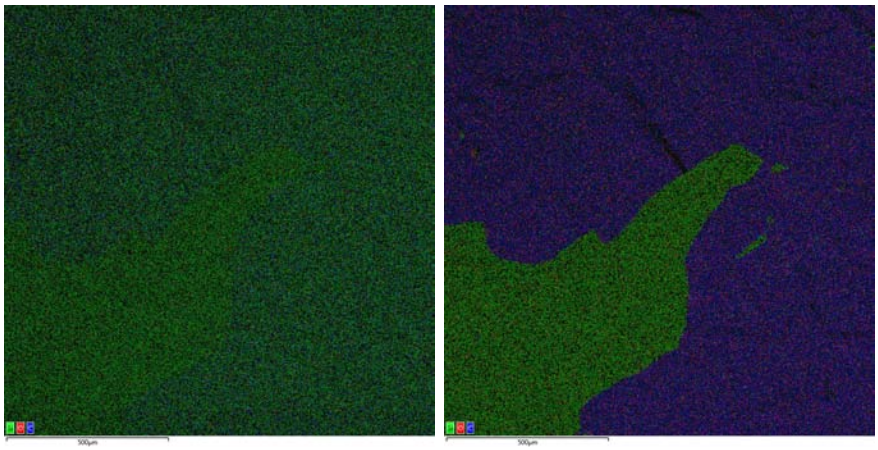

Figure 4.19: Comparison of the maps for 15 kV (on the left) and 4 kV (on the right) - part one. See Fig. 4.8 for the topology of the sample.

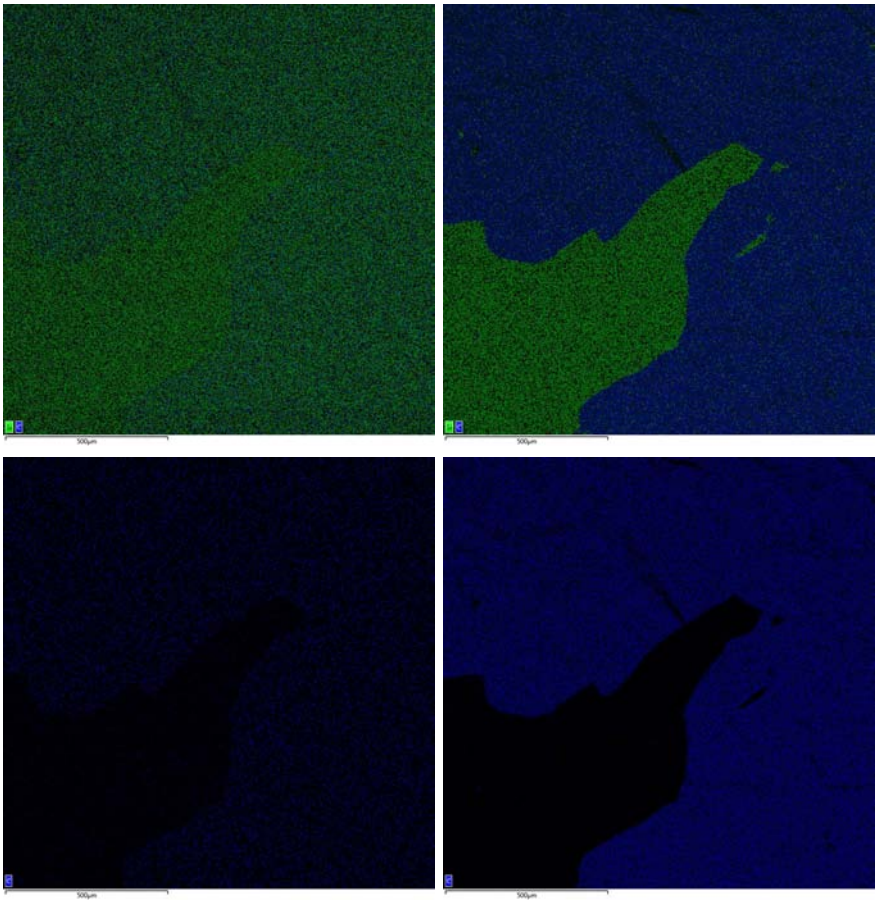

Figure 4.20: Comparison of the maps for 15 kV (on the left) and 4 kV (on the right) - part two. See Fig. 4.8 for the topology of the sample.

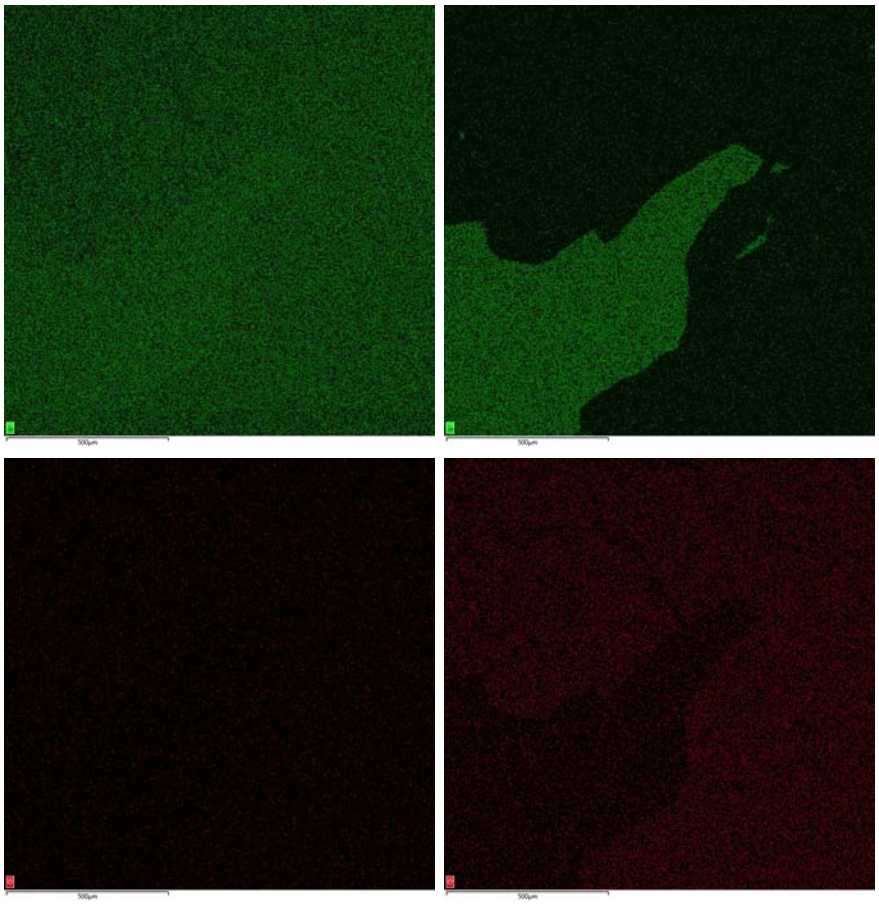

Figure 4.21: Comparison of the maps for 15 kV (on the left) and 4 kV (on the right) - part three. See Fig. 4.8 for the topology of the sample.

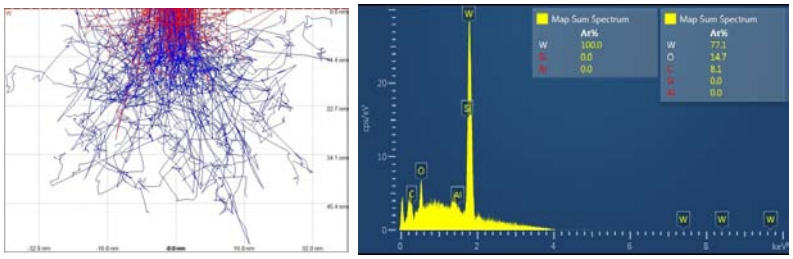

Figure 4.22: The simulations obtained by the CASINO software are shown on the left side . The spectrum of sample shown on the right side on Fig. 4.16 was measured perpendicularly to the sample surface at the beam voltage of 4 kV. The accelerating voltage used for the measurement is the lower limit for the detection of tungsten. Electrons penetrate through one layer.

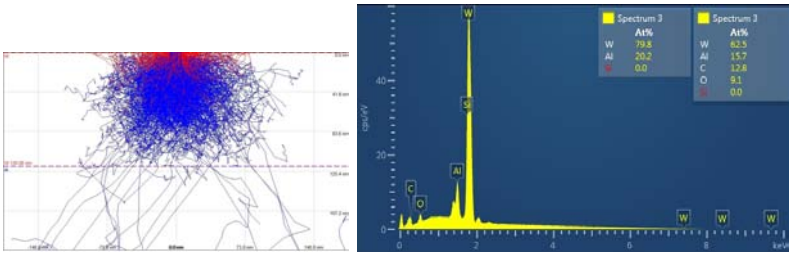

Figure 4.23: The simulations obtained by the CASINO software are shown on the left side . The spectrum of sample shown on the right side on Fig. 4.16 was measured perpendicularly to the sample surface at the beam voltage of 8 kV. The accelerating voltage used for the measurement is twice the lower limit for the detection of tungsten. Electrons penetrate two layers, the spectrum must be interpreted with this in mind.

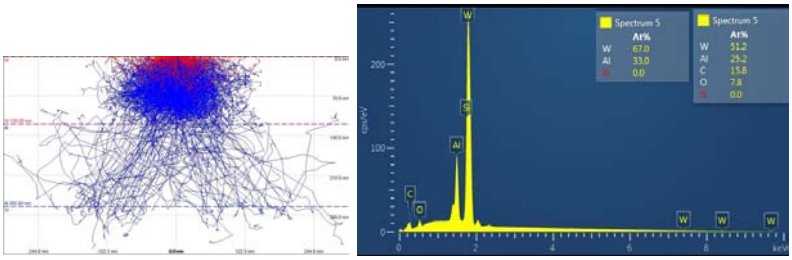

Figure 4.24: The simulations obtained by the CASINO software are shown on the left side . The spectrum of sample shown on the right side on Fig. 4.16 was measured perpendicularly to the sample surface at the beam voltage of 10 kV. Electrons penetrate through three layers.

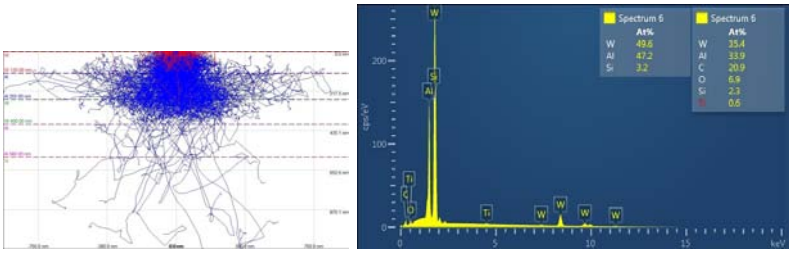

Figure 4.25: The simulations obtained by the CASINO software are shown on the left side . The spectrum of sample shown on the right side on Fig. 4.16 was measured perpendicularly to the sample surface at the beam voltage of 15 kV. Electrons penetrate through four layers.

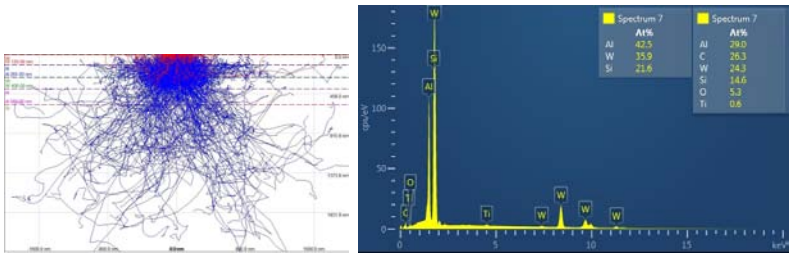

Figure 4.26: The simulations obtained by the CASINO software are shown on the left side . The spectrum of sample shown on the right side on Fig. 4.16 was measured perpendicularly to the sample surface at the beam voltage of 20 kV. Electrons penetrate through four layers.

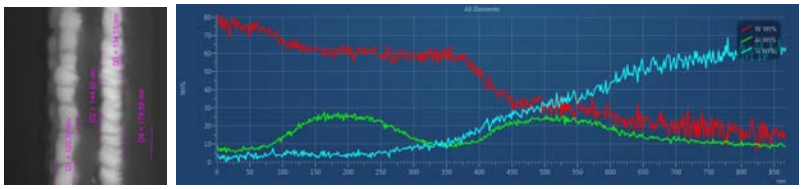

Figure 4.27: The linescan of the sample shown in Fig. 4.16 were measured via the sample cross-section. The interpretation of the linescan results needs to factor in the acceleration voltage (15 kV as in Fig. 4.25.

Linescan is a very useful tool when the sample changes the element concentration in the chosen direction. A linescan across the layers of the sample shown in Fig. 4.16 are plotted in Fig. 4.27. The result depends on the choice of the appropriate accelerating voltage. The accelerating voltage must be sufficient to determine all the elements, but the spatial region from which the X-ray signals are generated must be less than the thickness of the individual analysed layers.

Chapter 5

Atomic Force Microscopy

doc. RNDr. Vilma Buršíková, Ph.D.

5.1 Atomic force microscopy principle

The atomic force microscope (AFM) was invented in 1986 by Binning et al [59]. From that time the AFM equipments have undergone a large development. Recently, the AFM is an invaluable technique not only to acquire high-resolution topographical images, but also to map certain physical properties of specimens, such as their mechanical, electrical, magnetic or chemical properties. The AFM technique has the advantage that it can image both conducting and non-conducting samples, including polymers, ceramics, composites, glass and biological samples. With the recent AFM devices, the topography and structure of a surface can be studied either in air or in fluid. That means, that using this imaging technique, it is possible to map sample surfaces under natural conditions (in ambient air or water) without the samples being placed under destructive artificial conditions, such as drying, coating with metal, placing into vacuum conditions or freezing. AFM enables not only imaging, but also touching the tested objects and manipulating with them at the nanoscale.

The development of three technical improvements were necessary for the invention and for the further development of atomic force microscopes:

- development of piezoelectric materials (piezoscanners)
- micromachining of cantilevers (MEMS technology)
- cantilever deflection measurement techniques

5.1.1 Piezoelectric control of x,y and z movements

The piezoelectric ceramic material expands or contracts depending on the polarity of the voltage applied on them. The piezoscanner is constructed by combining independently piezoelectrodes for x, y and z direction. The piezoscanner is able to manipulate the tip or the sample with extreme precision. The scan range is established by setting the minimum and the maximum voltage and the position is established by offsetting the voltages on the piezoceramic. The scan orientation is changed by changing the phase between the signales. The relationship between the piezo-movement and piezovoltage is not linear and due to that fact the piezoscanner behaves differently when it contracts compared to its expansion. This causes hysteresis and differences between the forward and backward scan directions.

5.1.2 Cantilevers

In order to acquire images with excellent resolution it is necessary to have cantilevers with sharp tips, high displacement and high force sensitivity. Recently, the cantilevers are prepared using MEMS fabrication [61]. The following formula shows the relationships between the force F acting on the cantilever, and its displacement Δz at the place, where the tip is mounted (see Fig.5.1) :

$$\Delta z = w(L) = \frac{FL^3}{3EI}, \tag{5.1}$$

where $w(x)$ is the displacement of the centre axis as a function along the cantilever, L is the cantilever length E is the cantilevers Young's modulus and I is the moment of inertia.

The moment of inertia can be expressed as:

$$I = \frac{bh^3}{12}, \tag{5.2}$$

where b is the cantilever width and h is its thickness.

For the deflection angle (see Fig.5.2) at the end of the cantilever it is possible to calculate :

$$\theta = \frac{\mathrm{d}w(L)}{\mathrm{d}x} = \frac{FL^2}{2EI}, \tag{5.3}$$

Both the cantilever deflection at the end as well as the slope at the end of the cantilever are proportional to the force applied to the tip. Therefore the cantilever spring constant k can be expressed as follows:

$$k = \frac{3EI}{L^3} = \frac{Ebh^3}{4L^3}. \tag{5.4}$$

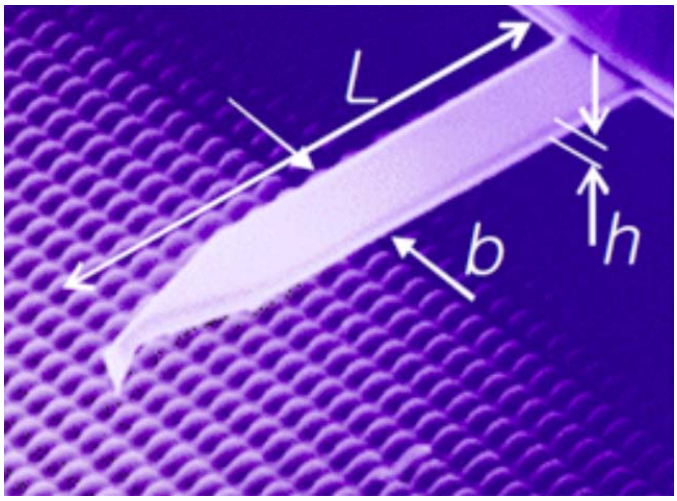

Figure 5.1: Schematic of the AFM cantilever [61].

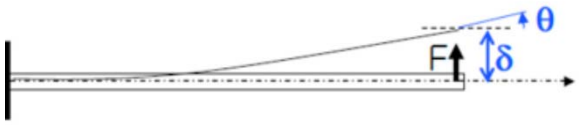

Figure 5.2: Schema of the cantilever deflection [61].

5.1.3 Cantilever deflection detection method

Recently, most of the AFMs use a laser beam to detect the cantilever deflection. The laser shines onto the back of the cantilever, which is coated with a reflecting film (for example gold), and the angle of the reflected beam is measured using a four-quadrant laser diode. The deflection and the torsion of the cantilever can be measured on the basis of the total amount of the laser light, that hits on the four quadrants (see Fig. 5.3) :

Vertical deflection $=(A_1 + A_2) - (B_1 + B_2)$

Horizontal deflection (torsion)$=(A_1 + B_1) - (A_2 + B_2)$.

Because the cantilever deflection is proportional to the force acting on the cantilever (and it is proportional to the tip displacement) we can use the deflection angle change as a measure of the tip displacement.

5.1.4 Feedback control

The feedback control is necessary in order to maintain a fixed relationship (force, displacement, etc.) between the tip and the scanned surface. The feedback control enables to keep the forces between the tip and the surface

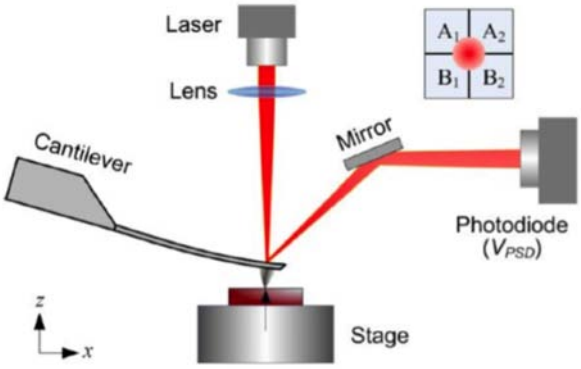

Figure 5.3: Cantilever deflection readout [61].

at user defined *setpoint* level. For example in case of the contact mode, when the control signal (in the case of the contact mode this is the cantilever deflection) is above the setpoint. When the deflection is less than the specified setpoint, the feedback loop will expand the piezo to move the tip closer to the sample. Although signal processing varies according to the image mode used (contact mode, tapping mode, etc.), the feedback loop always performs essentially the same function. The feedback system used to control tip-sample interactions and render images must be optimized for each new sample. This is accomplished by adjusting various gains in the SPM`s feedback circuit.

In the AFM, the feedback control device takes an input from the force sensor and compares the signal to a set-point value. The resulting signal is the error signal, which is sent through a feedback controller. The output of the feedback controller then drives the z piezoelectric ceramic. The most common implementation of a feedback loop in AFM is via proportional, integral and derivative (PID) controller. The PID controller takes the error signal and processes it as follows [62]:

$$Z(t) = P\left(s(t) - s_{set}\right) + I\int_0^t \left(s(t-\tau) - s_{set}\right)\, d\tau + D\frac{\mathrm{d}}{\mathrm{d}t}\left(s(t-\tau) - s_{set}\right), \tag{5.5}$$

where $Z(t)$ is the response signal, $s(t)$ is the signal from the measured interaction, s_{set} is the signal, what was set, $(s(t) - s_{set})$ is the error signal and P,I, and D have the following meaning:

- P is the proportional term describing the immediate response to the difference between the setpoint and the measured signal. It allow the probe to follow smaller, high frequency features on a surface.

- I is the integral term and it helps the system to reach the setpoint value if the present interaction signal value is only slightly shifted from the required value (in that case the P term would react too slowly). Moreover, the I term smooths the response to noise due to its averaging nature. The integral term facilitates the probe moving over larger surface features.
- D is the derivative term and it describes the response to te change in the error.

When the PID parameters are optimized, the error signal image will be minimal. As a rule of thumb: the higher the feedback gains, the faster the feedback loop can react to changes in topography while scanning [61]. Therefore, ideally one would set the gains as high as possible. However, since the AFM is not infinitely fast in responding to the output of the PID controller, one can only increase the feedback gains to a certain value. This also limits the maximum achievable scan speed. Establishing where this point is requires practice and some intuition.

5.1.5 Basic AFM modes

The principle of atomic force microscopy is based on detection of interaction forces between the probe and the force field associated with a studied material surface. The simplest model describing the interaction between two atoms is the Lennard-Jones (LJ) potential (see Fig. 5.4) It can be described by the formula

$$U(r) = 4\varepsilon \left[\left(\frac{\sigma}{r}\right)^{12} - \left(\frac{\sigma}{r}\right)^{6} \right] = \varepsilon \left[\left(\frac{r_m}{r}\right)^{12} - 2\left(\frac{r_m}{r}\right)^{6} \right], \qquad (5.6)$$

where ε is the measure of the interaction strength (it corresponds to the depth of the potential well), σ is the interatomic distance, where the potential is zero and r_m is the distance at which the potential reaches its minimum.

According to the Fig. 5.5, there are three basic regions of interaction between the probe and surface:

- free space
- attractive region
- repulsive region

Attractive forces near the surface are caused by a nanolayer of contamination that is present on all surfaces in ambient air. The contamination is typically

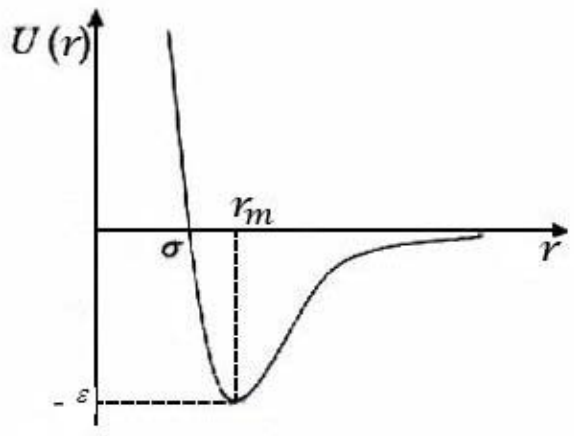

Figure 5.4: Lennard-Jones potential.

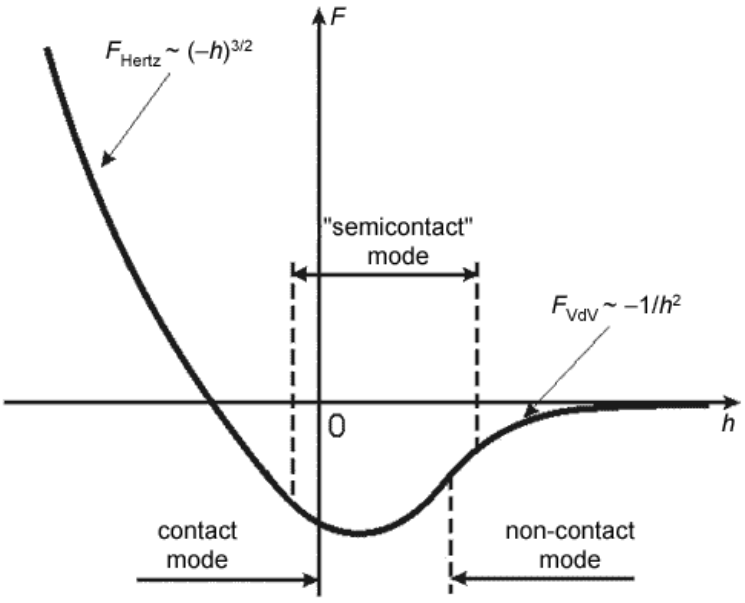

Figure 5.5: Lennard-Jones potential. Illustrations of the contact, semicontact and non-contact mode.

an aerosol composed of water vapor and hydrocarbons. The amount of contamination depends on the environment in which the microscope is being operated. Repulsive forces increase as the probe begins to 'contact' the surface. The repulsive forces in the AFM tend to cause the cantilever to bend up. There are two primary methods for establishing the forces between a probe and a sample when an AFM is operated. In contact mode the deflection of the cantilever is measured, and in vibrating mode the changes in frequency and/or amplitude are used to measure the force interaction. As a rule of thumb, the forces between the probe and surface are greater with contact modes than with vibrating modes.

Contact mode

In Contact mode, the cantilever deflection during the scanning reflects repulsive force acting upon the tip, which is related to the cantilever deflection value x under Hooke's law: F = -kx. Here k is the cantilever spring constant, which usually vary from 0.01 to several N/m. The main disadvantages of Contact Mode are, that soft samples can be destroyed by the scratching because the probe scanning tip is in direct contact with the surface. As a result the acquired topography of the sample may become distorted. The possible existence of substantial capillary forces imposed by a liquid adsorption layer can decrease the resolution. There are two different possibilities to scan the surface in Contact mode [63]:

- Contact Height Mode - The scanner of the microscope maintains fixed end of cantilever on the constant height value. Therefore *the deflection of the cantilever* reflects topography of sample under investigation (Fig. 5.6). The main advantage of Constant Height mode is the high scanning speed, which is restricted only by resonant frequency of the cantilever. The disadvantage of this mode is that the scanned samples must be sufficiently smooth.

- Constant Force Mode - The deflection of the cantilever is maintained by the feedback circuitry on the preset value. So *the vertical displacement of the scanner* under scanning reflects topography of sample under investigation (Fig. 5.7). The main advantage of Constant Force mode is the possibility to measure with high resolution simultaneously with topography some other characteristics, such the friction forces, spreading resistance etc. The disadvantage of the Constant force mode is that the speed of scanning is restricted by the response time of feedback system.

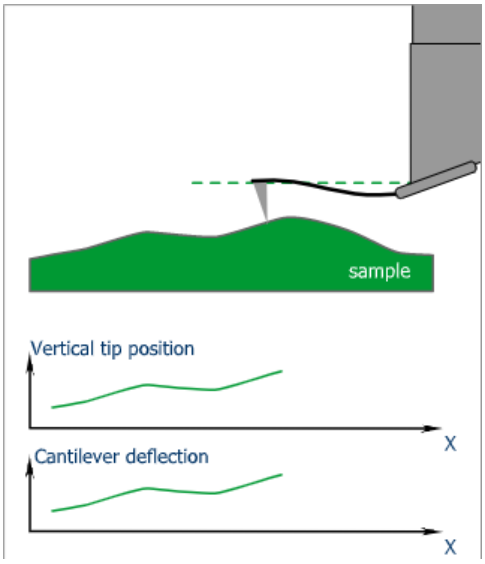

Figure 5.6: Constant Height Mode [63].

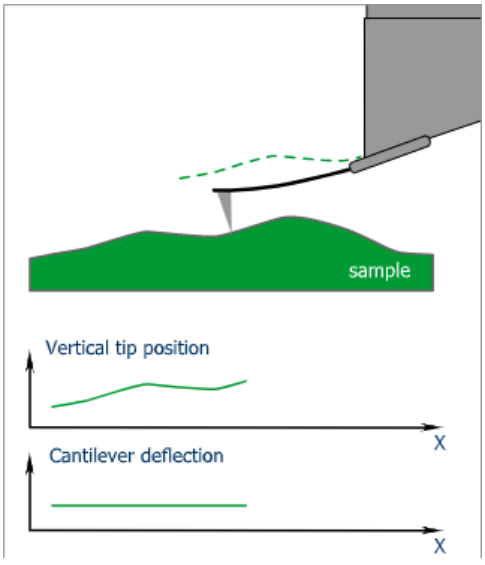

Figure 5.7: Constant Force Mode [63].

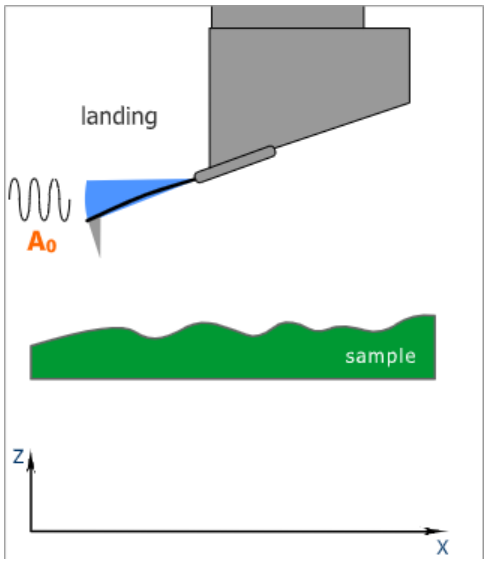

Figure 5.8: Semicontact Mode - tip landing [63].

Semicontact Mode

The dynamic AFM mode is often also called tapping, semicontact or intermittent contact mode. In case of this mode, the cantilever is excited at a fixed frequency f that is below the free resonance frequency f_o. Far away from the surface, the cantilever oscillates with amplitude of A_o (see Fig. 5.8). When the cantilever gets closer to the surface, the resonance curve shifts, but the cantilever is still excited with frequency f.

When the oscillating cantilever approaches the surface, the amplitude of the oscillation decreases (see Fig. 5.9). This decrease in amplitude can be used as the feedback parameter for AFM imaging, similarly like the cantilever deflection in contact mode. However, there is a difference, in the semicontact mode, decreasing the setpoint value increases the force on the sample on contrary to contact mode, where decreasing the setpoint decreases the force on the sample. The resonance behavior of the cantilever is shown in Fig. 5.10. The black curve in Fig. 5.10 B represents the situation far away from the surface and the red curve in Fig. 5.10 B represents the situation close to the surface. When the cantilever gets close to the surface, an additional restoring force acts on the cantilever (the tip sample interaction pushes the cantilever back), and this manifests itself as an increase in the spring constant, which manifests itself in a shift of the cantilever resonance frequency to higher values [61].

Using the change in amplitude as a feedback parameter is called operating the AFM in amplitude modulation (AM) mode. In case of the frequency

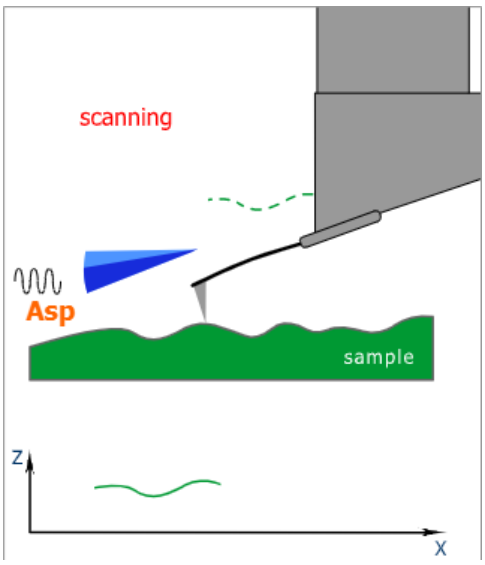

Figure 5.9: Semicontact Mode - scanning [63].

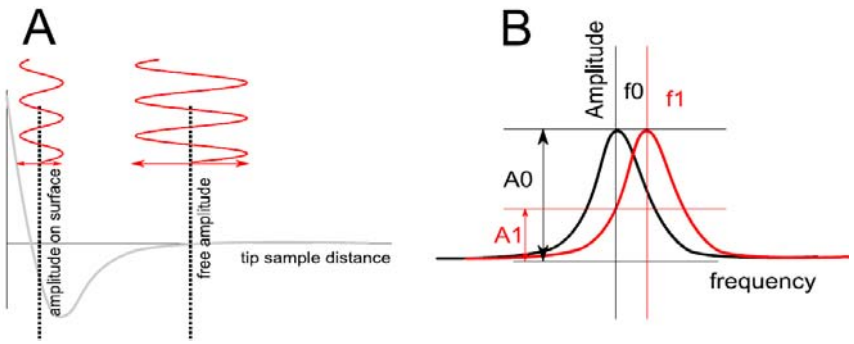

Figure 5.10: Amplitude dependence on the tip-sample distance in semicontact mode [61].

modulated (FM) mode the feedback parameter is the frequency. The amplitude modulation mode is the most common way to operate the AFM. Cantilever for semicontact mode are stiffer than cantilever for contact mode to allow for a higher resonance frequency. Typical values for k are 40N/m and f_o 300-400kHz.

Electrostatic force microscopy modes

The electrostatic force AFM modes are based on the detection of tip-sample electrostatic forces. They include Electrostatic force microscopy (EFM), Kelvin probe force microscopy (KPFM) and probing of local dielectric properties in various configurations including Maxwell stress microscopy and others. These modes were introduced for mapping the variations of electrostatic force, measurements of local surface potential and dielectric permittivity [64]. Electrostatic force microscopy (EFM) is a type of dynamic atomic force microscopy where the electrostatic force between the sample and the conductive tip is probed. This force arises due to the attraction or repulsion of separated charges. It is a long-range force and can be detected 100 nm or more from the sample [60]. In case of the two-pass EFM technique the conductive tip scans the surface to get the topography map. Then, the tip is distanced from the sample surface and records the offsets of the phase signal of the interactions with the gradient of electrical forces present on the surface at the same frequency that in case of scanning. In case of the single-pass EFM technique the conductive tip detects simultaneously the mechanical and electrostatic interactions at different frequencies [64]. This approach requires a use of several lock-in amplifiers in the detection system.

Magnetic force microscopy modes

In case of magnetic force microscopy (MFM) it is possible to map the space distribution of some parameters characterizing magnetic probe-sample interaction, such the interaction force, amplitude of vibrating magnetic probe and the like. This is a two pass technique. In the first pass (see Fig. 5.11) the topography map is acquired in Contact or Semicontact mode. In the second pass the magnetic tip is lifted from the surface (Fig. 5.12) to a certain height from the surface. The tip-sample separation during second pass scanning kept constant. This tip-sample separation must be large enough to eliminate the Van der Waals forces in order to affect the cantilever only by long-range magnetic force. Both the height-image and the magnetic image are obtained simultaneously with this method [63].

The MFM modes may be divided into to categories: DC MFM and AC MFM.

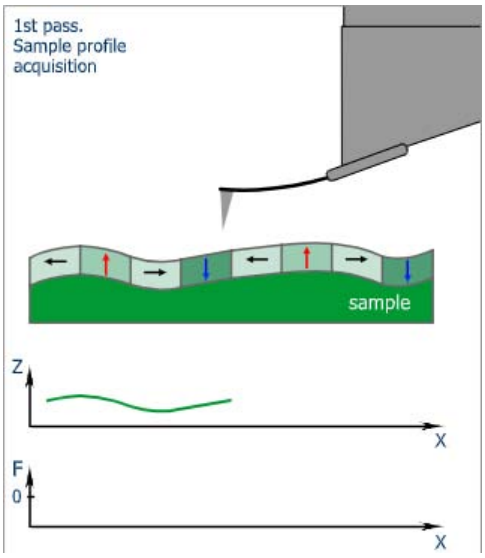

Figure 5.11: Magnetic mode microscopy - topography mapping [63].

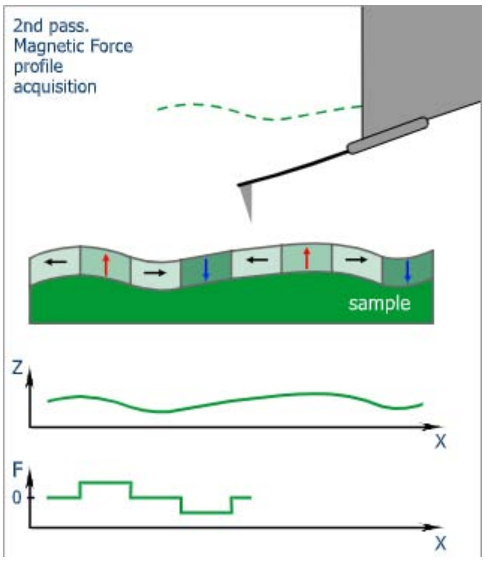

Figure 5.12: Magnetic mode microscopy - magnetic force scanning in DC MFM mode [63].

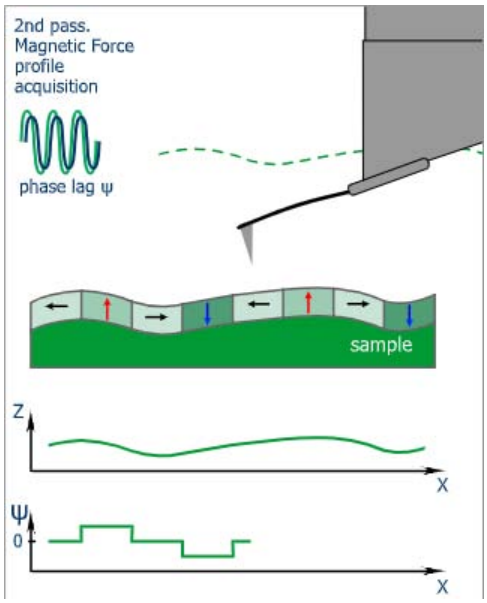

Figure 5.13: Magnetic mode microscopy - magnetic force scanning in AC MFM mode [63].

In case of the DC MFM during second pass the deflection (DFL) of a non-vibrating cantilever is detected. In the AC MFM during second pass the cantilever resonance oscillations are used to detect the magnetic force data (just as in the semicontact mode)(Fig. 5.13).

Force - distance curves

Using the AFM tip it is possible to record force-distance (FD) curves similarly as in case of nanoindentation. The plot of cantilever deflection is obtained as a function of sample position along the z-axis (see Fig. 5.14).

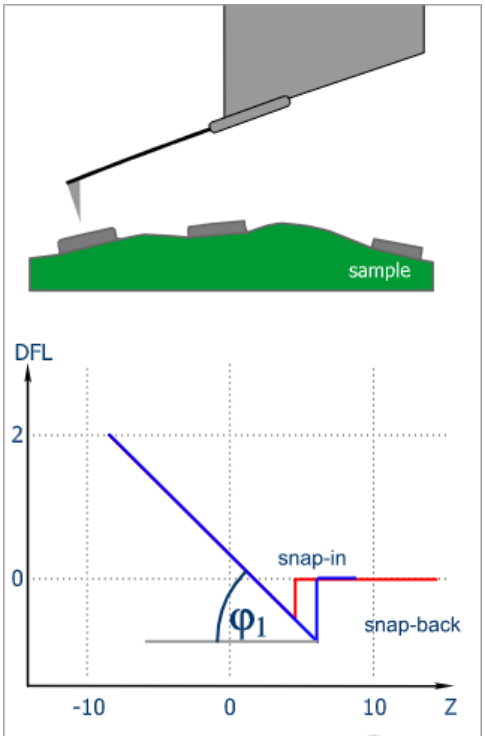

Figure 5.14: Measurement of force - distance curves [63].

Chapter 6

X-Ray Diffraction

Mgr. Pavel Souček, Ph.D.

X-ray diffraction is a widely used non-destructive method of analysis of at least partly crystalline samples. X-ray diffraction is used for identification of the present crystalline phase and for its subsequent quantitative analysis — evaluation of the crystallite size, the lattice parameter, preferential growth orientation and the crystallite strain.

6.1 Theoretical background

In 1912 Max von Laue discovered that crystalline material acts as a three-dimensional grating for X-rays. If we consider that monochromatic X-ray radiation is incident on a polycrystalline material and that all the grains are small and all grain growth orientations are present, only those grains for which the the Bragg diffraction rule is fulfilled will lead to constructive interference of the radiation [57]. A sketch illustrating the Bragg rule is shown in Fig. 6.1.

For the cubic lattice the Bragg diffraction rule can be simply written as

$$2d \sin\theta = \lambda\sqrt{h^2 + k^2 + l^2}, \tag{6.1}$$

where h, k and l are the Laue indices that are calculated by multiplying the Miller indices h_0, k_0 and l_0 by an integer n corresponding to the diffraction order. The diffraction intensity is determined by the structure factor of the unit cell. For different structure types of the unit cell certain Laue indices can be found that provide for zero intensity diffractions. These are the so-called forbidden diffractions. In conditions corresponding to the forbidden diffractions the waves refracted by different planes cancel out. Certain rules for allowed diffractions exist [58]:

- simple lattice — all diffractions are allowed

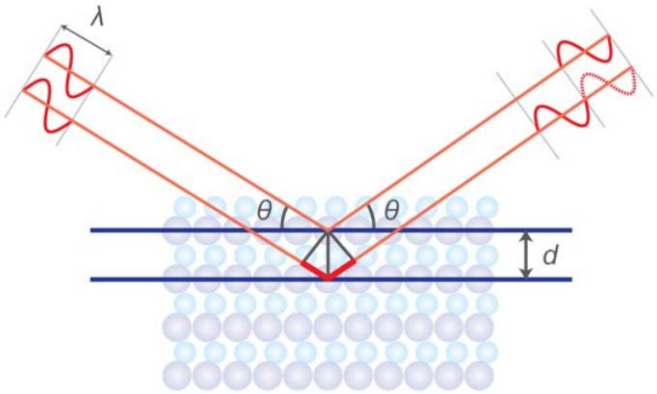

Figure 6.1: A sketch illustrating the Bragg rule. Taken from [65].

- face centred lattice — diffractions with the same parity Laue indices are allowed
- base centred lattice — diffractions with even $h + k + l$ are allowed
- diamond lattice — diffractions with odd Laue indices or diffractions with even Laue indices whose sum is divisible by 4 are allowed

The knowledge of these rules complemented by the knowledge of present elements allows one to identify the present lattice.

6.2 Experimental setup

The simplest geometry used for XRD measurements is the so called focussing Bragg-Brentano geometry. This geometry is sketched in Fig. 6.2. Here, the incident angle ω is defined between the X-ray source and the sample. The diffraction angle 2θ is defined between the incident beam and the detector and the incident angle ω is always $1/2$ of the 2θ angle. The diffraction vector (vector that bisects the angle between the incident and scattered beam) is always normal to the sample surface.

The X-rays are produced by a sealed tube or a rotating anode. Both work on a principle of X-ray generation by striking of an anode (copper in our case) with an electron beam from a heated tungsten filament. Copper K_α line is used for the measurement.

The X-rays from the source go through X-ray optics in a divergent ray towards the sample. There the diffraction occurs and the X-rays are scattered in a sphere around the sample in the so called Debye diffraction cone. A

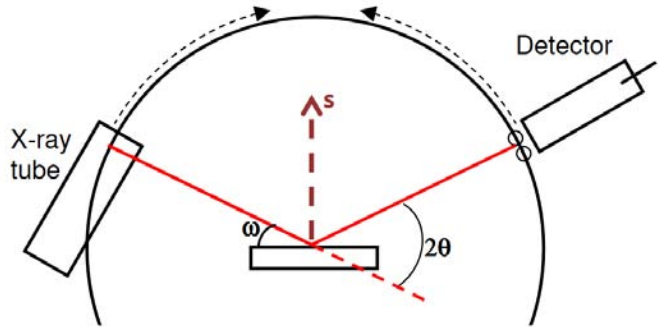

Figure 6.2: A sketch of the Bragg-Brentano geometry. Taken from [66].

certain part of this cone intersects the detector after going through more optics. The signal on the detector consists of the record of photon intensity versus the 2θ angle.

6.3 Data analysis

The diffraction pattern is a fingerprint of the diffracting material. Based on the diffraction peak position, its width and its relative intensity in the diffraction pattern the present phase can be positively matched to a database pattern. Databases can consist of either measured data like the Powder Diffraction File (PDF) of of calculated data such as the Crystallography Open Database.

The lattice parameter can be calculated directly from the Bragg diffraction rule, whereas the simplest way of calculation of the crystallite size comes from using the Scherrer equation [67]. The Scherrer equation can be written as

$$\tau = \frac{K\lambda}{\beta \cos\theta}, \tag{6.2}$$

where K is the dimensionless shape factor (0.94 for round grains), λ is the X-ray wavelength, β is the full width at half maximum of the diffraction peak and θ is the Bragg diffraction angle. The Scherrer equation presents the simplest case, where the total peak broadening is attributed only to the grain size and the strain is neglected. This approach is sufficient for powder samples, whereas care needs to be taken for thin films. The grain strain can be estimated either by different treatment of the measured data (Williamson-Hall analysis) or by measurements in special geometry.

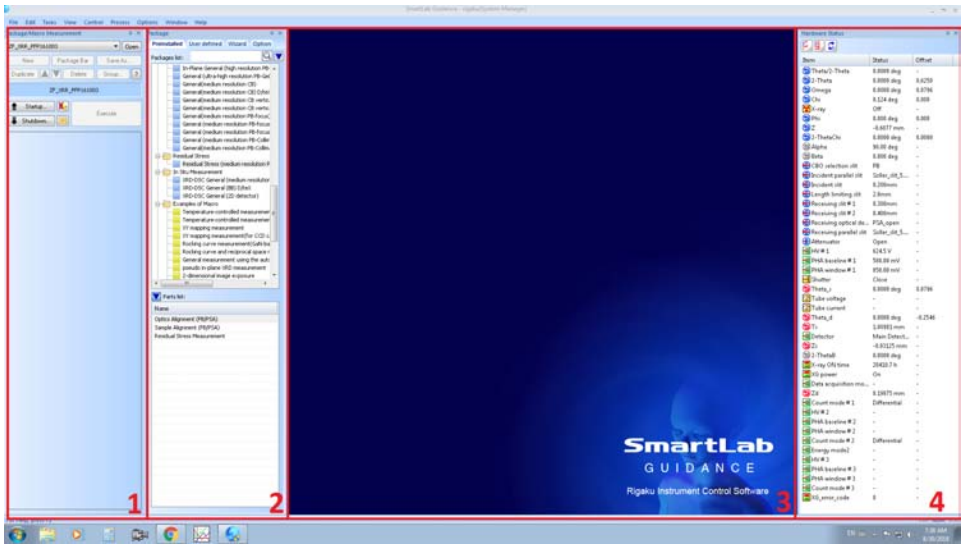

Figure 6.3: SmartLab Guidance — main screen.

6.4 Practical aspects of X-ray diffraction

XRD is a powerful fast non-destructive method of crystalline sample analysis. Minimum preparation of the sample is needed, however, some experience is needed to understand the acquired data. First source of confusion comes from the nature of the X-ray radiation. The K_α line is a doublet of $K_{\alpha 1}$ and $K_{\alpha 2}$ lines. Their separation is especially visible for diffractions at higher 2θ angles. Moreover diffractions caused by K_β and W_α lines can be visible. Their intensity can be reduced by using a nickel filter in the path of the signal from the sample to the detector. However, these lines can be present in the measured pattern. Secondly, knowledge of the present elements is immensely useful for the identification of the present phase. The diffraction pattern of the substrate must be also taken into consideration.

6.5 Measurement

The practical measurements will utilize Rigaku Smartlab X-ray diffractometer with copper sealed-tube X-ray source. The device is controlled via SmartLab Guidance software. The main screen is sown in Fig. 6.3. The left-hand panel (no. 1) shows the steps in the currently selected recipe or macro, panel no 2. is for selecting macros, the central panel 3 shows the detector output, i.e. the measurement data and the right-hand panel 4 shows the current state of the machine.

Any measurement generally consists of 3 steps:

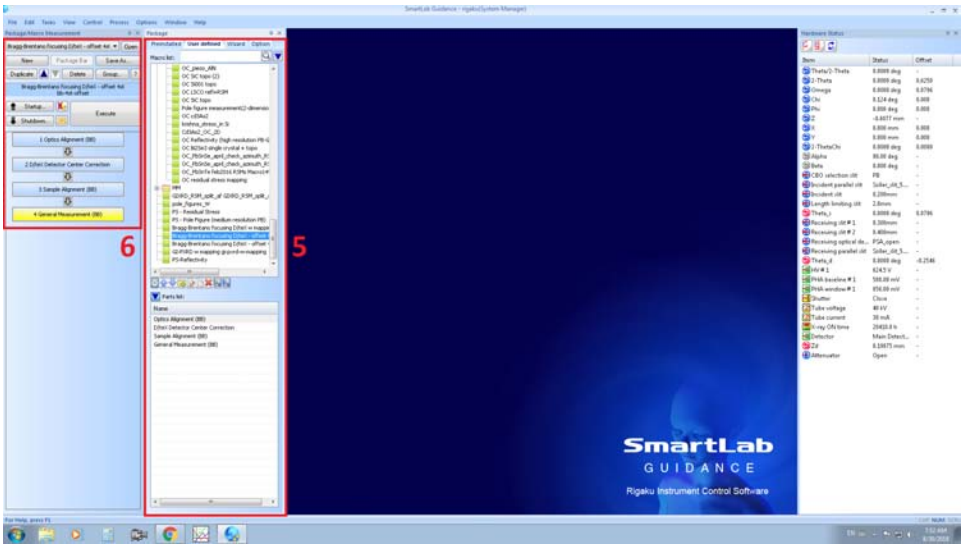

Figure 6.4: SmartLab Guidance — measurement macro.

1. optics calibration
2. sample positioning calibration
3. measurement.

Example of such a measurement is shown in Fig. 6.4. A macro for XRD measurement in the Bragg-Brentano configuration was selected in panel 5 and its parts is shown in panel 6. The first two steps are the calibration — the optical path is calibrated in step 1 and the used detector is calibrated in step 2. The measured sample is introduced into the measurement chamber after step 2 and is aligned with the X-ray beam in step 3. The measurement itself is step 4.

The measurement is set-up by clicking on the yellow highlighted measurement step. A popup window appears as is show in Fig. 6.5. Here the measurement can be configured for any specified sample. The most relevant fields are the Start and Stop angles and the Speed of the measurement in degrees per minute. The longer the measurement, the lower the noise. However, this relation is not linear but a square root one. Therefore, if you want to reduce the noise twice, you need to set the measurement four times as long and the measurements can become very time consuming. The measurement is started by clicking on the execute button.

When the measurement is finished, the measured peaks can then be indexed according to the aforementioned rules and the crystallite size and the lattice parameter can be calculated as well. An example of measured data of cubic TiC can be seen in Fig. 6.6.

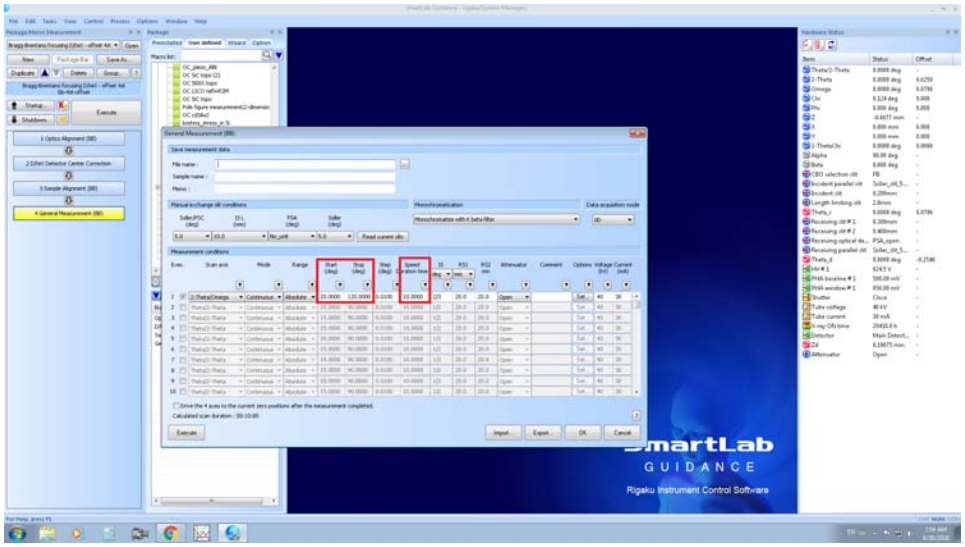

Figure 6.5: SmartLab Guidance — measurement setup.

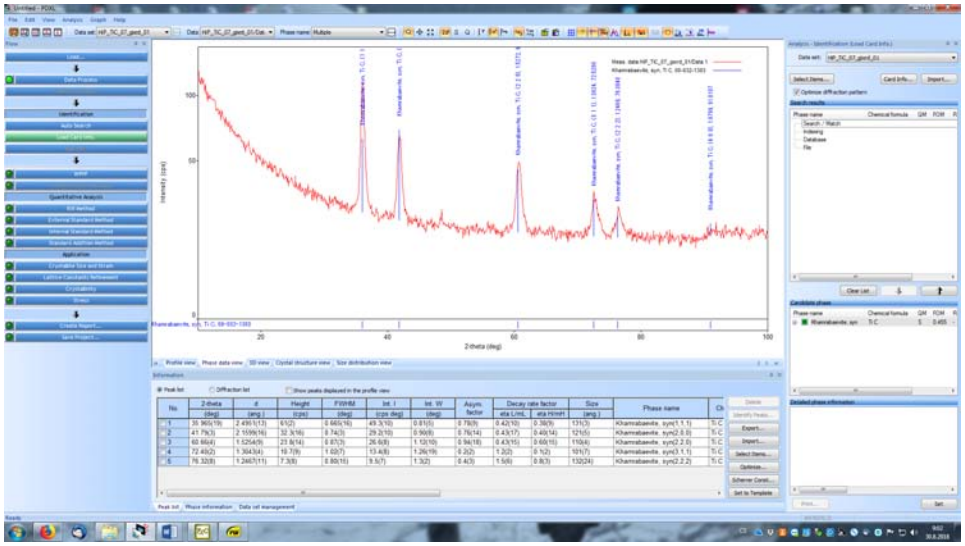

Figure 6.6: X-ray diffractogram of TiC.

Chapter 7

X-Ray Photoelectron Spectroscopy

RNDr. Monika Stupavská, PhD.

X-ray photoelectron spectroscopy (XPS) is a surface analytical technique that has become into an essential tool for material characterization. XPS is at present a widely utilized method of studying the qualitative and quantitative composition of surfaces of materials and represents a unique combination of surface sensitivity and chemical specificity as well as relatively straightforward means of quantification.

7.1 Basic principles

In XPS, the sample is irradiated with low energy X-rays $h\nu$ (controlled), in order to provoke the photoelectric effect (Fig. 7.1). As a result, emission of photoelectrons is observed. Kinetic energies of these electrons can be described most simply by the photoelectric equation:

$$h\nu = E_b + E_k, \tag{7.1}$$

where, E_b is the binding energy (unknown variable) and E_k is the photoelectron kinetic energy (measured by XPS Spectrometer). The equation will calculate the energy needed to get an electron out from the surface of the solid. Knowing E_k and $h\nu$, the E_b can be calculated.

Each element produces a characteristic set of XPS peaks at characteristic binding energy values that directly identify each element on the surface, therefore photoemission spectra can serve as fingerprints of the respective elements. Almost all elements except for hydrogen and helium can be identified via measuring the binding energy of its core electron. Furthermore, binding energy of core electron is very sensitive to the chemical environment of element. The same atom is bonded to the different chemical species, leading to the change in the binding energy of its core electron. The variation

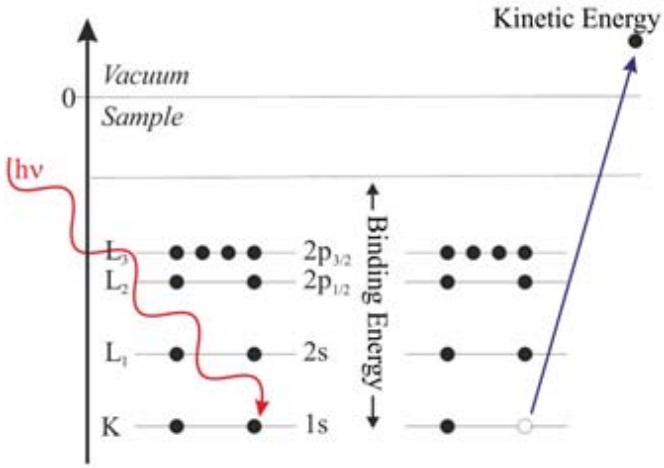

Figure 7.1: Principle of photoelectron emission [68].

of binding energy results in the shift of the corresponding XPS peak. This effect is termed as chemical shift, which can be applied to studying the chemical state of element on the surface. Therefore, XPS is also known as electron spectroscopy for chemical analysis (ESCA).

XPS is used not only to identify the elements but also to quantify the chemical composition. The number of detected electrons in each of the characteristic peaks is directly related to the amount of the element within the irradiated volume. The atomic concentration of an element, C_i, can be expressed as:

$$C_i = \frac{I_i/S_i}{\sum_i I_i/S_i}, \tag{7.2}$$

where I_i is the peak intensity for element i , and S_i is the sensitivity factor for the peak i.

The ejection of an electron from an inner shell (Fig. 7.2A-B) creates an unstable electronically excited state with a core hole in that shell. This excited state can decay via two distinct de-excitation routes:

- Auger decay
  The core hole is filled by an electron from an outer shell and the excess energy is transferred to another outer shell electron, which is emitted (Fig. 7.2C). The process involves three electrons: the electron knocked out in the initial photoionization event, the electron that decays to fill the inner shell vacancy, and the emitted electron from the outer shell (Auger electron). Auger transitions are labelled for the orbital shells involved in the transitions. For example, in a KLL transition the electron that leaves behind the initial core hole is from the K shell (1s

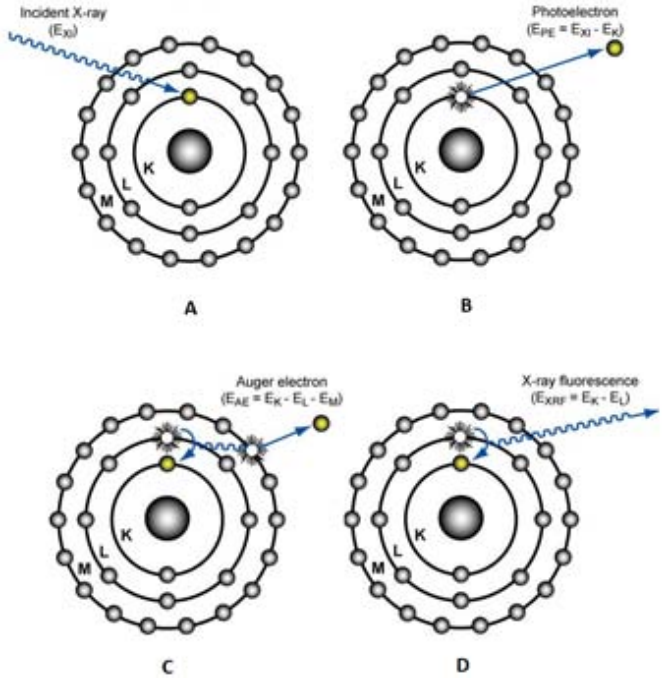

Figure 7.2: Schematic of (A-B) photoionization, (C) Auger decay, (D) X-Ray fluorescence

state), while the other two electrons come from the L shell (2s or 2p levels).

- X-ray emission process or X-ray fluorescence
  The core hole is filled by an electron from an outer shell with simultaneous emission of a photon with energy equal to the difference in binding energy of the two levels involved in the electron transition (Fig. 7.2D)

X-ray fluorescence and Auger electron emission are competitive processes, the branching ratio of which is governed by the respective decay cross-sections. Generally, elements with low atomic number prefer the non-radiative decay.

7.2 Surface sensitivity

All electron spectroscopies are highly surface sensitive, due to the strong interaction of electrons with matter. X-rays penetrate a few micrometers into the sample surface, and photoelectrons are generated throughout the irradiated volume. The XPS experiments are mainly concerned with the

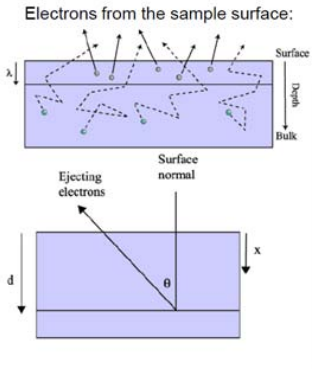

$$I(d) = K\int_0^d \exp\left(\frac{-x}{\lambda\cos\theta}\right)dx$$

Fraction of signal from various depth in term of λ

Depth	Equation	Fraction of signal (θ= 0)
λ	$\frac{I(\lambda)}{I(\infty)} = \frac{\int_0^{\lambda}\exp\left(\frac{-x}{\lambda\cos\theta}\right)dx}{\int_0^{\infty}\exp\left(\frac{-x}{\lambda\cos\theta}\right)dx}$	0.63
2λ	$\frac{I(2\lambda)}{I(\infty)} = \frac{\int_0^{2\lambda}\exp\left(\frac{-x}{\lambda\cos\theta}\right)dx}{\int_0^{\infty}\exp\left(\frac{-x}{\lambda\cos\theta}\right)dx}$	0.86
3λ	$\frac{I(3\lambda)}{I(\infty)} = \frac{\int_0^{3\lambda}\exp\left(\frac{-x}{\lambda\cos\theta}\right)dx}{\int_0^{\infty}\exp\left(\frac{-x}{\lambda\cos\theta}\right)dx}$	0.95

Figure 7.3: Parameters affecting XPS information depth [69, 70].

intensity of emitted photoelectrons that have suffered no energy losses, e.g. electrons can travel without undergoing inelastic scattering events. Those photoelectrons produced close to the surface will be able to escape in to the vacuum of the spectrometer without colliding with something on the way out. Quantity describing the average distance that an electron can travel through the material without suffering energy losses by inelastic scattering, is the inelastic mean free path λ_e, which is defined as the average distance that an electron of given kinetic energy E_{kin} travels between two successive inelastic collisions (Fig. 7.3). The sampling depth of the XPS experiment is often defined as $3\lambda_e$, which means that 95% of the photoemission intensity comes from the corresponding region below the surface. So the sampling depth ($3\lambda_e$) for XPS under these conditions is 3-10 nm. Those electrons produced deeper down will lose energy before reaching the surface, thus contributing to the background of the measured spectrum.

7.3 Primary structures in XPS

A typical XPS spectrum is obtained at a given photon energy by recording the number of photoelectrons as a function of the kinetic energy and can be plotted as a function of the binding energy. This spectrum, often called survey spectrum or wide scan, allows a complete elemental analysis. Fig. 7.4 represents the survey spectra of plasma treated polylactic acid surface. As can be seen, spectrum displays a series of signals correspond to carbon, oxygen and nitrogen. Survey scans give qualitative information about atoms/molecules present in the sampling depth. The relative intensities of the different photoelectron peaks reflect both the surface atomic abundance and the probability of photoemission from a given energy level. After having identified the elemental composition, it is then possible to acquire detailed "high resolution" scan of any single energy level. An example of detailed

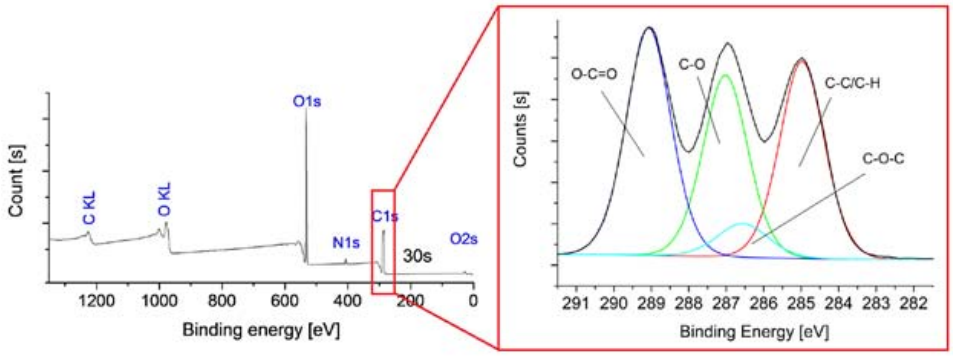

Figure 7.4: Wide scan and high resolution C1s scan of plasma treated polylactic acid surface [71].

scan relevant to the C 1s region, selected from a previous investigation, is shown in Fig. 7.4 on the right. High resolution scans show the subtle shifts in energy of photoelectrons originating from different chemical environments.

7.4 Chemical shift

Binding energies of a given element are not fixed values because the exact value of E_b reflects the chemical environment of the surrounding atoms and that energy shifts may occur when inequivalent atoms of the same elemental species are present (Fig. 7.5A). These energy shifts are called chemical shifts. Variations in the elemental binding energies arise from differences in the chemical potential and polarizability of compounds. The chemical shift range for any element is quite small, typically less than 10 eV. Usually species of a higher positive oxidation state are shifted towards higher binding energy due to the extra coulombic interaction between the emitted electron and the ion core (Fig. 7.5B). The core level C1s peak of a polyethylene terephthalate in Fig. 7.5A shows a clear shift in binding energy, related with differences in the chemical environment of the carbon. Based on these shifts, it is possible to determine 4 carbon chemical bonds: C-C/C-H at 284.8 eV, C-O at 286.5 eV and COO at 288.9 eV. The values of the binding energy shifts can often be used to determine oxidation states and the nature of the chemical bond formed by the atoms, although the shifts are normally quite small, and often peak fitting routines need to be used because they overlap in binding. This ability to discriminate between different oxidation states and chemical environments is one of the major strengths of the XPS technique.

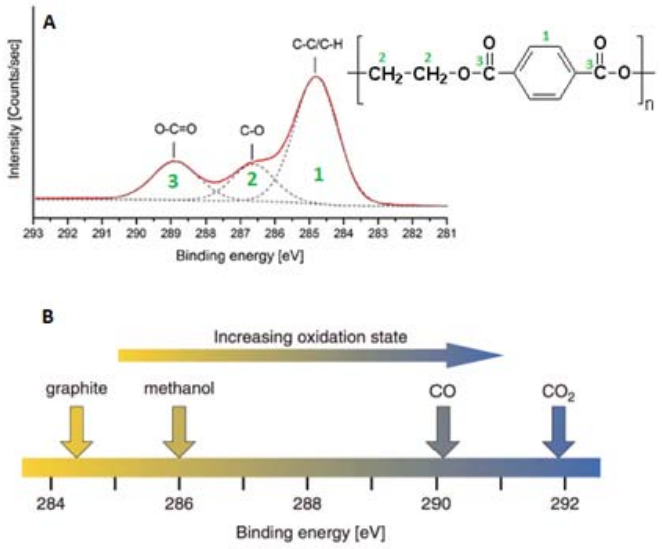

Figure 7.5: (A) Chemical shifts of C1s core level peak of polyethylene terephthalate, (B) A plot of the chemical shift in the C1s binding energy in different carbon - containing compounds [72].

7.5 Spin-orbit splitting

The photoemission process is inherently a many-electron event. All of the other electrons in the system must readjust their positions and energy since they are no longer in their ground electronic states. Splitting of core level peaks can occur when the system has unpaired electrons in the valance levels. The energy of a level varies according to the total angular momentum, $j = l+s$. States with $l > 0$ can have two possible j values: $j = 1-\frac{1}{2}, 1+\frac{1}{2}$ for $l = 1(p)$, or $j = 2-\frac{1}{2}$, or $j = 2+\frac{1}{2}$ for $l = 2(d)$, etc. In the XPS spectra this results in pairs of peaks with relatively close values of the binding energy as well as intensity as illustrated in the Fig. 7.6A which shows a doublet of Palladium. The intensity ratio of the two spin-orbit components is dictated by the ratio of the respective multiplicities: which determines the relative probability of transition to the two states upon photoionization. Generally, in the photoemission spectrum from a given subshell the core level sub-peak with maximum j is detected at lower binding energy. Obviously, no spin-orbit splitting occurs in the photoemission from s core levels. The theoretical peaks area ratio is based on the degeneracy of each spin state of the doublet. In the case of energy levels having quantum number $l = 1$, as in the case of the $2p_{1/2}/2p_{3/2}$ doublet, the peaks area ratio is 1/2, while in the case of the $3d_{3/2}/3d_{5/2}$ doublet the peak area ratio is 2/3 and, in the case of the $4f_{7/2}/4f_{5/2}$ doublet, the peak area ratio is 3/4 (Fig. 7.6B).

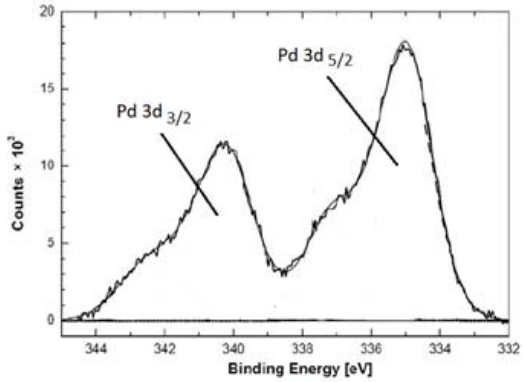

A

Spin-orbit split doublets

Sub-shell	*j* values	Area ratio
s	1/2	-
p	1/2; 3/2	1: 2
d	3/2; 5/2	2: 3
f	5/2; 7/2	3: 4

B

Figure 7.6: (A) Spin - orbit coupling leads to a splitting of the 3d photoemission line of palladium into a doublet [73], (B) Table listing spin-orbit split components and intensity ratios for different subshell

7.6 Surface charging

Many sample specimens have electrically insulating properties that would affect the XPS binding energy measurements. These samples can exhibit charging. This problem arises since photoelectrons emitted from the sample are not replaced by electrons from the ground due to poor conductivity. For nonconducting surface, electrons cannot return to the surface easily and are lost faster than they return. After a steady state is reached, a positive charge develops due to deficiency in electron density. Photoelectrons from the analyte would thus be ejected with a decreased kinetic energy (higher binding energy) along with broadening of the peak full width half maximum. Measurements of binding energy for these systems involve flooding of the sample surface with low energy secondary electrons to neutralize the charge.

7.7 Analysis features

7.7.1 Imaging & mapping

XPS can also be used to image the surface of a sample. This is useful in understanding at the distribution of chemistries across a surface or for finding the limits of contamination. There are two approaches for obtaining XPS images: mapping (serial acquisition) or parallel imaging (parallel acquisition).

Serial acquisition of images is based on a two-dimensional, rectangular array of small-area XPS analyses. This method enables measurements of the

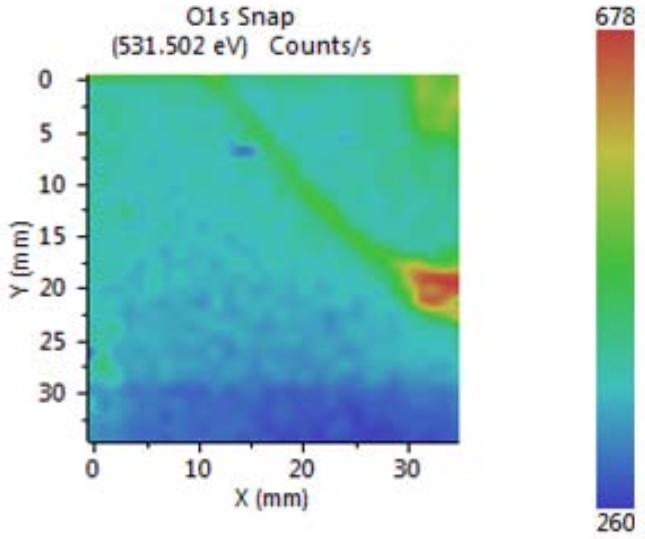

Figure 7.7: XPS map of oxygen distribution on the surface of treated polystyrene [74].

distribution of elements or chemical states (Fig. 7.7). The ultimate spatial resolution in the image is determined by the size of the smallest analysis area an is $\sim$ 15 µm for ESCALAB 250Xi. Serial acquisition is generally slower than parallel acquisition but can collect a range of energies at each pixel compared to collecting only a single energy for parallel acquisition.

Parallel acquisition of photoelectron images simultaneously images the entire field of view. The spatial resolution of parallel imaging depends on the spherical aberrations of the lens. This method of imaging is fast and produces the best possible imaging resolution. Fig. 7.8 illustrates the combined use of parallel imaging, high energy resolution, excellent sensitivity and optimum charge compensation. It shows high resolution chemical state images from a sample consisting of carbon fibres on a polyethylene terephthalate (PET) substrate. This is a particularly challenging sample for XPS imaging studies because the substrate is an insulator while the fibres have some conductivity. Moreover, the sample is not flat, contributing further to the dangers of differential surface charging [75].

7.7.2 Depth profiling

Depth profiling uses an ion beam to etch layers of the surface or surface contamination, revealing subsurface information. The surface is etched by rastering an Ar ion beam over a square of the sample. After the etch cycle, the Ar beam is blanked and another set of spectra is recorded. This sequence of etching and spectrum acquisition is repeated until profiling has proceeded

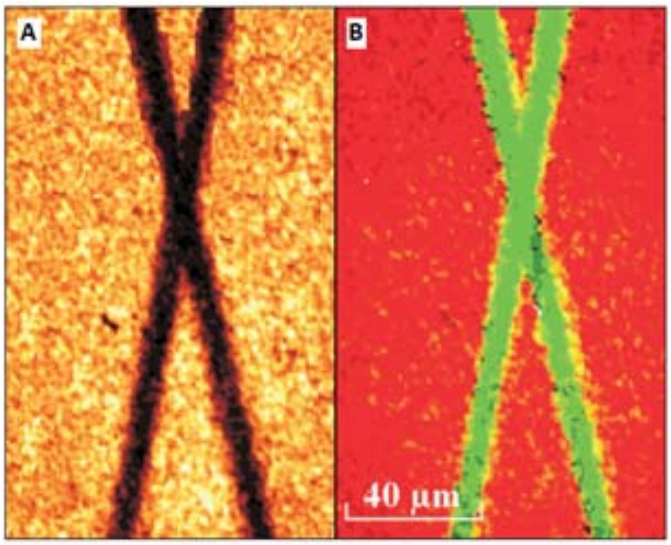

Figure 7.8: (A) C1s image of the carbon fibers on the PET substrate, (B) color overlay image showing two chemical states of carbon [75].

to the required depth and provides quantitative information. The damaged part of the surface can be a few nanometers thick depending on the surface material, the density and energy of the argon ions [75]. The results for the Al_2O_3 film on the Si wafer are plotted in Fig. 7.9. Concentrations for Al, O, C, and Si were quantified as a function of sputtering time. For Al_2O_3 on the Si, the Al concentration decays to zero at a sputtering time of 270 s. The O concentration decays to zero later than the Al concentration because of the SiO_x interlayer [76].

7.7.3 Angle resolved XPS (AR-XPS)

Using angle resolved XPS it is possible to characterize ultra-thin films without sputtering. Unlike depth profiling with ion sputtering, AR-XPS is capable of non-destructive analysis of areas deep down to the escape depth of photoelectrons. From Beer-Lambert equation, it is clear that the depth of analysis is dependent on the angle of electron emission. This technique varies the emission angle at which the electrons are collected, thereby enabling electron detection from different depths. This is usually undertaken by tilting the sample with respect to the analyzer. AR-XPS provides information about the thickness and composition of films and can be applied to films that are too thin to be analyzed by conventional depth profiling techniques.

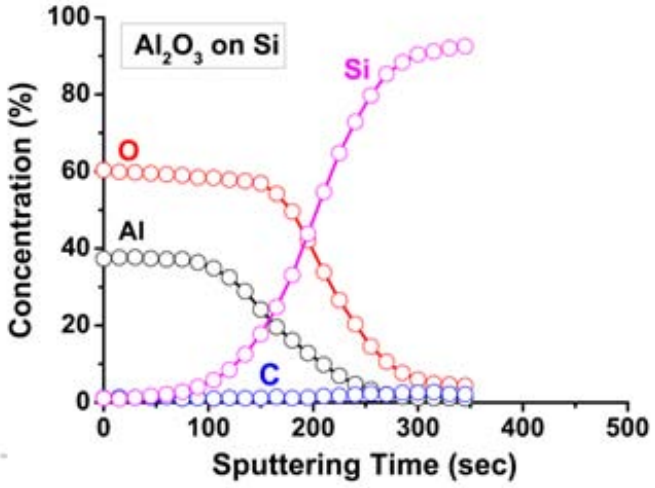

Figure 7.9: XPS depth profiles for the Al_2O_3 film deposited on the Si wafer [76].

7.8 Experimental set-up

7.8.1 Vacuum system

The sample analysis is conducted in a vacuum chamber, under the best vacuum conditions achievable, typically $\sim 10^{-10}$ mbar. XPS is a surface sensitive method. Impurities can play a major role in the observed spectra and most of the effort that goes into the sample handling directly involves this problem. The first criterion then is that a good vacuum is needed to maintain the integrity of the surface. In general, 10^{-6} mbar would be sufficient to allow the photoelectron to reach the detector without suffering collisions with other gas molecules. On the other hand, 10^{-9} mbar is required to keep an active surface clean for more than several minutes [77]. Even in the case of a vacuum of 10^{-9} mbar, typically carbon peaks are found as a result of surface contamination. Therefore, often the sample is cleaned by a slight sputtering.

7.8.2 X-ray source

In XPS instruments, X-rays are generated by bombarding a metallic anode with high-energy electrons. The energy of the emitted X-rays depends on the anode material and beam intensity depends on the electron current striking the anode and its energy. Electrons are emitted from a bright source, such as LaB_6, and focused onto a water-cooled, aluminum anode. A small portion of the bombarding electrons cause vacancies in inner electron shell of the

target atoms and electrons from higher levels fall to fill the vacancies with the simultaneous emission of X-ray photons. If the electrons fall from the L shell to the K shell, then the X-ray is designated $K_{\alpha 1}$; if it is produced by an L_2 shell to K shell transition it is designed $K_{\alpha 2}$. In case of aluminum, the Al K_α X-ray line consists of doublet with the $K_{\alpha 1}$ (at 1486.70 eV) having twice the intensity of the $K_{\alpha 2}$ (at 1486.27 eV). In addition to the characteristic $K_{\alpha 1}$, 2 lines, there are other features in the X-ray emitted. There is a K_β line as well as satellite lines arising from doubly ionized atoms [78–80]. The wavelength of X-ray must be restricted precisely in order to remove the satellites (associated X-rays of different energies, which are less intense than the primary, and preferred, X-ray) from the Al K_α X-ray line. This ensures that the energy imparted to photoelectrons will be precise. Therefore some of the X-rays emitted from the anode are intercepted by the crystal and a monochromated beam of X-rays is focused onto the sample. The size of the X-ray spot at the sample is equal to the size of the electron beam spot on the anode. Therefore the analysis area can be controlled by controlling the electron beam spot size.

7.8.3 Electron energy analyser

Electrons ejected from the surface enter the input lens, which focuses the electrons and retards their energy for better resolution. A lens system focuses the electron beam into a hemispherical analyser. This analyser consists of two plates carrying a potential, so that only electrons with a small range of energy differences reach the exit. Finally, an electron detector analyses the electrons (Fig. 7.10A). Hemispherical analyser disperses electrons inside two hemispheres with applied voltages V_1 and V_2 ($V_2 > V_1$), and the dispersion depends on these voltages and on the kinetic energy of the photoelectrons. It means that the hemispherical analyser behaves like an energy filter.

Potential of mean path through analyser is:

$$V_0 = \frac{V_1 R_1 + V_2 R_2}{2R_0} \tag{7.3}$$

The figure 7.10B shows schematically how this happens. An electron of kinetic energy $eV = V_0$ will travel through a circular orbit through hemispheres at radius R_0. Since R_0, R_1 and R_2 are fixed, in principle changing V_1 and V_2 will allow scanning of electron kinetic energy following mean path through hemispheres. Once the electron is focused to the back of the analyser, it is counted by a channeltron detector.

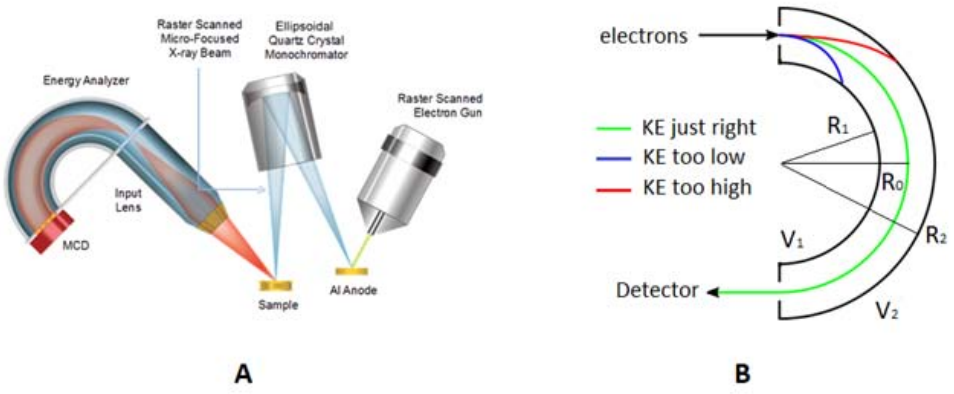

Figure 7.10: (A) Schematic diagram of the major components of XPS, (B) Path of photoelectrons in a concentric hemispherical analyser [81].

7.8.4 Sample handling

Samples that can be analysed by XPS are all solids ranging from films, powders to frozen liquids including inorganic compounds, metal alloys, semiconductors, polymers, elements, glasses, ceramics, papers, inks, woods, plant parts, bio-materials and many others. In majority of XPS applications, sample preparation and mounting are not critical. Typically, the sample is mechanically attached to the specimen holder, and analysis is begun with the sample in as-received condition. Additional sample preparation is discouraged in many cases because any preparation might modify the surface composition. Argon etching is a long-established method for in-situ sample cleaning. It can be highly effective at removing thin oxide layers of contamination but also can leave significant damage.

Chapter 8

Raman Spectroscopy

Mgr. Pavel Souček, Ph.D.

Raman spectroscopy is a light-scattering based method for investigation of the molecules on the surface of the studied material. It is based on the change in the polarizability of the molecules due to their interaction with the incident monochromatic light beam [82]. These observed specific energy transitions arise from specific molecular vibrations. When the energies of the transitions are plotted as a spectrum, they can provide a "molecular fingerprint" of the molecule. Raman spectroscopy is a complementary method to the infrared spectroscopy, where the observed signal arises from a change in the dipole moment of a molecule. Often molecules that are infra-red inactive are not Raman active and vice versa.

8.1 Theoretical background

When light is scattered in matter, it can be scattered elastically or inelastically. The incident light interacts with the molecule and distorts the electron cloud which forms a virtual state. This state is unstable and the photon is re-radiated very fast. Most photons are scattered elastically, i.e. they undergo the so called Rayleigh scattering, where the excited electron in the molecule falls onto the same level it has been excited from, and their energy and hence also their wavelength is the same as of the incident photons. Raman spectroscopy uses the approximately 0.00000001 – 0.000001 % of photons that are scattered inelastically and undergo the so called Raman scattering [83]. Both these processes are shown in Fig. 8.1. Raman scattering can be further divided to Stokes and anti-Stokes scattering. In Stokes scattering part of the energy from the photon is transmitted to the molecule and it is excited from the ground level to a higher vibrational level. The scattered photon therefore has lower energy and a higher wavelength than the incident photon. In anti-Stokes scattering the energy is transmitted the other way. The molecule that is originally in a higher vibrational level is

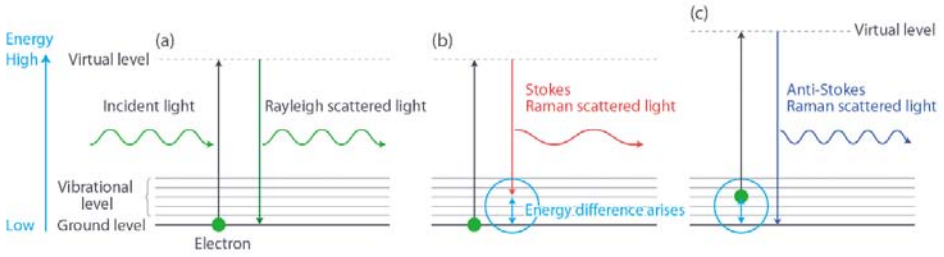

Figure 8.1: Scattering of light in matter. Taken from [83].

de-excited into the ground level. The scattered photon therefore has higher energy and shorter wavelength than the incident one. As low number of molecules is excited into a higher vibrational level at room temperature, the anti-Stokes scattering is less likely to occur than the Stokes scattering by several orders of magnitude.

8.2 Experimental setup and data acquisition

A typical Raman spectroscopy system is composed of one or several lasers with an optical path focussed on a sample holder. The optical signal is then directed to a grating splitting the signal to its spectral components. These are gathered by a CCD detector [84].

The actual system used in this laboratory is the Horiba LabRam HR Evolution shown in Fig. 8.2. The system is equipped with 3 lasers — 325 nm UV, 532 nm VIS and 785 nm IR. Each laser has certain advantages as well as disadvantages and sometimes it is necessary to measure a sample with more than one laser. The system is in a confocal configuration meaning that the laser goes through a confocal objective lens with a very shallow depth of field to the sample as well as back from the sample towards the gratings and the detector. The system is equipped with two gratings in the device itself — 600 mm^{-1} and 1800 mm^{-1}. A third grating of 1200 mm^{-1} can be swapped manually with the 1800 mm^{-1} grating. The signal is collected by a CCD detector cooled to -60 degrees centigrade to reduce the signal noise.

The Raman spectrometer is controlled via LabSpec 6 software. The main screen of the software os shown in Fig. 8.3. The device settings are done in the righthand bar (highlighted as no. 1 in Fig. 8.3), whereas the direct device control is done by the top icon row (highlighted as no. 2 in Fig. 8.3).

First the laser needs to be chosen in the righthand bar in the instrument setup panel. The appropriate Range needs to be set as well — Visible range for 532 nm and 785 nm lasers and UV range for the 325 nm laser. The appropriate objective needs to be set with regards to the used laser and the

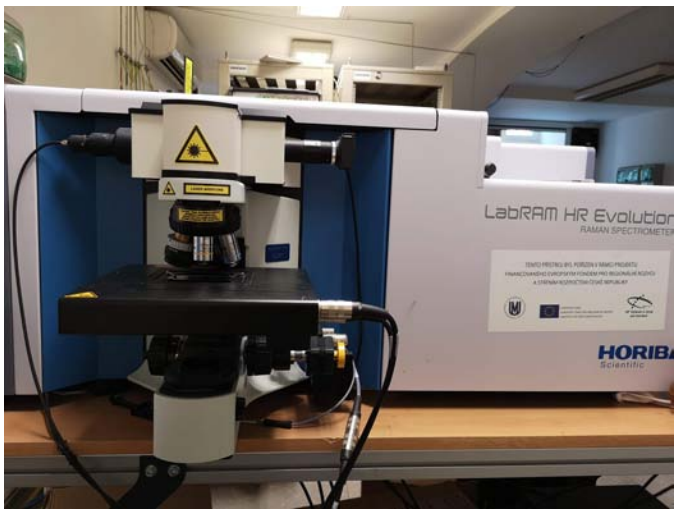

Figure 8.2: Horiba LabRam HR Evolution

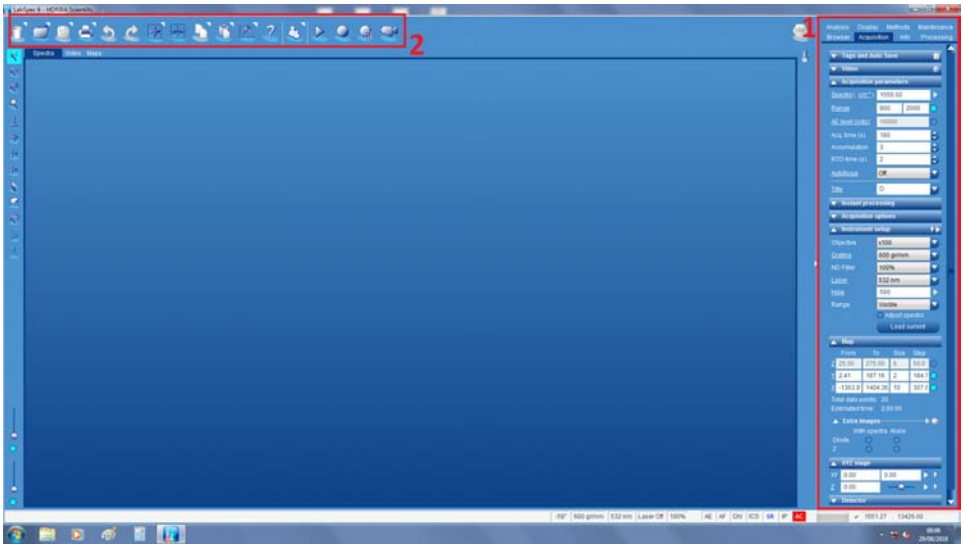

Figure 8.3: LabSpec6 — main screen

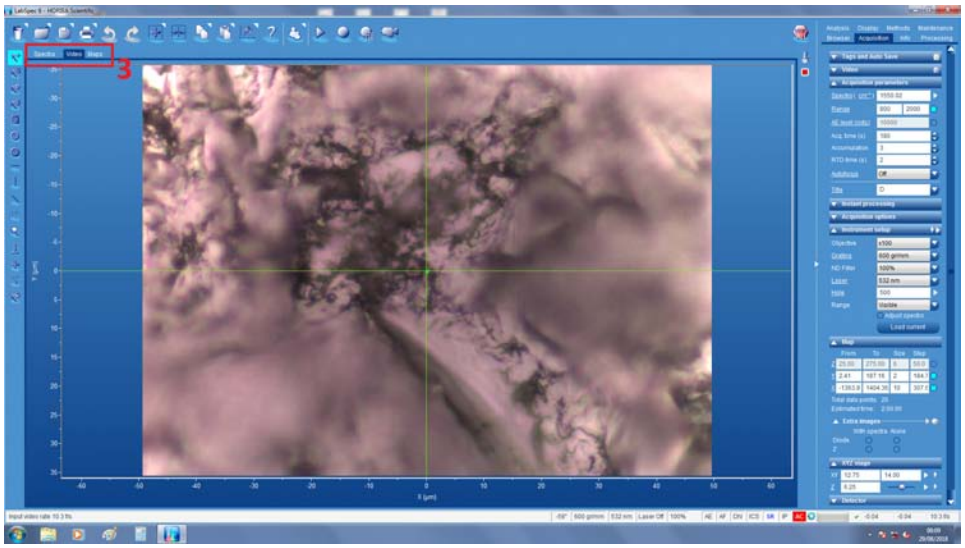

Figure 8.4: LabSpec6 — sample focussing

sample. The lens 10x, 50x and 100x objectives are suitable for the 532 nm and 785 nm lasers, while the mirror xCG 74x objective needs to be used for the 325 nm laser.

Before the first measurement of the day or in any new laser-objective combination the calibration of the device needs to be performed due to sensitivity of the device to to external parameters such as the temperature. The calibration is done on a Si sample due to very simple Raman spectra of silicon. The silicon reference sample is put on the sample holder and the software is switched to the Video tab as is shown in Fig. 8.4. The sample is focussed by moving it up and down. The first rough focussing is done by a rotating slider on either side of the sample holder. Fine adjustments are done by a joystick connected to the spectrometer. Once the sample is focussed, the calibration can be performed. The easiest calibration — autocalibration — can be done for the 532 nm visible laser. This can be done by clicking oh the red AC sign on the bottom of the screen (see Fig. 8.5). Then select Current Auto Calibration to perform the calibration in the currently selected setup. The calibration is done in two steps - first the Rayleigh-scattered signal is set to 0 cm^{-1} and then the Stokes first order scatter peak of Si is set to 520.7 cm^{-1}. This way we have 2 points and the output of the CCD can be linearised. The AC sigh turns green after successful autocalibration.

The measurement of the investigated sample can be done after the device is calibrated. The measurement range and length need to be set up now in the Acquisition parameters tab as is shown in Fig. 8.6 — box 5. The example range of 800 – 2000 cm^{-1} is suitable for the measurement of first order D and G peaks of carbon. After the appropriate measurement range is set it

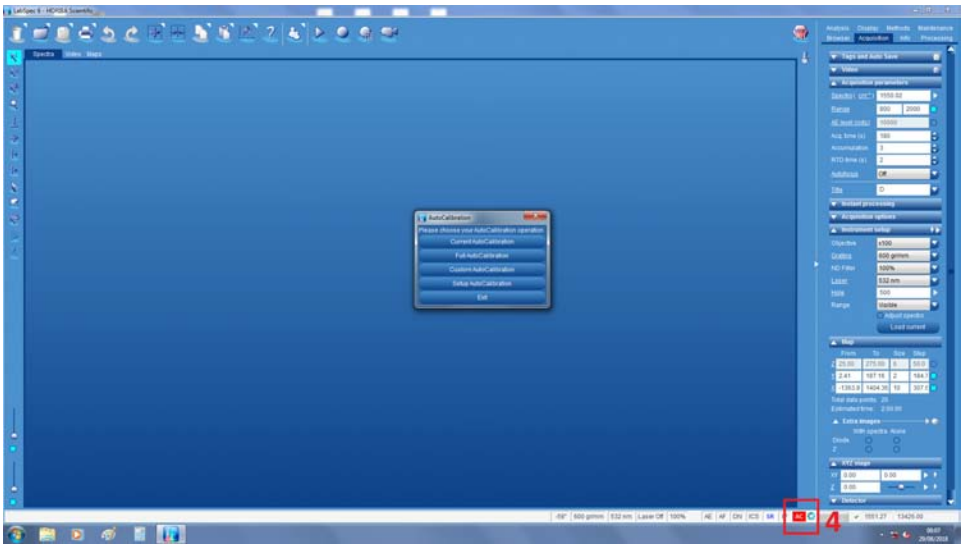

Figure 8.5: LabSpec6 — autocalibration

is advisable to use the real time display (RTD) highlighted by no 6. This makes short repeated measurements that are continually refreshed on the screen. These short measurements make it possible to judge the time needed for the full measurement (note that the maximum detector count is cca. 64 000). This can then be started by the Start measurement button (no. 7). If some damage to the sample after the measurement is observed, the time of the measurement needs to be shortened and/or an neutral-density (ND) filter needs to be applied.

The data analysis of different samples greatly varies and reaches form comparison of the measured spectra with a database to identify the peaks and therefore to identify the sample material to fitting of the peaks an calculation of different material parameters like evaluation of the bonding hybridization of carbon.

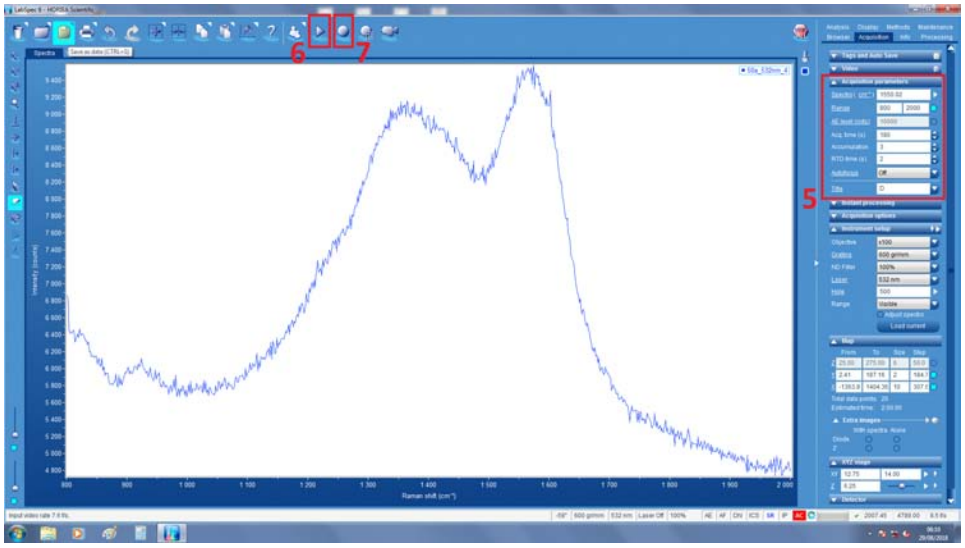

Figure 8.6: LabSpec6 — measurement

Chapter 9

Surface Energy Analysis

doc. RNDr. Vilma Buršíková, Ph.D.

The determination of surface free energy of a solid is of a great importance in a wide range of problems in applied science. Because of the difficulties to measure directly the surface free energy of a solid phase, indirect approaches have been used. Among the indirect methods used for estimation of the surface free energy of the solids, the contact angle measurements are believed to be the simplest.

The contact angle measurement could be easily performed by establishing the tangent angle of a liquid drop with a solid surface. The contact angle of a liquid drop on a solid surface is defined by the mechanical equilibrium of the drop under the action of three interfacial tensions solid/vapour, solid/liquid and liquid/vapour. The surface free energy of plasma treated polymers can be easily examined by using contact angle measurement. The method is suitable for surface characterization of various materials i.e. polymers with or without adhesive treatment, protective coatings, materials with biocompatible modification, natural materials (paper, textiles) etc. Thanks to wide range of possible use becomes this method useful in chemical and plasmachemical laboratories, in packaging techniques, chemical, automotive industry etc.

The determination of the surface free energy of solids from contact angles relies on a relation, which has been proposed by Young in 1805 [86] and the equilibrium relation is known as Young`s equation. In the literature there is wide range of different methods for surface free energy calculation which are based on the Young`s relation [86]. There are various graphical or numerical methods (Zisman Theory, Fowkes Theory, The Extended Fowkes Theory, Wu Equation of State, Owens - Wendt - Raeble - Kaeble Theory, Lifshitz & van der Waals - Lewis Acid - Base Theory etc.). One of the most often used methods is the Owens-Wendt-Rable-Kaeble (OWRK) method [85].

9.1 Surface Tension and Surface Free Energy

In case of liquid surfaces the term 'surface tension' and the term 'surface free energy' are often interchanged. The term surface tension arose from historical concept that the liquid has a 'skin' which can exert a force per unit length. Generally, the surface tension γ can be defined as the reversible work, W done in creating a unit surface area

$$W = \gamma \Delta A. \tag{9.1}$$

Here ΔA is the newly created surface area. γ may be associated with units of either Jm^{-2} (surface free energy) or Nm^{-1} (surface tension). These two units are dimensionally equivalent.

The total Helmholtz free energy F_{tot} of the system may be written in the following form

$$F_{tot} = NF_a + AF_{surf}. \tag{9.2}$$

Here F_a is the Helmholtz free energy per atom, N is the number of atoms of the bulk material and F_{surf} is the Helmholtz free energy per unit area of the surface:

$$\mathrm{d}F_{tot} = -S\mathrm{d}T - P\mathrm{d}V + \mu \mathrm{d}N + F_{surf}\mathrm{d}A \rightarrow \mathrm{d}F_{tot(T,V,N)} = F_{surf}\mathrm{d}A. \tag{9.3}$$

Here S is the entropy, P is the pressure and μ is the chemical potential. The reversible work done in creating of unit area of surface is the Helmholtz free energy for that area at constant temperature T and volume V

$$\gamma = \left(\frac{\mathrm{d}Ftot}{\mathrm{d}A}\right)_{T,V,N} \tag{9.4}$$

From 9.3 and 9.4 follows:

$$\gamma = F_{surf}. \tag{9.5}$$

The surface tension equals the Helmoltz free energy for the surface, which is generally termed the surface free energy.

In case of solid surfaces the interatomic/intermolecular forces are stronger than in case of liquids, therefore the solid material is not able to rearrange itself in order to minimise its energy. This results in another contribution to the surface free energy, which is the contribution of the surface stress, resulting from the work required to deform the surface. The relationship between the surface tension, surface stress and surface free energy is too complex to deal with here in detail [85].

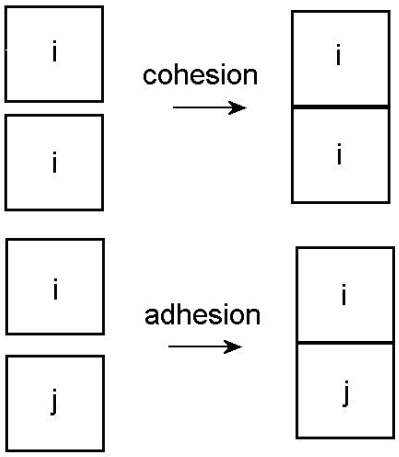

Figure 9.1: Schema of adhesion and cohesion [85].

The surface free energy of solids can be described as a measure of disruption of chemical bonds that occurs when a new surface is created. Surfaces must be energetically less favourable than the bulk of the material otherwise there would be a driving force for creation of new surfaces. Cutting a piece of a solid material in half (see Fig 9.1) breaking its bonds consumes energy. If the cutting is done reversibly, then the energy W consumed by the cutting process is equal to the energy of the two newly created surfaces $2\gamma_i$. The unit surface energy would be therefore half of the cohesion energy (see Fig 9.1) of the solid material.

$$\frac{W_c}{2} = \gamma_i \tag{9.6}$$

In practice it is true only for surfaces newly prepared in ultra-high vacuum conditions. All surfaces are energetically unfavourable in that they have a positive energy of formation. Due to positive energy of newly created surface there are driving forces leading to creation of surface layers of natural oxides or contaminations. Therefore clean surfaces in ultra-high vacuum conditions have higher free energy, than oxidised or contamined surfaces. Energy of adhesive bonds W_a is energy released at creation of adhesive bonding between two different materials i and j. The energy of adhesion can be also defined as the energy which is needed for the separation of two different materials i and j.

Wa may be determined according to Dupré´ formula:

$$W_i + W_j = W_{ij} + W_a, \tag{9.7}$$

where W_i is the cohesion energy of the substance i, W_j is the cohesion energy of the substance j and W_{ij} is the energy of the solid-solid or solid-liquid interface. Direct measurements of surface free energy of solid surface

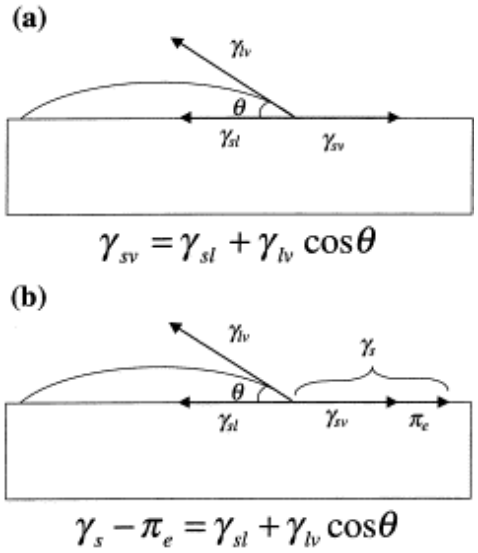

Figure 9.2: Contact angle of a sessile drop (a) neglecting the spreading pressure (b) accounting for spreading pressure. [101].

W_j and of the interfacial energy W_{ij} are rather difficult, so the equation in the above described form could not be used easily for determination of energy of adhesion W_a.

9.2 Young´s Equation

If a drop of a liquid l is brought into contact with a flat horizontal solid surface s in a gas atmosphere v, it can either spread over the surface or assume the shape of a spherical segment from a flat lens up to an almost complete ball. The most well known description of wetting state was derived by Young in 1805. The Young´s equation describes the equilibrium of forces between the surface tension at the three-phase boundary:

$$\gamma_{sl} - \gamma_{sv} = \gamma_{lv} \cos\Theta, \tag{9.8}$$

where γ_{sv} is the solid-vapor interfacial free energy, γ_{sl} is the solid-liquid interfacial free energy, and γ_{lv} is the liquid-vapor interfacial tension.

In Fig 9.2 a the wetting state by Young is illustrated: γ_{sv} is the solid-vapor interfacial free energy, γ_{sl} is the solid-liquid interfacial free energy, and γ_{lv} is the liquid-vapor interfacial tension. In Fig 9.2 b the wetting state accounting for spreading pressure π_e is illustrated.

If the contact angle is equal to 0^o then the liquid will completely spread over

the surface of the solid phase. If the contact angle is equal to 180^o, liquid will not wet the solid surface. Generally, the solid surface is called wettable if the contact angle of the liquid drop is less than 90^o and is not wettable if the contact angle is higher than 90^o. The solid surfaces may be divided into two groups, they may be hydrophilic (wettable with water) or hydrophobic (not wettable with water). The first case concerns the high-energy surfaces and the second case concerns the low-energy surfaces. High-energy surfaces such as metal, oxide or ceramic surfaces should be completely wetted by fluids. However, the complete wetting ($\Theta = 0^o$) may be obtained only in the case of completely clean, highly polished surfaces and pure liquids in inert gas atmospheres that are completely free of contaminants. Even a short-time contact with a gas atmosphere of less than 1% relative atmospheric humidity substantially changes the surface properties of the high-energetic materials [85].

On the basis of γ_{sv}, γ_{sl} and γ_{lv} the following thermodynamic quantities may be defined:

Work of adhesion

$$W_a = \gamma_{sv} + \gamma_{lv} - \gamma_{sl} = \gamma_{lv}(\cos\Theta + 1) \tag{9.9}$$

Spreading coefficient

$$\pi_e = \gamma_{sv} - \gamma_{lv} - \gamma_{sl} = \gamma_{lv}(\cos\Theta - 1) \tag{9.10}$$

Wetting energy

$$W_e = \gamma_{sv} - \gamma_{sl} = \gamma_{lv}\cos\Theta \tag{9.11}$$

9.3 Models for determination of interfacial tension

According to Duprè (see Eq. 9.9) [86] the interfacial tension between two phases i and j may be expressed as

$$\gamma_{ij} = \gamma_i + \gamma_j - W_{ij} \tag{9.12}$$

Antonow [93] estimated the interfacial tension as a difference between the surface tensions of the individual phases i and j:

$$\gamma_{ij} = |\gamma_i - \gamma_j| \tag{9.13}$$

This approach was found to be not sufficiently accurate.

Good and Girifalco [98] used the Berthelot`s [91] rule to calculate the interfacial tension. Berthelot suggested, that the free energy of adhesion (ΔG^a_{ij}) is equal to the geometric mean of free energies of cohesion of the separate phases i and j (ΔG^c_i and ΔG^c_j). According to this rule, the following relationship applies to apolar substances:

$$\Delta G^a_{ij} = \sqrt{\Delta G^c_i . \Delta G^c_j} \rightarrow \frac{\Delta G^a_{ij}}{\sqrt{\Delta G^c_i . \Delta G^c_j}} = 1. \tag{9.14}$$

In case of polar phases, the experimental results are often in conflict with Eq. 9.14. In order to correct these discrepancies the interaction parameter Φ was defined in the following way:

$$\Phi = \frac{\Delta G^a_{ij}}{\sqrt{\Delta G^c_i . \Delta G^c_j}}. \tag{9.15}$$

The free energy of adhesion is the negative work of the adhesion and the free energy of cohesion is the negative work of cohesion:

$$\Delta G^a_{ij} = -W^a_{ij},\ \Delta G^c_i = -W^c_i,\ \Delta G^c_j = -W^c_j. \tag{9.16}$$

Using the Duprè`s relationship Eq. 9.7, Eq. 9.6, Eq.9.15 and the geometric combining rule, the following equation will be obtained:

$$\Delta G^a_{ij} = -W^a_{ij} = -2\Phi\sqrt{\gamma_i . \gamma_j}. \tag{9.17}$$

From Young`s equation 9.8 it is possible to obtain the relationship between the equilibrium contact angle and the interaction parameter:

$$\gamma_{ij} = \gamma_i + \gamma_j - 2\Phi\sqrt{\gamma_i . \gamma_j} \tag{9.18}$$

From the above relations follows:

$$\cos\Theta \cong -1 + 2\Phi\sqrt{\frac{\gamma_i}{\gamma_j}} \tag{9.19}$$

The interaction parametr Φ depends on the mutual properties of the liquid and the solid surface:

$\Phi = 1$ for so called regularinterfaces, i.e. systems for which the cohesive forces of the two phases and the adhesive forces across the interface are of the same type.

$\Phi < 1$ the dominant forces within the separate phases are unlike, e.g. London - van der Waals vs. metallic or ionic or dipolar.

$\Phi > 1$ there are specific interactions between the molecules forming the two phases.

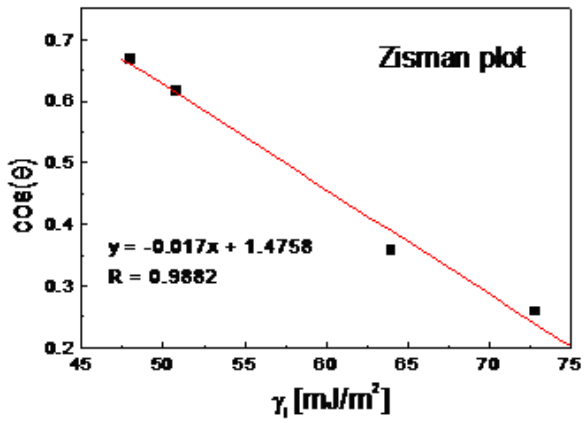

Figure 9.3: Example of the use of Zisman model (there were used four liquids: water, glycerol, ethylene glycol a methylene iodide). The value of the calculated critical surface free energy for amorphous diamond-like carbon was $\gamma_c = 27.9\ \frac{mJ}{m^2}$ [85].

9.4 Surface Free Energy Evaluation

9.4.1 Zisman plot

Zisman [87] noticed that a plot of $\cos\Theta$ versus γ_l is often linear [1, 2, 3]. The Zisman method is based on the determination of the dependence of the $\cos\Theta$ on the total liquid tension

$$\cos\Theta = f(\gamma_l) \tag{9.20}$$

With linear extrapolation (for $\cos\Theta \to 1$) we can obtain the critical surface energy γ_c. The dependence could be fitted by the following equation:

$$\cos\Theta = 1 + b(\gamma_c - \gamma_l), \tag{9.21}$$

where b is a constant characteristic for the set of liquids used. Te value γ_c characterises the type of molecules on the surface.

The relative inertness of surfaces can be evaluated by comparing the value of γ_c of the surface. The theory becomes complex if nonpolar liquids are used. However, the plot of $\cos\Theta$ versus γ_l is not exactly linear. Neglect of spreading pressure π_e for $\Theta < 10^o$ and the assumption that $\Phi = 1$ are not always valid. Surface energy varies widely with the functional groups at the surface. For hydrophobic surfaces, free energy decreases in the order $-CH_2 > -CH_3 > -CF_2- > -CF_2H > -CF_3$. In table there are listed

Group	$\gamma_c[mJ.m^{-2}]$
$-CF_3$	6
$-CF_2-$	18
$-CH_3$	22
$-CH_2-$	31-33

Table 9.1: Characteristic values of critical surface energy for several functional groups [85].

the critical surface energy values for several highly hydrophobic functional groups [85].

According to Girifalco and Good [98] (Eq. 9.19) $\cos\Theta \cong -1 + 2\Phi\sqrt{\frac{\gamma_{sv}}{\gamma_{lv}}}$ the dependence of $\cos\Theta$ on $\sqrt{\frac{1}{\gamma_{lv}}}$ has to be linear. This suggests that if we plot $\cos\Theta$ against $\sqrt{\frac{1}{\gamma_{lv}}}$. The intercept should be - 1 and the slope should be equal to $2\Phi\sqrt{\gamma_{sv}}$.

9.4.2 Equation of State

One of the groups of models for surface free energy calculation is based on the thermodynamic equation of states expressed in the form $\gamma_{sl} = f(\gamma_{lv}, \gamma_{sv})$, where γ_{sl} depends only on γ_{lv} and γ_{sv}.

Ward and Neumann [90] proposed for low energetic surfaces the following equation

$$\gamma_{sl} = \frac{\sqrt{(\gamma_{sv}} - \sqrt{\gamma_{lv})^2}}{(1 - 0.015\sqrt{\gamma_{sv}\gamma_{lv}}}. \tag{9.22}$$

Combining this equation with Young`s formula one cane obtain:

$$\cos\Theta = \frac{(0.015\gamma_{sv} - 2)\sqrt{\gamma_{sv} + \gamma_{lv}} + \gamma_{lv}}{\gamma_{lv}(0.015\sqrt{\gamma_{sv}\gamma_{lv}} - 1)}. \tag{9.23}$$

The equation gives from known contact angle $\cos\Theta$ the value of γ_{sv}. The equation derived by Li a Neumann [99] was determined empirically by using a large number of contact angle data:

$$\gamma_{sl} = \gamma_{sv} + \gamma_{lv} - 2\sqrt{\gamma_{sv}\gamma_{lv}}e^{-0.0001247(\gamma_{lv}-\gamma_{sv})^2}. \tag{9.24}$$

Combining Eq. 9.24 with Young`s equation yields

$$\cos\Theta = -1 + 2\sqrt{\frac{\gamma_{sv}}{\gamma_{lv}}}e^{-0.0001247(\gamma_{lv}-\gamma_{sv})^2}. \tag{9.25}$$

Kwok and Neuman proposed the following form of equation of states

$$\gamma_{sl} = \gamma_{sv} + \gamma_{lv} - 2\sqrt{\gamma_{sv}\gamma_{lv}}(1 - 0.0001057(\gamma_{lv} - \gamma_{sv})^2), \tag{9.26}$$

what in combination with Young`s equation gives

$$\cos\Theta = -1 + 2\sqrt{\frac{\gamma_{sv}}{\gamma_{lv}}}(1 - 0.0001057(\gamma_{lv} - \gamma_{sv})^2). \tag{9.27}$$

Wu suggested for equation of state the following expression

$$\gamma_c = \frac{\gamma_l(1 + \cos\Theta)^2}{4}. \tag{9.28}$$

. where γ_c is function of interaction parameter and of the surface free energy. Wu obtained from the dependence $\gamma_c = f(\gamma_l)$ the maximum value of γ_c as γ_s.

9.4.3 Fowkes Theory

Theory of Fowkes [88,89,95] forms a basis of all the surface free energy component evaluations used today and the dispersion component of the total surface energy is still calculated by using this approach. Fowkes considered the surface free energy to be a measure of the attractive force between surface layer and liquid phase and that these attractive forces and their contribution to the free energy are additive. The intermolecular attractions, which cause surface tension, arise from a variety of well-known intermolecular forces. Most of these forces, such as metallic bonding and hydrogen bonding, are a function of specific chemical nature. However, London dispersion forces exist in all types of matters and always give an attractive force between adjacent atoms or molecules, no matter how dissimilar their nature may be. The London dispersion forces arise from the interaction of fluctuating electronic dipoles with the induced dipoles in neighbouring atoms or molecules. The effect of fluctuating dipoles cancels out, but not that of the induced dipoles. These dispersion forces contribute to the cohesion in all substances and are independent of other intermolecular forces, but their magnitude depends on the type of material and density. Therefore, the γ^d term includes only the London dispersion force contribution and Keesom and Debye force contributions are included in the γ^p term. If only dispersion forces are considered, than

$$\gamma_{sl} = \gamma_s + \gamma_l - 2\sqrt{\gamma_s^d\gamma_l^d} \tag{9.29}$$

From Young-Duprè equation it is possible to obtain the work of adhesion W_A

$$W_A = \gamma_l(1 + \cos\Theta) = 2\sqrt{\gamma_s^d \gamma_l^d} \tag{9.30}$$

If there are additional interactions Esl at the interface, the equation should be written as:

$$W_A = \gamma_l(1 + \cos\Theta) = W_A^d + E_{sl} \rightarrow W_A^d = 2\sqrt{\gamma_s^d \gamma_l^d} \tag{9.31}$$

The work of adhesion was considered to be made up of independent additive terms:

$$W_A = W_A^d + W_A^p + W_A^h + W_A^i + W_A^{ab} + ... \tag{9.32}$$

Therefore the surface free energy was similarly considered to made up from independent additive terms:

$$\gamma = \gamma^d + \gamma^p + \gamma^h + \gamma^i + \gamma^{ab} + ... \tag{9.33}$$

suffix d marks dispersion (London) interactions, suffix p means Keesom`s interactions, h means hydrogen bonds, i means inductions (Debye) interactions and ab means acid-base interactions.

Owens, Wendt, Rabel and Kaelble (OWRK) Theory

Owens, Wendt, Rabel and Kaelble [94] proposed the division of the total surface energy of a solid or liquid in two components: dispersion force component γ^d and polar component γ^p. The interaction energy of the non -dispersive forces at the interface was quantified and included as geometric mean of the non-dispersive components of solid and liquid. The equation proposed was the extension of the equation proposed by Fowkes:

$$\gamma_{sl} = \gamma_s + \gamma_l - 2(\sqrt{\gamma_s^d \gamma_l^d} + \sqrt{\gamma_s^p \gamma_l^p}) \tag{9.34}$$

Combining this equation with Duprè`s formula the following term was obtained

$$W_A = \gamma_l(1 + \cos\Theta) = 2(\sqrt{\gamma_s^d \gamma_l^d} + \sqrt{\gamma_s^p \gamma_l^p}) \tag{9.35}$$

Dalal [97] developed a method for the best-fit solution of simultaneous equations, which are obtained when more than two testing liquids are used. Least squares method is used to solve the over-determined systems of equations in the following form:

$$\frac{(1 + \cos\Theta)}{2} \frac{\gamma_l}{\sqrt{\gamma_l^d}} = 2\sqrt{\gamma_s^d} + \sqrt{\gamma_s^p}\sqrt{\frac{\gamma_l^p}{\gamma_l^d}} \tag{9.36}$$

The Extended Fowkes method

In case of the Extended Fowkes method the total surface free energy of the studied solid is divided in three components: dispersion γ^d, polar γ^p and γ^H components. The γ^H component results from hydrogen bridges. The interaction energy of the non - dispersive forces at the interface was quantified and included as geometric mean of the non-dispersive components and hydrogen bridge components of solid and liquid:

$$\gamma_{sl} = \gamma_s + \gamma_l - 2(\sqrt{\gamma_s^d \gamma_l^d} + \sqrt{\gamma_s^p \gamma_l^p} + \sqrt{\gamma_s^h \gamma_l^h}) \tag{9.37}$$

Combining this equation with Duprè`s formula the following term was obtained

$$\gamma_l(1 + \cos\Theta) = 2(\sqrt{\gamma_s^d \gamma_l^d} + \sqrt{\gamma_s^p \gamma_l^p} + \sqrt{\gamma_s^h \gamma_l^h}) \tag{9.38}$$

The most appropriate solution is to do first the measurement of the dispersion part using a non-polar liquid. In the second step it is recommended to measure the polar part with liquid which exhibits a hydrogen bridge part equal to zero $\gamma_l^h = 0$. Finally the hydrogen bridge component of the surface free energy of the solid can be determined using a liquid which exhibits nonzero hydrogen bridge component of surface tension.

Wu Theory (Harmonic Mean)

On the basis of the method of Wu [96] the surface free energy of the solid is given as the sum of the disperse γ^d and polar γ^p components of the surface free energy. The interfacial energy between the solid surface and the liquid γ_{sl} could be detemined according to following formulaes.

$$\gamma_{sl} = \gamma_s + \gamma_l - 4\left(\frac{\gamma_s^d \gamma_l^d}{\gamma_s^d + \gamma_l^d} + \frac{\gamma_s^p \gamma_l^p}{\gamma_s^p + \gamma_l^p}\right) \tag{9.39}$$

Combination of the formulae Eq. 9.39 with equation of Duprè and Young-Duprè gives the final formulae for the calculation of the surface free energy components

$$W_A = \gamma_{li}(1 + \cos\Theta_i) = 4\left(\frac{\gamma_s^d \gamma_{li}^d}{\gamma_s^d + \gamma_{li}^d} + \frac{\gamma_s^p \gamma_{li}^p}{\gamma_s^p + \gamma_{li}^p}\right) \tag{9.40}$$

Suffix li refers to measurements using several different liquids. This equation is useful for systems with high energy (i.e. glasses, oxides, graphite, metals etc.) [12-17].

Combination of the harmonic mean and geometric mean gives:

$$\gamma_{li}(1+\cos\Theta_i) = 2\sqrt{\gamma_s^d\gamma_{li}^d} + 4\frac{\gamma_s^p\gamma_{li}^p}{\gamma_s^p+\gamma_{li}^p} \tag{9.41}$$

or

$$\gamma_{li}(1+\cos\Theta_i) = 2\sqrt{\gamma_s^p\gamma_{li}^p} + 4\frac{\gamma_s^d\gamma_{li}^d}{\gamma_s^d+\gamma_{li}^d} \tag{9.42}$$

Dalal [97] performed a comparative study of the two approaches, geometric mean and harmonic mean, on 12 common polymers using the published data with six liquids. It is found that the total surface energy of the solid obtained by the two methods are generally quite close.

Combination of two liquids with similar values of polar and dispersion components gives wrong values of the surface free energy. Value D for two liquids i and j used for the calculation should be higher than 10 mJm^{-2}:

$$D = \sqrt{\gamma_{li}^d\gamma_{lj}^p} - \sqrt{\gamma_{lj}^d\gamma_{li}^p} \tag{9.43}$$

Acid-Base Theory

The Lifshitz & van der Waals - acid-base approach was proposed by van Oss, Good and Chaudhury [86]. This method enables to determine the electron - acceptor and electron - donor parameters of the surface free energy. The total surface free energy is a sum of its Lifshitz & Van der Waals (LW) and acid/base (AB) components:

$$\gamma_{TOT} = \gamma^{LW} + \gamma^{AB}, \tag{9.44}$$

where LW indicates the total Lifshitz-Van der Walls interactions and AB refers to the acid-base or electron-acceptor and electron-donor interaction according to Lewis. The surface energy can be calculated according to Young-Duprè equation expressed by LW component, acid component γ^+ (acceptor effect) and basic component γ^- (donor effect):

$$(1+\cos\Theta)\gamma_l = 2(\sqrt{\gamma_{li}^{LW}\gamma_s^{LW}} + \sqrt{\gamma_{li}^+\gamma_s^-} + \sqrt{\gamma_{li}^-\gamma_s^+}), \tag{9.45}$$

where li refers to liquid and s refers to solid material. The values can be determined from contact angle measurement with three liquids of which two must have polar component. The polar component is given by

$$\gamma^{AB} = 2\sqrt{\gamma^+ + \gamma^-}. \tag{9.46}$$

The equations of the form of Eq. 9.45 may be written in matrix form $\mathbf{Ax} = \mathbf{B}$ with the contact angle data of various liquids on solid. The system can

be over - determined with more than three liquid contact angles and the least square method may be used to determine the coefficients in equation Eq. 9.47.

$$\frac{(1+\cos\Theta_{li})}{2}\frac{\gamma_{li}}{\sqrt{\gamma_{li}^{LW}}} = \sqrt{\gamma_s^{LW}} + \sqrt{\gamma_s^+}\sqrt{\frac{\gamma_{li}^-}{\gamma_{li}^{LW}}} + \sqrt{\gamma_s^-}\sqrt{\frac{\gamma_{li}^+}{\gamma_{li}^{LW}}} \tag{9.47}$$

In comparison with the three-liquid method the regression method is much more stable against the wrong selection of the testing liquids. The result of the regression method is usually very close to the product of the three-liquid method on the recommended liquid combinations [85].

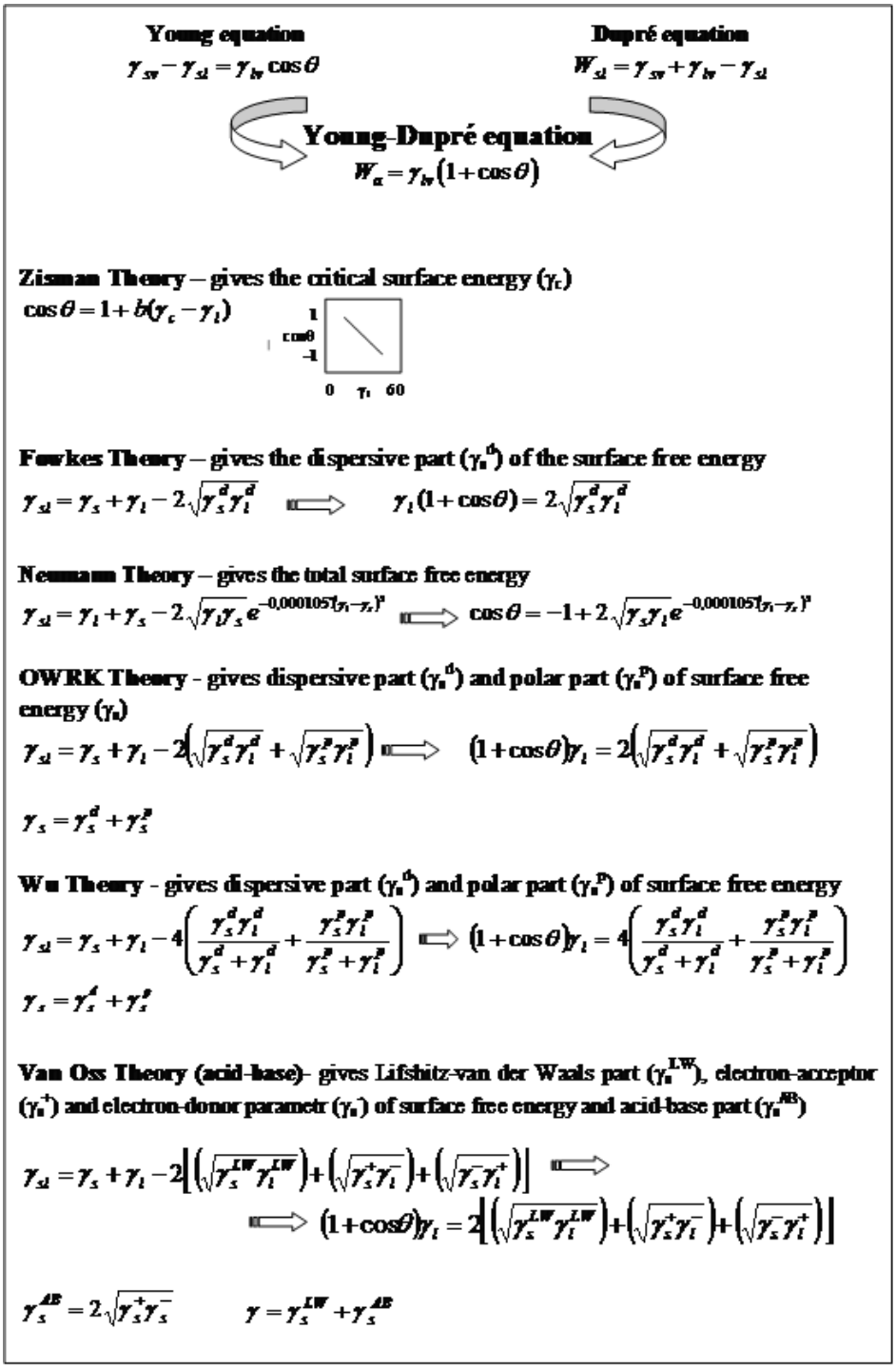

Figure 9.4: Overview on most often used methods of surface free energy evaluation [85].

Chapter 10

Instrumented indentation techniques

Mgr. Lukáš Zábranský, Ph.D.

10.1 Introduction

Indentation test is a simple method consisting of pressing of a well-defined material whose mechanical properties and geometry are known (indenter) into a measured material whose mechanical properties are unknown (measured specimen, e.g. a thin film). It is one of the most convenient ways how to measure mechanical properties such as hardness or Young's modulus in absolute terms. It is considered as nondestructive, the analysis procedure is well standardized, and the method can be used for wide variety of materials with different mechanical properties such as glass, metals, ceramics, etc. The established widely known Vickers, Brinell, Knoop and Rockwell tests are based on pressing of an indenter with a certain shape (which is different in case of each method) into a material. Afterwards, the projected (contact) area of a residual crater (indent), which is a result of the indentation process, is measured by an optical microscope and the mechanical properties are calculated from the known applied load and the size of the projected area. This procedure is time consuming and the determination of the projected area is subjective. However, the main disadvantage is when the measurement scale of displacement is in nanometers (10^{-9} m) instead of millimeters or micrometers (10^{-6} m), which are typical measurement scales in indentation or microindentation tests. In the nanometer range, in which we most definitely are if we want to measure mechanical properties of thin films, we are talking about *nanoindentation*. The size of residual imprints is so small that it is very complicated to even find them under an optical microscope. Thus, other methods of determination of the contact area needed for further analysis must be sought for.

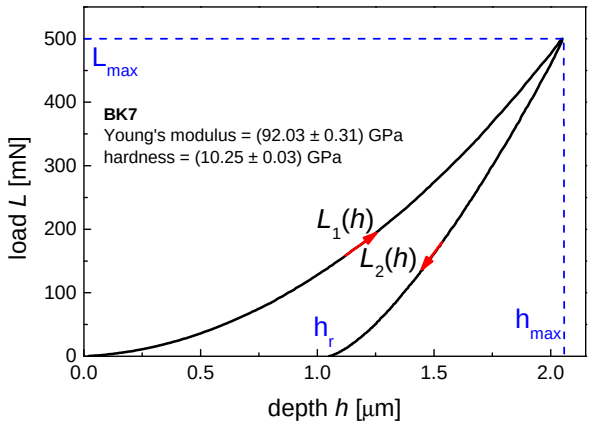

Figure 10.1: Load-displacement curve measured on BK7 standard.

It is possible to measure this using atomic force microscopy (AFM); however, this is also time-consuming and demands a precise knowledge of the location of residual imprints on a specimen surface. The other possibility is to use the so-called *Instrumented Indentation Technique* (IIT), also known in literature as *Depth Sensing Indentation* (DSI) which is a smart and fast method where the contact area is calculated from the known geometry of the indenter and actual penetration depth of the indenter into the specimen. In the case of this method, the instantaneous depth of an imprint is detected during the entire loading and unloading processes, depending on the instantaneous load value. Fully automated recording of the test progress allows fast processing of measured dependencies. By analyzing the loading and unloading curves (so-called *load-displacement curve*) obtained from the test, the hardness, modulus of elasticity, fracture toughness, resistance to indentation creep, thin film adhesion to the substrate and other useful characteristics can be determined.

10.2 Load-displacement curve

In a typical nanoindentation test, load L and depth of penetration h are recorded as load is applied from zero to some maximum $\mathrm{L_{max}}$ and then from the maximum load back to zero. The *load-displacement curve L(h)* is a result of a recording of one nanoindentation measurement. This curve has two main parts (see Fig. 10.1): first, there is a part of the gradual increase of the load or the *loading part* $L_1(h)$ which is followed by a second part of gradual decrease of the load or the *unloading part* $L_2(h)$.

For the case of pure elastic reversible deformation, the loading and unloading

parts overlap perfectly. If plastic deformation occurs during the test, then the unloading curve will follow a different path compared to the loading curve and there is a residual impression of depth h_r left on the surface of the specimen. From the plastically deformed volume, or more precisely, the area of the residual impression and the known applied load it is possible to calculate the *hardness* H of the specimen. The methods of analysis rely on the assumption of an elastic-plastic loading followed by an elastic unloading, with no reverse plasticity during the unloading sequence. There is only some degree of recovery due to the relaxation of elastic strains within the material which occurs mostly in the later part of the unloading curve. The beginning is considered approximately linear; therefore, the initial portion of the elastic unloading response is used for calculation of the *reduced elastic modulus* E_r of the indented specimen.

10.3 Analysis of load-displacement curve

The results of the analysis can largely depend on the model used to evaluate the load/depth dependencies. The use of an analysis based on the elastic contact model assumes that the following conditions are met:

1. no reverse plasticity occurs during the unloading part of the test;
2. for calculation of the so-called reduced elastic modulus Er, the Sneddon's equation [102, 103] can be used; here the compliances of the indenter and the sample are summed according to the relationship describing elasticity of springs connected in series:

$$\frac{1}{E_r} = \frac{1-\mu_i^2}{E_i} + \frac{1-\mu_s^2}{E_s}, \tag{10.1}$$

   where E is the Young's modulus, μ is the Poisson's ratio and indices i and s denote indenter and sample material;
3. the indenter has a precisely defined shape and the test surface is perfectly smooth;
4. the contact can be modelled using an analytical model [104,105] for the contact between a rigid indenter of a defined shape and an elastically homogeneous isotropic half-space:

$$\frac{\mathrm{d}L}{\mathrm{d}h} = \frac{2}{\pi} E_r \sqrt{A_p}, \tag{10.2}$$

   where A_p is so-called projected contact area of an indenter contacting the surface of measured specimen.

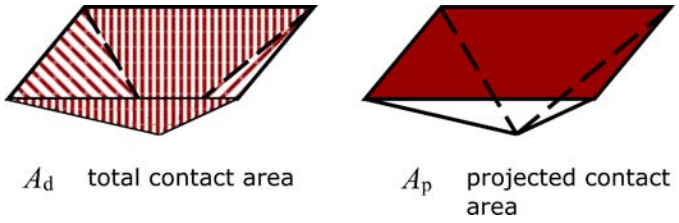

Figure 10.2: Comparison of total and projected contact areas.

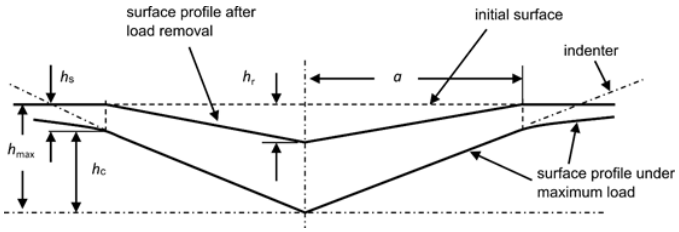

Figure 10.3: Schematic of indentation process with important characteristics: a is diameter of the indenter, h_{max} is maximum depth at maximum load, h_r denotes for residual depth, h_c is contact depth and h_s is depth of sink-in.

In Fig. 10.2 the difference between total contact area A_d and contact area projected into the surface plain (projected contact area A_p or an area as it is seen and measured under an optical microscope) is explained.

The side view of a specimen surface in contact with an indenter and after unloading is depicted in Fig. 10.3. It is clear that while the load is at the maximum L_{max} and the depth is at h_{max}, the true *contact depth* h_c, i.e. the depth of contact between the indenter and surface of the specimen, is lower than h_{max} and higher than h_r (the influence of pile-up is not accounted here).

After unloading, the residual indentation imprint partially recovers in the depth direction; however, its radius a remains mostly unchanged. This is an important conclusion because it means that right from the h_c it is easy to calculate the diameter a and if the geometry of the indenter is known, it is possible to calculate from parameter a the projected contact area A_p. The main task of IIT analysis is to substitute the direct measurement of the projected contact area of residual imprint which is here reduced to the task of finding the contact depth. Both h_{max} and h_r can be extracted explicitly from the load-displacement curve without the need of any assumptions; however, for determination of contact depth h_c we need to have a model assuming the geometry of the indenter. The contact area is generally a function of contact depth depending on the geometry of the indenter [105]:

$$A_p(h_c) \sim h_c^m \tag{10.3}$$

The cylindrical indenter has an index m = 0 and the contact area is constant with depth, the spherical tip has m = 1 and the cone or pyramid has m = 2. For the spherical indenter, the contact depth is exactly half of the actual depth during loading, for cylinder it is lower and for pyramid or cone it is slightly higher. According to Oliver and Pharr [105,106], this behaviour can be summarized into an equation where the h_c is fully expressed in measurable quantities:

$$h_c = h_{max} - h_s = h_{max} - \epsilon \frac{L_{max}}{S}; h_s = \epsilon(h_{max} - h_p), \tag{10.4}$$

where h_s is a depth of sink in, h_p is the intersection of tangent of the unloading curve at maximum load and the depth axis, ϵ is a constant depending on indenter geometry (0.72 for cone tip and 0.75 for spherical indenter) and S is *contact stiffness* calculated from the power law fit of the initial part of the unloading curve with m as a fitting parameter:

$$S = \frac{\mathrm{d}L}{\mathrm{d}h}(h_{max}) = mA_p(h_{max} - h_p)^{m-1}. \tag{10.5}$$

An example of analysis by the Oliver and Pharr method is depicted in Fig. 10.4 with important characteristics highlighted. Another way how to estimate the contact depth, described by Doerner and Nix [107] in 1986, is to use the intercept of the tangent to upper part of the unloading curve and the depth axis h_p. This older method provides reasonable values of calculated contact area for materials with relatively high E/H ratio (elastic modulus E to hardness H), e.g. metals; however, for materials with low value of E/H, where significant elastic recovery occurs, the whole of the unloading curve is not linear and the power law fit and the method according to Oliver and Pharr should be used instead.

For perfectly sharp Berkovich (three-sided pyramid) or Vickers (four-sided pyramid) indenters, commonly used to study mechanical properties of thin films, the relationship describing their geometry is:

$$A_p = 24.5h_c^2. \tag{10.6}$$

However, it is impossible to manufacture such precise shape of an indenter; therefore, corrections of the indenter shape need to be done during calibration on a specimen whose mechanical properties are known. This is especially important for measurements with low depths which is the case for most measurements on thin films. The function of $A_p(h_c)$ after corrections is:

$$A_p(h_c) = 24.5h_c^2 + \sum_{j=1}^{7} c_j \sqrt[2^j]{h_c}, \tag{10.7}$$

where c_j is a calibration constant for a specific indenter geometry.

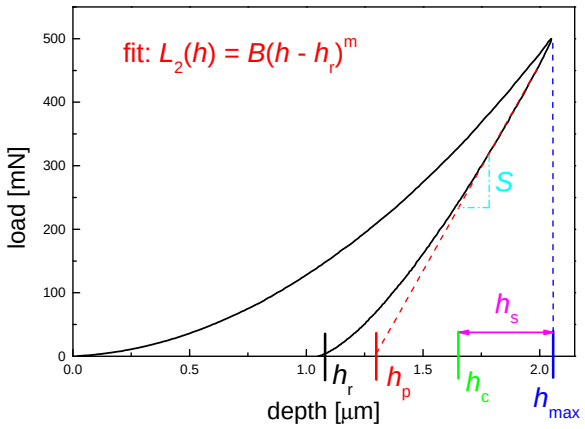

Figure 10.4: The example of analysis of load-displacement curve according to Oliver and Pharr method with important parameters: h_s is depth of sink in, h_c is contact depth, h_p is the intercept of tangent to the unloading curve and depth axis, S is contact stiffness, h_{max} is maximum depth, h_r is residual depth and B and m are fitting constants.

10.4 Elastic-plastic contact

Indentation tests on many materials result in elastic-plastic deformation of the specimen material which cannot be considered as superposition of elastic and plastic properties obtained from models of ideal plastic and ideal elastic solid. It turns out, for example, that the stress field generated by the elastic-plastic deformation when using the pyramidal indenter is similar to the stress field generated from the spherical indenter with no plastic deformation in the specimen. For the pyramidal indenter, the mean contact pressure p_m is constant during the loading phase. However, this does not apply to the unloading phase if the plastic deformation occurs. In the plastically deformed volume, the hydrostatic pressure is generated which decreases during the unloading phase. In brittle materials, plastic deformation most commonly occurs with pointed indenters; in ductile materials, plasticity may be readily induced with blunter indenters such as a sphere or cylindrical punch.

The model for ideal elastic-plastic behaviour of a material was created by Tabor [108,109]. According to his research, the ideal elastic-plastic material has a linear curve of stress-strain dependence. This dependency is constant until the elastic limit (yield strength) is reached. Then it starts to behave plastically under the stress of the yield strength Y, which remains constant even when we consider the presence of permanent plastic deformation. The relationship between Y and the maximum strain load L_{max} can be found.

This direct relationship depends on the material. In general, three areas of material behaviour can be distinguished by the mean pressure value p_m compared to Y [104]:

1. $p_m < 1.1\,Y$ — fully elastic recovery occurs without the presence of plastic deformation;

2. $1.1\,Y < p_m < \mathrm{C}\,Y$ — plastic deformation exists under the surface, but is limited by surrounding elastically deformed material. The C value is the so-called *constraint factor*. This is dependent on the material and tip geometry. In addition, the C value changes during the formation of the plastic zone from $\mathrm{C} \cong 1$ to $\mathrm{C} \cong 3$;

3. $\mathrm{C}\,Y = p_m$ — the plastic zone is fully formed and the further increase in load no longer increases the mean pressure. Here, the mean pressure is equal to the hardness of the material. When the plastically deformed volume stops being constrained by the elastically deformed material, then material is buckled around the tip which is known as *pile-up* [110].

It is clear that the hardness can be defined only if the plastic zone is fully formed and then it is equal to the mean pressure.

10.5 Hardness

Historically, the first scale of hardness is the so-called Mohs hardness scale from 1812 [111], which was created on the basis of the scratch test where the harder material is able to scratch the softer one. According to the definition given by A. Martens, hardness is seen as resilience of a material against penetration of another material. Hardness is resistance to plastic deformation. However, this simple definition is inadequate, as it does not say anything how to quantify the hardness as a physical quantity. This was not possible before the indentation test came. The indentation hardness derived from the indentation test can define hardness as physical variable [112]. Hardness H is defined here as the proportion of applied load L and size of the deformed area of impression A as follows:

$$H = \frac{L}{A}. \tag{10.8}$$

10.5.1 Hardness models

Depending on what exactly we substitute for A in Eq. 10.8, we can have several hardness theories and models, each describing slightly different property.

The indentation hardness H_{IT} which is equal to the mean contact pressure, as described in the previous section, is defined as:

$$H_{IT} = \frac{L_{max}}{A_p} = \frac{L_{max}}{k_c h_c^2}, \tag{10.9}$$

where A_p is the projected area which is calculated from contact depth h_c and a constant k_c depending on the indenter geometry. The value of indentation hardness has a physical meaning of a mean contact pressure under the indenter and describes the resistance to plastic deformation. The second equation in Eq. 10.9 is correct only for perfectly sharp indenter (see Eq. 10.6); otherwise, it is necessary to use the equation for indenter shape correction (see Eq. 10.7).

A different approach is used in case of *plastic hardness* HU_{pl} which describes the plastic behaviour of the specimen and can be expressed as:

$$HU_{pl} = \frac{L_{max}}{A_d} = \frac{L_{max}}{\mathrm{k}h_p^2}. \tag{10.10}$$

Here the total area A_d (see Fig. 10.2) is used instead of projected area (the constant k = 26.43 for Vicker's indenter). The total area is calculated from h_p, i.e. the intercept of a tangent to unloading curve with the depth axis, which is the same as h_c value calculated by Oliver and Pharr method for $\epsilon = 1$ (see Eq. 10.7). This hardness model is mostly used in industry and for characterization of metallic specimens where the unloading curve can be fitted by linear function without the need of power law relation.

It is also possible to determine the hardness as a function of load and depth. This is how the *Marten's hardness* H_M is defined:

$$H_M = \frac{L}{A_d} = \frac{L}{\mathrm{k}h^2}. \tag{10.11}$$

If the $L = L_{max}$ and $h = h_{max}$, then Marten's hardness is equal to the *universal hardness HU*. It should be noted that the Marten's hardness describes the resistance to both elastic and plastic deformation mixed together.

A special case is the *differential hardness* H_{dif}, which is defined as the derivative of the applied load $\mathrm{d}L$ with respect to the contact area, which is dependent on h^2, as follows:

$$H_{dif} = \mathrm{const}\,\frac{\mathrm{d}L}{\mathrm{d}(h)^2}. \tag{10.12}$$

Differential hardness is calculated by numerical methods from the load-displacement curve during the nanoindentation test to provide information on the continuous deformation response of the material (plastic and elastic)

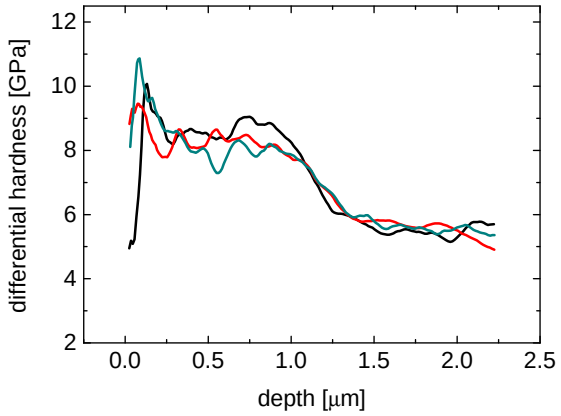

Figure 10.5: An example of three measurements of differential hardness. [117]

for a small change in applied load. It describes the momentary resistance of the material to deformation, on the other hand, the common hardness described in previous paragraphs integrates over all deformation states from the initial contact of the tip with the specimen to the actual depth [113,114]. Differential hardness measurement results in a continuous dependency of this hardness on depth. Sudden changes in differential hardness may result from events such as cracking or grain rearrangement. The initial few dozens of nanometres of depth are strongly affected by the microstructure of the coating or by the surface roughness because the deformed area is not yet large enough to avert potential local inhomogeneities such as grains in the case of nanocomposite material. From a change in the differential hardness curve it is also possible to recognize when mechanical properties of a substrate or an underlying layer affect the measurement, which is often associated with a gradual change of differential hardness curve [115, 116]. Figure 10.5 represents examples of such gradual shifts. Here, three differential curves represent three nanoindentation tests performed on a specimen containing a TiC (titanium carbide) thin film. Initial sequences at lower depths vary quite a lot, and for higher depths the measurements are more averaged due to larger distorted volume. From about 1 µm there is a decrease that is caused by the influence of the lower layer, in this case, a substrate on which the thin film was deposited. With this technique it is possible to find safe loads and indentation depths where the measured hardness is not affected by the unwanted influence of the substrate — in the case presented in Fig. 10.5 the safe indentation depth would be < 1 µm.

10.5.2 The influence of the substrate on measured hardness

Hardness is one of the most important material parameters of thin films but due to their small thickness, however its measured value is often influenced by the substrate itself and is not the real hardness of the thin film. One of the ways to find the hardness of a thin layer without the influence of a substrate is to use a nanoindentation test with a tip penetration of up to 10 % of the depth of the thin film. However, in the case of a very thin film, this option is sometimes impossible. In addition, there is a combination of substrates and thin films where not even 10 % of depth is sufficient because the substrate and the thin film have very different mechanical properties [110]. There are several models to separate the hardness of the thin film from the substrate or from lower layers in the multilayered system [118].

During the nanoindentation test performed into a thin film, the material at different depths under the indenter has a different effect on the resulting hardness value. Let us consider a small volume of material at depth h. Its contribution to the resulting hardness is proportional to two factors — the actual hardness $H(h)$ of the material in a given volume, and the *weighting coefficient* which determines the weight of the material hardness contribution at depth h on the measured result and which is also proportional to the distance from the point we measure. This weighting coefficient can be, for example, linear (Jonsson-Hogmark model) [119] or quadratic (Burnett-Page model) [120]. There are also different models considering cracks in a thin film emerging during the nanoindentation test, such as the Korsunsky's model [121], where one parameter determines whether the plastic deformation or the effect of the resulting cracks prevails.

10.6 Elastic modulus

The elastic modulus expresses the ability of the material to resist elastic deformation and is defined as the ratio of stress and strain. Depending on the type and direction of stress and deformation, we divide the elastic modulus into several types:

1. **Young's modulus** of elasticity is defined as the ratio of tensile stress and relative elongation of the body in the direction of applied stress. It is labelled as E and given in GPa.

2. **The shear modulus** is defined as the shear stress and shear deformation ratio. It is denoted as G and for isotropic materials it can be expressed using Young's modulus of elasticity and Poisson's ratio μ as:

$$G = \frac{E}{2(1+\mu)}; \tag{10.13}$$

3. **The bulk modulus**, denoted as K or B, represents the resistance of a material to uniform pressure. It is defined as the ratio of the increase of this pressure $\mathrm{d}p$ and the reduction of the volume $\mathrm{d}\,V$. Using Young's elastic modulus E and the Poisson's ratio μ, the bulk modulus can be expressed as:

$$B = \frac{E}{3(1-2\mu)}. \tag{10.14}$$

The modulus of elasticity in the case of thin films can be obtained by means of a nano-indentation measurement from the so-called contact stiffness S (see Eq. 10.2), which is obtained from fitting of the upper 60 % (in older literature 80 % [122]) part of the unloading curve with an assumption that first about 5 % of the curve length is not used for the fitting by default. According to the Eq. 10.2, the contact area A_p in which the contact stiffness is determined is required to calculate reduced modulus E_r. Thus, E_r is typically measured in the initial part of the unloading curve [112] as the contact area for evaluation of hardness is usually determined here as well.

From the reduced modulus using Eq. 10.1, it is possible to calculate *effective elastic modulus* E_{ef} and from it the Young's modulus E if the Poisson's ratio of the measured material μ_s is known. The effective elastic modulus of the specimen $E_{ef,s}$ is defined as:

$$E_{ef,s} = \frac{E_s}{1-\mu_s^2}, \tag{10.15}$$

where E_s is the Young's modulus of the specimen. The value of $E_{ef,s}$ describes better the elastic properties of the specimen itself than E_r because the later one characterize combined elastic properties of the specimen and the indenter. If the diamond indenter is used, the E_t and μ_t are 1140 GPa and 0.07, respectively, and it is easy to express the effective elastic modulus of the specimen from Eq. 10.1 as a function of the E_r which is the only variable.

10.7 Fracture toughness

Fracture toughness is defined as the critical stress intensity factor (K_{IC}) at which a brittle failure occurs. The stress intensity factor expresses the magnitude of the stress field at a given point around the crack and depends on the stresses due to external forces and the crack length. This dependency differs for different ways of applying external forces. It is true that malleable materials have higher fracture toughness than brittle materials of the same hardness because they can absorb energy in their plastic zone [123], i.e. it is harder to produce a crack since the material complies rather plastically.

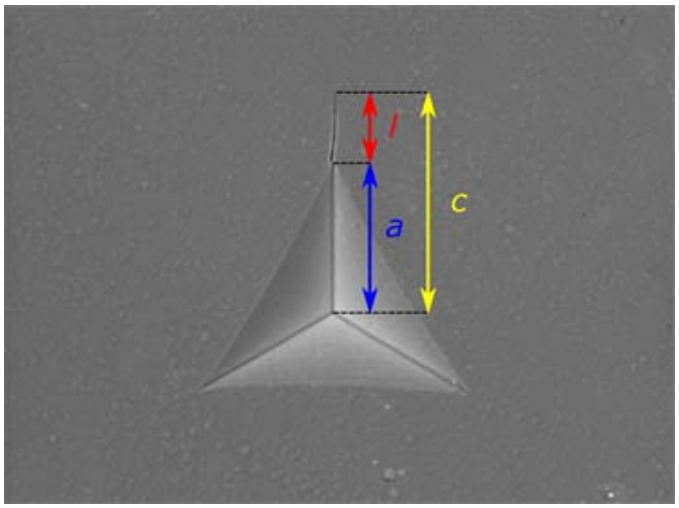

Figure 10.6: The image of a radial crack spreading from one indent corner including important length parameters that are necessary for the fracture toughness calculation.

The fracture toughness is calculated for the *plain strain* condition, which is difficult to achieve in the case of thin films as it imposes certain requirements, among other things, on their thickness [124]. There are several ways to determine fracture toughness of thin films using nanoindentation. The most common option is to measure the length of the radial crack c from the residual impression after the indentation test [125–128] and use the following equation which is applicable for the Berkovich tip:

$$K_{IC} = \chi_v \left(\frac{a}{l}\right)^{\frac{1}{2}} \left(\frac{E}{H}\right)^{\frac{2}{3}} \frac{L_{max}}{c^{\frac{3}{2}}}, \tag{10.16}$$

where c is the length of the radial crack measured from the indentation centre to the tip of the emanated cracks as shown in Fig. 10.6, a is the size of the residual indent made by Berkovich tip, l is the length of the emanated crack, E is the Young's modulus and H is the hardness. The parameter χ_v was determined by Ouchterlony [129] — for Berkovich tip it is equal to 0.016.

The Eq. 10.16 is suitable for calculating the fracture toughness of composite materials consisting of brittle and malleable phases [130]. The reliability of the measured fracture toughness values depends on the crack lengths and Eq. 10.16 works well only when cracks are shorter than 10 µm. Of course, it is necessary that the indentation measurement is not affected by the substrate (see section 10.5.2); otherwise, the obtained K_{IC} values do not represent the fracture toughness of the coating standalone but rather properties of the coating-substrate system as a whole.

10.8 Ratios of H/E and H^3/E^2

Mechanical properties such as fracture toughness or resilience are important parameters when studying thin films. For their at least approximate estimation in the case of ceramic materials, it is possible to use the results of the hardness measurement H and the effective elastic modulus E_{ef} [131] obtained from the nanoindentation test.

Several authors [132–135] show that the *fracture toughness* of the studied thin films depends on the H/E_{ef} ratio. By increasing the H/E_{ef} ratio, we can in many cases achieve high crack resistance. The low H/E_{ef} allows the applied load to be decomposed into a larger volume, inhibiting the formation of plastic deformation in the substrate and at the substrate-coating interface. This plastic deformation is the cause of tensile stresses and subsequent cracking at the interface.

The resilience of the material is defined as resistance to plastic deformation. This is the energy the material can hold before plastic deformation occurs. The *wear resistance* [133] is derived from the resilience which is related to the proportion of H^3/E_{ef}^2 where the higher proportion indicates higher resistance to wear.

10.9 Fischerscope measuring device

Fischerscope H100C XYp (see Fig. 10.7) is a computer-controlled measuring system with programable XY stage for automated testing and determination of material parameters according to ISO 14577 [136]. A Vickers or Berkovich pyramid is generally used as an indenter and is pressed into the material or coating whose parameters are to be determined. Without requiring special sample preparation, test specimens are positioned by hand and material parameters such as Martens hardness, Vickers hardness, differential hardness, plastic and elastic parts of the indentation work, effective elastic modulus or creep (determined after loading as well as unloading) are measured quickly and accurately.

10.9.1 Parameters and calibration

Key parameters of the measuring device are summarized in following points:

Measuring head

- load range: 0.4 — 1000 mN,
- load resolution: 0.02 mN,

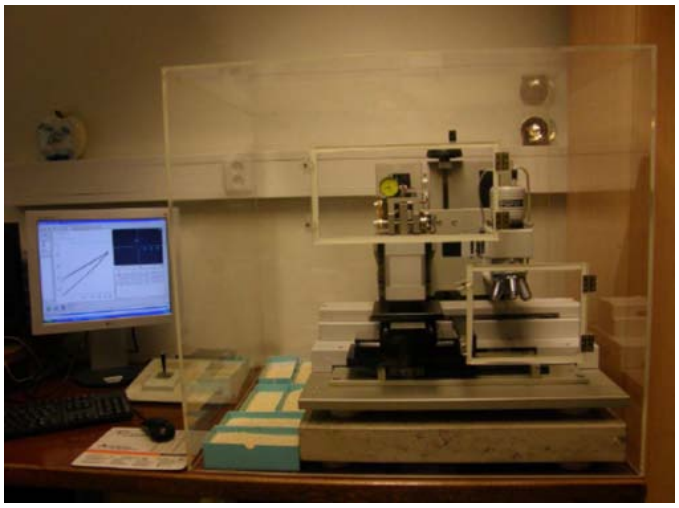

Figure 10.7: The image of the Fischerscope H100C XYp measuring device covered in a plastic box, with running WIN-HCU software on the screen. [117]

- maximum displacement: 700 µm,
- displacement resolution: 2 nm.

Positioning device and optics

- optical microscope with 40x, 200x and 400x magnification,
- programmable measuring stage 80 x 80 mm.

Prior to the measurement it is necessary to ensure that the indenter is free of any mechanical impurities, to check the measuring stage parallelism and to ensure that the indenter shape is well calibrated. For the indenter shape calibration, it is important to have a standardized sample which mechanical parameters are precisely known. One of the best candidate for indenter shape calibration in the case of Fischerscope H100C device is a certified boron silicate BK7 plate 5 x 5 x 1 cm with universal hardness of 4150 $\pm$ 80 MPa. If the measurement of universal hardness with the load of 300 mN fits in the error range of the universal hardness value of BK7, then the indenter shape calibration is not needed. Otherwise, the area function needs to be modified to obtain the correct universal hardness. In case of the Fischerscope H100C, the values of calibration constants C_j (see Eq. 10.7) are fixed and the contact depth h_c is corrected to a value of h_{corr} where the obtained universal hardness fits in the error range of the universal hardness value of BK7. The value of h_{corr} then represents virtually the correct contact depth as it would be for the perfect Berkovich or Vickers indenter (see Eq. 10.6). This value is then used for all calculations instead of the true h_c.

10.9.2 WIN-HCU software

The entire measurement process is controlled via WIN-HCU software. By using this software and the built-in optical microscope, it is possible to program multiple measurements or imprints with different loads. In Fig. 10.8 there is a print screen of the welcoming main window of this program where one may find all necessary buttons, bars and sub-menus. On the upper right-hand side of the window there is an optical microscope screen with magnification that is currently used, and x and y coordinates that serve as scales. With a small attached joystick, it is possible to move the stage in x and y axes and control the movement with the optical microscope screen. Below the optical screen there is a result table with measured and calculated parameters as Marten's, plastic or indentation hardness, ratio of the elastic work to total work done during one indentation test n_{IT}, effective elastic modulus, maximum depth, creep etc., which are related to a certain load chosen in a drop-down list located above. Selected as well as averaged values including standard errors and deviations, minima and maxima are generally shown in separated rows. All load-displacement curves measured with the chosen load are displayed in the middle graph â€“ by clicking on a curve, one can display corresponding parameters in the result table. It is also convenient to erase measurements that are wrong, i.e. due to imperfect contact with the surface of the specimen or due to unwanted cracking of the specimen; otherwise, their calculated values of parameters distort the averages in the result table. The measurement or set of programmed measurements can be started or aborted via buttons in the start bar located in the lower left-hand side of the main window. The magnification is changed manually directly on the attached microscope and, at the same time, it is convenient to change it also by the software — on the toolbar there is a corresponding icon for it. After changing the magnification via software, the displayed magnification and the scales on the optical microscope screen will change as well.

The whole measurement process is very simple: first, the desired spot is found on the specimen, then the load is chosen, and the single measurement can be performed just by one click. The X/Y programming of several following measurements can be done by clicking on the corresponding icon `X/Y-Programming` in the toolbar. In the programming window, there is possible to program individual measurements, line of measurements or matrices where it is necessary to set the first and the last point and number of points between. The selection is done by stage movement which can be done either by using the joystick, or mouse-clicking. Afterwards, the load is selected and by confirmation the programming is finished. After clicking back on the `Measurement Screen` icon in the toolbar, one may notice that the `Run` button in the start bar is now green and can be pressed. The `Run` button

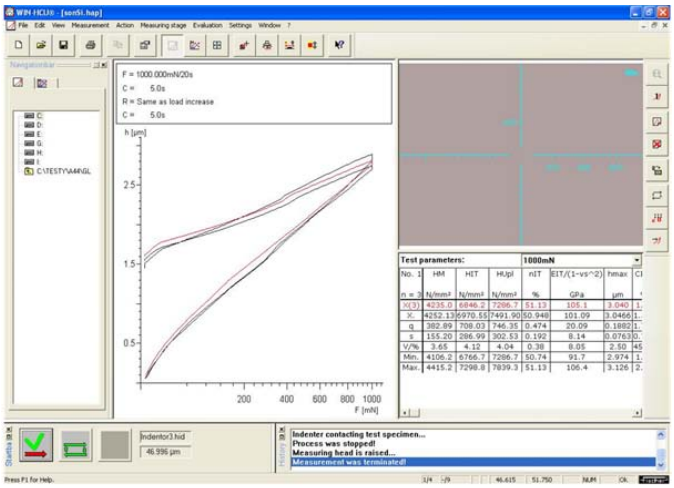

Figure 10.8: The print screen of the main window of WIN-HCU software.

serves for starting the programmed measurements whereas the `Start` button is for a single measurement by using a load chosen in the drop-down list in the right-hand side of the window.

After the measurement and evaluation is done, the data might be exported as Excel, text or ASCII files via `User-defined export` located on the measurement bar on the right-hand side. However, prior clicking on it, one needs to first set what exactly is to be exported and how. Click on `Settings` on the upper main bar, then go to `Options - User-defined export`. Here, ensure that `Settings of test parameters, Statistics of block, Characteristic material parameters - over all test parameters`, and `Excel` as a target are crossed, and confirm. Then, after clicking on the measurement bar the Excel file with exported data should open automatically.

Chapter 11

Advanced ellipsometry and spectrophotometry

Mgr. Daniel Franta, Ph.D., Mgr. Jiří Voháňka, Ph.D., Mgr. David Nečas, Ph.D.

11.1 Polarization of light and optical quantities

The properties of the light beams between the light sources, detectors, measured samples and optical elements of the real optical instruments can be effectively described using the formalism of the Stokes vectors and Mueller matrices [137]. This formalism allows us to describe the intensity and the polarization state of light but the information about the absolute phase is lost. Therefore, this formalism is usable for expressing the incoherent superposition of individual light beams falling onto the detector and for expressing the influence of the area non-uniformity of the measured samples, i.e. varying properties along the area of the samples.

The intensity and the polarization state of quasi-monochromatic light is completely specified by the Stokes vectors

$$\boldsymbol{S} = \begin{pmatrix} S_0 \\ S_1 \\ S_2 \\ S_3 \end{pmatrix} = \begin{pmatrix} I \\ I_{\parallel} - I_{\perp} \\ I_{+} - I_{-} \\ I_{\circlearrowright} - I_{\circlearrowleft} \end{pmatrix} , \tag{11.1}$$

where $I = I_{\parallel} + I_{\perp} = I_{+} + I_{-} = I_{\circlearrowright} + I_{\circlearrowleft}$ is the total intensity of light $I_{\parallel}$, $I_{\perp}$, I_{+}, I_{-}, $I_{\circlearrowright}$, $I_{\circlearrowleft}$ are the intensities measured after light passes through ideal polarizers for the following polarization states: $I_{\parallel}$ – linear polarization at angle 0Â° (i.e. in the reference direction), $I_{\perp}$ – linear polarization at angle 90Â°, I_{+} – linear polarization 45Â°, I_{-} – linear polarization -45Â°, $I_{\circlearrowright}$ – right circular polarization, $I_{\circlearrowleft}$ – left circular polarization.

From the Stokes vector it is possible to express other quantities describing the polarization of the light, for example the degree of polarization

$$P = \frac{1}{S_0}\sqrt{S_1^2 + S_2^2 + S_3^2}\ . \tag{11.2}$$

The changes in the intensity and the polarization state of the light beam after it is reflected from or transmitted through the linear optical system is then expressed by means of the matrix which relates the Stokes vector of the outgoing (i.e. reflected or transmitted) beam $\boldsymbol{S}_{\mathrm{out}}$ to the Stokes vector of the incident beam $\boldsymbol{S}_{\mathrm{in}}$:

$$\boldsymbol{S}_{\mathrm{out}} = \mathbf{M}\boldsymbol{S}_{\mathrm{in}}\ . \tag{11.3}$$

The matrix $\mathbf{M}$ is called the Mueller matrix. The optical quantities measured using the optical instruments, such as reflectance, transmittance and ellipsometric quantities can be expressed using the elements of this matrix.

Although the Mueller matrix has 16 elements, the number of independent elements is often much smaller. For simple systems which do not exhibit complicated combinations of effects such as anisotropy and depolarization a number of elements of the Mueller matrix vanishes or could be expressed using the other elements. In particular for reflection of light from the system of ideal isotropic thin films placed on semi-infinite substrate the Mueller matrix has only three independent elements. Although the real substrate is never semi-infinite, it is possible to view it as semi-infinite if the reflections from the back side do not have to be taken into account. This happens, for example, if the substrate is sufficiently absorbing or if the back-side is very rough.

The special system discussed above does not cause depolarization and it is possible to investigate the reflection of light independently for light polarized in the plane of incidence and light polarized perpendicular to the plane of incidence, i.e. for the p-polarization (from German *parallel* for parallel) and the s-polarization (from German *senkrecht* for perpendicular). The electric field corresponding to the p- and s-polarized light is depicted in figure 11.1. Therefore, it is possible to decompose light into the p-component and s-component, which are not mixed in the simplest case discussed here. This means that p-polarized light is reflected and refracted to p-polarized light and s-polarized light is reflected and refracted into s-polarized light. The relations between the complex amplitudes of the electric fields of the incident, reflected and refracted waves are expressed using the Fresnel reflection coefficients ($\hat{r}_{\mathrm{p}}$, $\hat{r}_{\mathrm{s}}$) and the transmission coefficients ($\hat{t}_{\mathrm{p}}$, $\hat{t}_{\mathrm{s}}$) for individual polarizations:

$$\hat{E}_{\mathrm{rp}} = \hat{r}_{\mathrm{p}}\hat{E}_{\mathrm{ip}}\ , \qquad \hat{E}_{\mathrm{rs}} = \hat{r}_{\mathrm{s}}\hat{E}_{\mathrm{is}}\ , \qquad \hat{E}_{\mathrm{tp}} = \hat{t}_{\mathrm{p}}\hat{E}_{\mathrm{ip}}\ , \qquad \hat{E}_{\mathrm{ts}} = \hat{t}_{\mathrm{s}}\hat{E}_{\mathrm{is}}\ . \tag{11.4}$$

The Mueller matrix describing the reflection from the system is then given

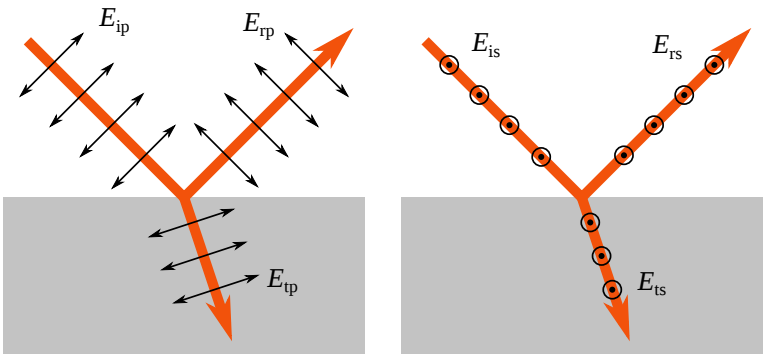

Figure 11.1: Schematic diagram of the electric field corresponding to the p- and s-polarized light.

as:

$$\mathbf{M} = \frac{1}{2}\begin{pmatrix} |\hat{r}_\mathrm{p}|^2 + |\hat{r}_\mathrm{s}|^2 & |\hat{r}_\mathrm{p}|^2 - |\hat{r}_\mathrm{s}|^2 & 0 & 0 \\ |\hat{r}_\mathrm{p}|^2 - |\hat{r}_\mathrm{s}|^2 & |\hat{r}_\mathrm{p}|^2 + |\hat{r}_\mathrm{s}|^2 & 0 & 0 \\ 0 & 0 & 2\Re(\hat{r}_\mathrm{p}\hat{r}_\mathrm{s}^*) & 2\Im(\hat{r}_\mathrm{p}\hat{r}_\mathrm{s}^*) \\ 0 & 0 & -2\Im(\hat{r}_\mathrm{p}\hat{r}_\mathrm{s}^*) & 2\Re(\hat{r}_\mathrm{p}\hat{r}_\mathrm{s}^*) \end{pmatrix} . \tag{11.5}$$

The reflectance of the sample, which is defined as the ratio of the intensity of reflected light I_r to the intensity of incident light I_0 (we assume that light is not polarized), is then equal to the element M_{00} of the Mueller matrix

$$R = \frac{I_\mathrm{r}}{I_0} = M_{00} = \frac{1}{2}(|\hat{r}_\mathrm{p}|^2 + |\hat{r}_\mathrm{s}|^2) . \tag{11.6}$$

This result is exactly what we expect since for unpolarized light the reflectance is given as the average $(R_\mathrm{p} + R_\mathrm{s})/2$ of the reflectances for the p- and s-polarized light ($R_\mathrm{p} = |\hat{r}_\mathrm{p}|^2$, $R_\mathrm{s} = |\hat{r}_\mathrm{s}|^2$).

While the reflectance describes the change of the intensity upon the reflection of light from the sample, the other two remaining quantities (recall that there are three independent elements of the Mueller matrix) describe the change in the polarization state. The ellipsometric ratio

$$\hat{\rho} = \hat{r}_\mathrm{p}/\hat{r}_\mathrm{s} , \tag{11.7}$$

is often used to describe the change in the polarization state. Since $\hat{\rho}$ is a complex number, it corresponds to two real quantities. The real quantities azimuth Ψ and the phase change Δ related to the ellipsometric ratio as

$$\tan\Psi \exp(\mathrm{i}\Delta) = \hat{r}_\mathrm{p}/\hat{r}_\mathrm{s} . \tag{11.8}$$

are also often used to describe the change in the polarization state.

The disadvantage of these quantities is that they are periodic, discontinuous and in some cases they can be infinite. Therefore, the changes in the polarization state that are close to each other from the physical point of view do not necessarily result in values of $\hat{\rho}$, Ψ and Δ lying close to each other. This may cause problems in processing of the experimental data. It is more practical to describe the changes in the polarization state using the elements of the normalized Mueller matrix, which is defined as the Mueller matrix divided by the reflectance R:

$$\mathbf{M} = R \begin{pmatrix} 1 & -I_{\mathrm{n}} & 0 & 0 \\ -I_{\mathrm{n}} & 1 & 0 & 0 \\ 0 & 0 & I_{\mathrm{c}} & I_{\mathrm{s}} \\ 0 & 0 & -I_{\mathrm{s}} & I_{\mathrm{c}} \end{pmatrix} . \tag{11.9}$$

The quantities I_{s}, I_{c} and I_{n} take values from the interval $[-1, 1]$ and the changes of the polarization states that are close to each other correspond to values lying close to each other. Since there are only two independent quantities describing the change in the polarization state only two of these quantities are independent. In particular it holds

$$I_{\mathrm{s}}^2 + I_{\mathrm{c}}^2 + I_{\mathrm{n}}^2 = 1 . \tag{11.10}$$

Another advantage of the quantities I_{s}, I_{c} and I_{n} is that they can be used even if the system exhibits depolarization, which can be caused, for example, by the reflection on the back sides of the substrates, area non-uniformity of the samples, etc. In this case the Mueller matrix has the same form as presented above but the ellipsometric quantities I_{s}, I_{c} and I_{n} represent three independent quantities constrained by the condition

$$I_{\mathrm{s}}^2 + I_{\mathrm{c}}^2 + I_{\mathrm{n}}^2 \hat{a} 1 . \tag{11.11}$$

In the ellipsometric literature, these quantities are often denoted by letters $S \equiv I_{\mathrm{s}}$, $C \equiv I_{\mathrm{c}}$ and $N \equiv I_{\mathrm{n}}$ (mostly by researchers using the Woollam instruments) or by symbols $I_{\mathrm{S}} \equiv I_{\mathrm{s}}$, $I_{\mathrm{CII}} \equiv I_{\mathrm{c}}$ and $I_{\mathrm{CIII}} \equiv I_{\mathrm{n}}$ (mostly by researchers using the Horiba, Jobin Yvon instruments).

The transmittance of the sample is defined as the ratio of the intensity of transmitted light I_{t} to the intensity of incident light I_0:

$$T = I_{\mathrm{t}}/I_0 . \tag{11.12}$$

It does not make sense to consider transmittance for the layered system on the semi-infinite substrate and, moreover, the reflections on the back side of the substrate must be taken into account.

If the substrate is transparent, then the reflectance (or transmittance) must be calculated as incoherent superposition the intensities corresponding to the

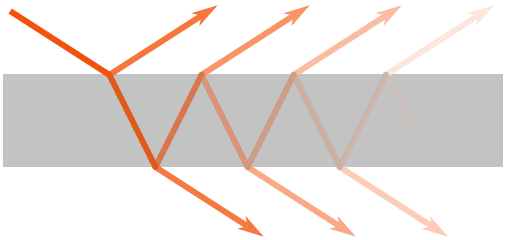

Figure 11.2: Summation scheme used for total reflectance or transmittance on the thick substrate.

situations in which there are zero, one, two, etc. reflections from the back side of the substrate. The contributions that must be summed together are depicted in figure 11.2. Let us denote: R_1 reflectance of the layered system on the upper (front) side of the substrate for light incident from top, R_1' reflectance of the layered system on the upper side of the substrate for light incident from bottom, R_2 reflectance of the layered system on the lower (back) side of the substrate for light incident from top, T_1 transmittance of the layered system on the upper side of the substrate for light incident from top, T_1' transmittance of the layered system on the upper side of the substrate for light incident from bottom, T_2 transmittance of the layered system on the lower side of the substrate and U transmittance of the substrate. The reflectance and transmittance of the whole system is then given as

$$R = R_1 + \frac{T_1 T_1' R_2 U^2}{1 - R_1' R_2 U^2}\,, \qquad T = \frac{T_1 T_2 U}{1 - R_1' R_2 U^2}\,. \tag{11.13}$$

If we want to calculate the Mueller matrices instead of reflectance and transmittance, then the same summation scheme can be used but it is necessary to replace the reflectances and transmittances with corresponding Mueller matrices:

$$\mathbf{R} = \mathbf{R}_1 + \mathbf{T}_1'(\mathbf{1} - U^2\mathbf{R}_2\mathbf{R}_1')^{-1}\mathbf{R}_2\mathbf{T}_1 U^2\,, \qquad \mathbf{T} = U\mathbf{T}_2(\mathbf{1} - U^2\mathbf{R}_1'\mathbf{R}_2)^{-1}\mathbf{T}_1\,. \tag{11.14}$$

When the above formulae were derived it was assumed that the Mueller matrix describing the attenuation of the light in the substrate is given as

$$\mathbf{U} = U\mathbf{1}, \qquad U = \exp\left(-\frac{4\pi d}{\lambda}\Im(\hat{n}\cos\hat{\theta})\right)\,, \tag{11.15}$$

where $\hat{n}$ is the complex refractive index of the media forming the substrate, $\hat{\theta}$ is complex refraction angle of the light traveling in the substrate, d is the thickness of the substrate and λ is the wavelength of light in vacuum. The Mueller matrices for transmitted light have the same form as for the reflected light (11.5) but with the reflection coefficients replaced by transmission coefficients.

11.2 Thin film systems

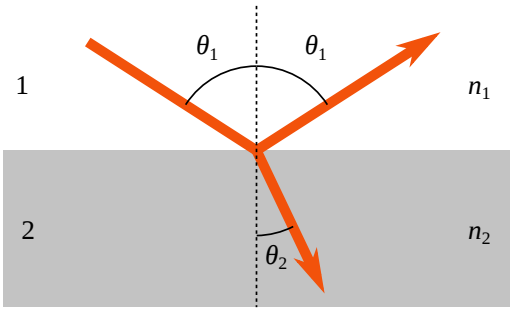

Figure 11.3: Schematic diagram of reflection and refraction of the light on single boundary.

In the optical characterization it is necessary to use the relations between the optical quantities and the properties of the materials, thicknesses of the films and other parameters.

First, we will look at the reflection and refraction of light on a boundary between two different isotropic media with refractive indices $\hat{n}_1$ and $\hat{n}_2$ (see figure 11.3). The incidence angle from the side of media 1 will be denoted $\hat{\theta}_1$. The refraction angle in the media 2 follows from the Snell's law

$$\hat{n}_1 \sin\hat{\theta}_1 = \hat{n}_2 \sin\hat{\theta}_2 \ . \tag{11.16}$$

It is evident that this law is transitive. Although the angles and refractive indices are complex quantities if the media are absorbing, the Snell's law and other formulae that will be introduced below take exactly the same form as for non-absorbing media.

The boundary conditions for the Maxwell equations can be used to derive the Fresnel coefficients for the reflection on the smooth boundary. The reflection coefficients for the p- and s-polarization are as follows

$$\hat{r}_\mathrm{p} = \frac{\hat{E}_\mathrm{rp}}{\hat{E}_\mathrm{ip}} = \frac{\hat{n}_2\cos\hat{\theta}_1 - \hat{n}_1\cos\hat{\theta}_2}{\hat{n}_2\cos\hat{\theta}_1 + \hat{n}_1\cos\hat{\theta}_2} \ , \qquad \hat{r}_\mathrm{s} = \frac{\hat{E}_\mathrm{rs}}{\hat{E}_\mathrm{is}} = \frac{\hat{n}_1\cos\hat{\theta}_1 - \hat{n}_2\cos\hat{\theta}_2}{\hat{n}_1\cos\hat{\theta}_1 + \hat{n}_2\cos\hat{\theta}_2} \ . \tag{11.17}$$

In the special case of normal incidence these formulae take especially simple form

$$\hat{r}_\mathrm{p} = -\hat{r}_\mathrm{s} = \frac{\hat{n}_2 - \hat{n}_1}{\hat{n}_2 + \hat{n}_1} \ . \tag{11.18}$$

The Fresnel transmission coefficients are given as

$$\hat{t}_\mathrm{p} = \frac{\hat{E}_\mathrm{tp}}{\hat{E}_\mathrm{ip}} = \frac{2\hat{n}_1\cos\hat{\theta}_1}{\hat{n}_2\cos\hat{\theta}_1 + \hat{n}_1\cos\hat{\theta}_2} \ , \qquad \hat{t}_\mathrm{s} = \frac{\hat{E}_\mathrm{ts}}{\hat{E}_\mathrm{ip}} = \frac{2\hat{n}_1\cos\hat{\theta}_1}{\hat{n}_1\cos\hat{\theta}_1 + \hat{n}_2\cos\hat{\theta}_2} \ . \tag{11.19}$$

For the normal incidence they can be written as:

$$\hat{t}_\mathrm{p} = \hat{t}_\mathrm{s} = \frac{\hat{n}_1}{\hat{n}_2 - \hat{n}_1} \ . \tag{11.20}$$

It is necessary to note that the ideal boundary between two media is almost never encountered in the real world. Therefore, it is often necessary to use more complicated models which take into account adsorbed layers or slight roughness of the boundaries. This is especially true for ellipsometry which is very sensitive to these effects.

In order to calculate the optical quantities of more complicated layered systems it is convenient to use the 4×4 matrix formalism (Yeh matrix formalism). In this formalism we work with four-dimensional complex vectors and with complex matrices relating these vectors. The components of the vectors correspond to amplitudes of four plane waves (there are two polarizations and two directions of propagation). Since this formalism works with amplitudes of the waves it is usable if the fields are summed coherently. Therefore, this formalism is usable for systems of thin films, where the interference effects must be taken into account. In this formalism the layered system is described by the matrix of the system, which relates the amplitudes of the waves on both sides of the system. For example, the matrix of the two-layer system with smooth boundaries is expressed as follows:

$$\hat{\mathbf{M}} = \hat{\mathbf{B}}(n_\mathrm{a}, \hat{n}_\mathrm{f1})\hat{\mathbf{T}}(\hat{n}_\mathrm{f1}, d_\mathrm{f1})\hat{\mathbf{B}}(\hat{n}_\mathrm{f1}, \hat{n}_\mathrm{f2})\hat{\mathbf{T}}(\hat{n}_\mathrm{f2}, d_\mathrm{f2})\hat{\mathbf{B}}(\hat{n}_\mathrm{f2}, \hat{n}_\mathrm{s}) \ , \tag{11.21}$$

where the arguments in the brackets indicate dependencies of the individual matrices on the complex refractive indices and thicknesses of the layers. The indices a, f1, f2, and s correspond to the ambient, first layer, second layer and substrate. In the case of smooth boundaries and homogeneous media the Yeh matrices are expressed as follows:

$$\mathbf{B}(\hat{n}_1, \hat{n}_2) = \begin{pmatrix} 1/\hat{t}_\mathrm{p} & \hat{r}_\mathrm{p}/\hat{t}_\mathrm{p} & 0 & 0 \\ \hat{r}_\mathrm{p}/\hat{t}_\mathrm{p} & 1/\hat{t}_\mathrm{p} & 0 & 0 \\ 0 & 0 & 1/\hat{t}_\mathrm{s} & \hat{r}_\mathrm{s}/\hat{t}_\mathrm{s} \\ 0 & 0 & \hat{r}_\mathrm{s}/\hat{t}_\mathrm{s} & 1/\hat{t}_\mathrm{s} \end{pmatrix} \tag{11.22}$$

and

$$\mathbf{T}(\hat{n}, d) = \begin{pmatrix} \exp(\mathrm{i}\hat{X}) & 0 & 0 & 0 \\ 0 & \exp(-\mathrm{i}\hat{X}) & 0 & 0 \\ 0 & 0 & \exp(\mathrm{i}\hat{X}) & 0 \\ 0 & 0 & 0 & \exp(-\mathrm{i}\hat{X}) \end{pmatrix} \ , \tag{11.23}$$

where

$$\hat{X} = \frac{2\pi}{\lambda}\, d\, \hat{n}\, \cos\hat{\theta} \ . \tag{11.24}$$

It is also possible to include anisotropy or various defects, such as roughness, inhomogeneity, etc., into this 4×4 matrix formalism. The concrete forms of the matrices for anisotropic media or mentioned defects can be found in literature [137, 138].

11.3 Universal dispersion models

If the aim of the optical characterization is more than determination of the refractive index in the transparent region and the thickness of the layer, it is necessary to perform the optical characterization in a wide spectral range. In this case the absorption caused by excitations of electrons, i.e. in the visible and ultraviolet ranges, as well as the absorption caused by vibrations of the atomic lattice, i.e. in the phonon absorption in the infrared region, must be taken into account. A suitable dispersion model describing the mentioned absorption processes must be used for the optical characterization. In the program *newAD2* it is possible to use the dispersion model called the Universal Dispersion Model (UDM) [139], which provides the means to describe the dielectric response of almost all materials.

The description of the UDM model and its use in the *newAD2* software can be found at `newad.physics.muni.cz`.

11.4 Spectroscopic ellipsomety

Ellipsometry is an optical technique, in which the changes in the polarization state of light upon reflection or transmission by the sample are measured. The instrument used for these measurements is called ellipsometer.

Within ellipsometry we distinguish several techniques differing in the construction of the used instruments and the quantities that can be measured. The number of the measured quantities is in the range from two (e.g. Δ and Ψ) to fifteen (i.e. all the elements of the normalized Mueller matrix).

All types of ellipsometers contain polarizers in the optical path before and after the sample. The one before the sample is called polarizer while the one after the sample is called analyzer. Most types of ellipsometers also contain one or more compensators (optical elements shifting the phase between the waves corresponding to two mutually perpendicular directions). By analyzing the dependence of the intensity of the detected light on the on the rotation angles of the optical elements or changes of their parameters it is possible to determine how the sample changes the polarization state of the light (see figure 11.4).

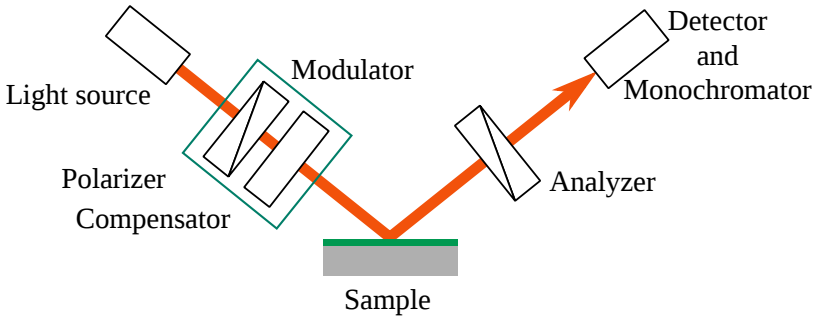

Figure 11.4: Shematic diagram of ellipsometers in PCSA (polariser–compensator–sample–analyser) configuration.

11.5 Spectrophotometry

The spectrophotometers can be constructed as one-channel or two-channel instruments. The schematic diagram of the two-channel spectrophotometer is depicted in figure 11.5. In two-channel instruments the light beam between the light source and the detector is divided into two paths using appropriate beamsplitter, the first path corresponds to the sample channel and the second path corresponds to the reference channel. Both channels use the same detector and the channel measured at a given time is chosen for example by using the rotating mirrors as beamsplitter to select appropriate path of the light beam. Two measurements are performed on the sample channel. The first measurement is performed for the investigated sample and the second measurement is performed for the normal (i.e. sample with known reflectivity). The silicon single crystal in the UV–VIS range and gold plated sample in the NIR range are often used. Therefore, we measure the relative reflectance of the sample with respect to the normal. The reference channel is used to compensate for the fluctuations in the intensity of the light source and sensitivity of the detector. The sample with arbitrary reflectivity (usually identical with the normal) is placed in this channel. The following relations hold for the intensities I_{v}, I_{n} measured on the sample channel and the intensities $I_{\mathrm{r}1}$, $I_{\mathrm{r}2}$ measured on the reference channel:

$$I_{\mathrm{v}} = R_{\mathrm{v}} Z_1 D_1 G_{\mathrm{v}} \,, \qquad I_{r1} = R_{\mathrm{r}} Z_1 D_1 G_{\mathrm{r}} \,, \tag{11.25}$$

$$I_{\mathrm{n}} = R_{\mathrm{n}} Z_2 D_2 G_{\mathrm{n}} \,, \qquad I_{r2} = R_{\mathrm{r}} Z_2 D_2 G_{\mathrm{r}} \,, \tag{11.26}$$

where R_{v}, R_{n} and R_{r} are the reflectances of the sample, normal and reference, respectively. The symbols $Z_{1,2}$ denote the intensity of the light source at the time of measurement, the symbols $D_{1,2}$ denote the sensitivity of the detectors at the time of measurement and G_{v}, G_{n}, G_{r} are geometrical factors for individual channels which take into account different positions of the samples and they also include different technical realization of these channels. If the channels are switched sufficiently fast during one measurement,

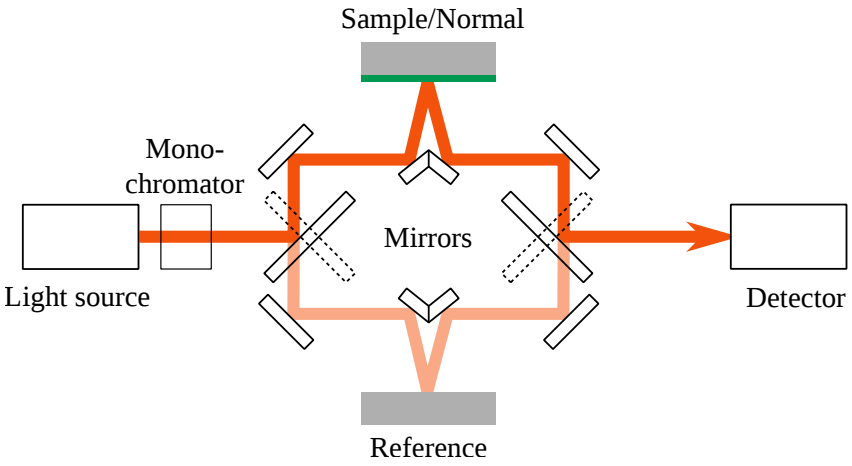

Figure 11.5: Shematic diagram of two-channel spectrophotometers.

it is possible to neglect the fluctuations in the intensity of the light source and the sensitivity of the detector (i.e. D a Z are the same for both the channels but different for subsequent measurements).

By combining the above relations we obtain

$$\frac{R_\mathrm{v}}{R_\mathrm{n}} = \frac{\dfrac{I_\mathrm{v}}{I_\mathrm{r1}}}{\dfrac{I_\mathrm{n}}{I_\mathrm{r2}}} \frac{G_\mathrm{n}}{G_\mathrm{v}} = R_\mathrm{rel} \,. \tag{11.27}$$

The factors corresponding to fluctuations of the light source and the detector were canceled and, moreover, it is reasonable to assume that the ratio $G_\mathrm{v}/G_\mathrm{n}$ is very close to unity, since it relates factors for the same channel (only the measured samples are different). The reflectance of the sample is then calculated as

$$R_\mathrm{v} = R_\mathrm{rel} R_\mathrm{n} \,. \tag{11.28}$$

The measurement of the transmittance using the two-channel spectrophotometer is almost identical to measurement of the reflectance. The only difference is that an empty channel (corresponding to 100% transmittance) is used instead of the reference sample. Therefore, the measurement of transmittance does not require the knowledge of the reflectance of the reference.

11.6 FTIR - Fourier Transform InfraRed

FTIR (Fourier Transform InfraRed) is a method for measuring spectrophotometric and ellipsometric quantities in the infrared region.

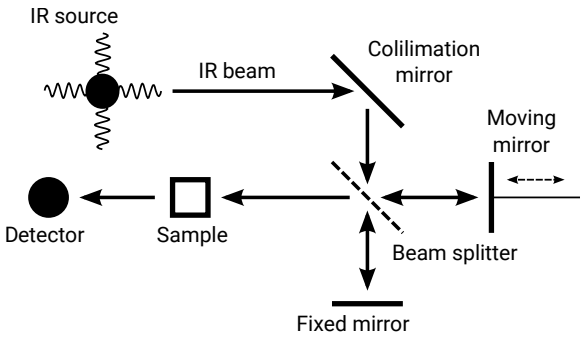

Figure 11.6: Schematic diagram of the Michelson interferometers for FTIR measurements.

The FTIR instrument does not contain monochromator. Instead, it uses the Michelson interferometer (see figure 11.6) and the output of the measurement is interferogram (the dependence of the intensity of the detected radiation on the position of the mirror in the interferometer). The spectral dependence of the intensity is obtained from the interferogram using the Fourier transform.

Bibliography

[1] R.F. Bunshah, (Ed.) *Handbook of Deposition Technologies for Films and Coatings: Science, Technology and Applications*. 2nd ed. Park Ridge: Noyes Publications, 1994. 888 p. ISBN 0-12-533026-X

[2] P. Sigmind, *Nucl. Instrum. Meth. B* 27/1-2 (1987) 1

[3] R.A. Powell, S. Rossnagel, (Eds.) *PVD for Microelectronics: Sputter Deposition Applied to Semiconductor Manufactoring*. San Diego: Academic Press, 1999. 420 p. ISBN 0-8155-1337-2

[4] K. Besocke, S. Berger, W.O. Hofer, U. Littmark, *Radiat. Eff.* 66 (1982) 35

[5] W.O. Hofer, K. Besocke, B. Stritzker, *Appl. Phys. A* 30/2 (1983) 83

[6] Y. Yamamura, H. Tawara. *Atomic and Nuclear Data Tables*. Academic Press, vol. 62, 1996.

[7] O.A. Fouad, A.K. Rumaiz, S.I. Shah, *Thin Solid Films*. 517/19 (2009) 5689

[8] J.F. Ziegler, *Particle Interactions with Matter*. http://www.srim.org/, Cited July 15th, 2013.

[9] W.M. Posadowski, *Vacuum* 46/8-10 (1995) 1017

[10] J. Fu, P. Ding, F. Dorleans, Z. Xu, F. Chen, *J. Vac. Sci. Technol. A*. 17/5 (1999) 2830

[11] A. Anders, J. Andersson, A. Ehiasarian, *J. Appl. Phys.* 102 (2007) 113303-1

[12] D. Depla, S. Mahieu, (Eds.). *Reactive Sputter Deposition*. Springer Berlin Heidelberg, 2008, ISBN 978-3-540-76664-3

[13] T. Motohiro, Y. Taga, *Thin Solid Films* 112/2 (1984) 161

[14] G.M. Turner, I.S. Falconer, B.W. James, D.R. McKenzie, *J. Appl. Phys.* 65 (1989) 3671

[15] S.M. Rossnagel, *J. Vac. Sci. Technol. A* 6 (1988) 19

[16] G.M. Turner, *J. Vac. Sci. Technol. A*. 13/4 (1995) 2161

[17] F.J. Jimenez, S.K. Dew, *J. Vac. Sci. Technol. A*. 30/4 (2012) 041302

[18] C. Huo, M.A. Raadu, D. Lundin, J.T. Gudmundsson, A. Anders, N. Brenning, *Plasma Sources Sci. Technol.* 21 (2012) 045004

[19] N. Brenning, D. Lundin, M. A. Raadu, C. Huo, C. Vitelaru, G. D. Stancu, T. Minea, and U. Helmersson, *Plasma Sources Sci. Technol.* 21 (2012) 025005

[20] F. Mitschker, M. Prenzel, J. Benedikt, C. Maszl, A. von Keudell, *J. Phys. D: Appl. Phys.* 46 (2013) 155204

[21] N. Hardy, *Planar Magnetrons In PVD Coatings: Essential Basics.* http://www.semicore.com/ news/ 50-planar-magnetron-pvd-coating, Cited July 22nd, 2013.

[22] D.L. Smith, *Thin Film Deposition: Principles & Practice.* McGraw-Hill, New York, 1995

[23] R.S. Rastogi, V.D. Vankar, K.L. Chopra, *Rev. Sci. Instrum.* 58/8 (1987) 1505

[24] *Gencoa high yield magnetic option.* hhttp://www.gencoa.com/ hy_high_yield_rectangular_magnetron/ index.asp, Cited July 22nd, 2013.

[25] *The ONYX-Revolution: Angstrom Sciences — Cylindrical Magnetrons.* www.angstromsciences.com, Cited July 22nd, 2013.

[26] P.S. McLeod, L.D. Hartsough, J. Vac. Sci. Technol. 14(1) (1977) 263

[27] R.K. Waits, J. Vac. Sci. Technol. 15(2) (1978) 179

[28] P.J. Kelly, R.D. Arnell *Vacuum* 56 (2000) 159

[29] B. Window, N. Savvides, J. Vac. Sci. Technol. A 4(2) (1986) 196

[30] K.L. Chopra, *Thin film phenomena*, McGRAW-HILL book company USA, 1969

[31] R.V. Stuart, *Vacuum Technology, thin films and sputtering*, Academic press, 1983, ISBN 0-12-674780-6

[32] D.M. Mattox, *Handbook of Physical Vapor Deposition (PVD) Processing*, Elsevier Inc. , 2010, ISBN 978-0-8155-2037-5

[33] H.O. Pierson, *Handbook of Chemical Vapor Deposition (CVD)*. Noyes Publications,Park Ridge, New Jersey, U.S.A., 1992

[34] M.A. Lieberman, A.J. Lichtenberg, *Principles of Plasma Discharges and Material Processing*.Second Edition, Wiley, 2005

[35] L. Martinu, O. Zabeida and J.E. Klemberg-Sapieha, *Plasma Enhanced Chemical Vapor Deposition of Functional Coatings.In Handbook of Deposition Technologies for Films and Coatings*, Third Edition,*Science, Applications and Technology* (2010), 392

[36] L. Martinu, J.E. Klemberg-Sapieha, O.M. Kuettel, A. Raveh, M.R. Wertheimer, *J. Vac. Sci. Technol.* A 12 (1994) 1360

[37] K. Kohler, D.E. Horne, J.W. Coburn, *J. Appl. Phys.* 58 (1985), 3350

[38] R.N. Franklin, *J. Phys. D: Appl. Phys.* 36 (2003) R309

[39] A.Stoica, *Preparation of nanostructured carbon films by Plasma Enhanced Chemical Vapor Deposition* ,Dissertation work, Masaryk University, Brno, 2012

[40] M. V. Alves, M. A. Lieberman, V. Vahedi, and C. K. Birdsall, *J. Appl. Phys.* 69/7 (1991) 3823

[41] C. Corbella Roca. *Thin film structures of diamond-like carbon prepared by pulsed plasma techniques.* PhD dissertation. Universitat de Barcelona, 2005

[42] L. Körner, *Diffusion Barrier Coatings for Polymer Containers processed by Plasma Enhanced Chemical Vapor Deposition* PhD dissertation. Eidgenössische Technische Hochschule â€“ ETH Zürich 2010

[43] R.d´Agostino, P. Favia, F. Fracassi, *Plasma Processing of Polymers*, Kluwer Academic Publishers, The Netherlands, 1997

[44] J. Goldstein, D. E. Newbury, D. C. Joy, C. E. Lyman, P. Echlin, E. Lifshin, L. Sawyer, J. R. Michael, *Scanning Electron Microscopy and X-Ray Analysis*, Kluwer, NY, 2003

[45] P. B. Hirsch, *Electron Microscopy of Thin Crystals*, Butterworths, Washington, 1965 or later edition

[46] C. W. Oatley, *The Scanning Electron Microscope, part 1: The Instrument.*, Cambridge University Press, 1972

[47] L. Reimer, *Scanning Electron Microscopy*, Springer, 1998

[48] *Handbook of Charged Particle Optics*, Ed. J. Orloff, CRC Press, 1997

[49] V. Hulínský, K. Jurek, *Zkoumání látek elektronovým paprskem*, SNTL Praha, 1982

[50] Tescan, *Mira 3*. https://www.tescan.com/en-us/technology/sem/mira3

[51] Quorum Technologies, *Q150R Rotary-Pumped Sputter Coater/Carbon Coater*.
https://www.quorumtech.com/quorum-product/q150r-rotary-pumped-sputter-coatercarbon-coater

[52] Oxford Instruments, *Oxford Instruments NanoAnalysis*.
https://www.oxford-instruments.com/products/microanalysis/energy-dispersive-x-ray-systems-eds-edx,
https://www.oxford-instruments.com/products/microanalysis/wavelength-dispersive-systems-wds

[53] JEOL, *Scanning Electron Microscope A To Z*.
https://www.jeol.co.jp/en/applications/pdf/sm/sem_atoz_all.pdf

[54] ThermoFischer Scientific, *Electron Microscopy*.
https://www.thermofisher.com/cz/en/home/industrial/electron-microscopy.html,
https://www.fei.com/introduction-to-electron-microscopy/

[55] GlobalSino, *Practical Electron Microscopy*.
http://www.globalsino.com/EM/

[56] Ústav přístrojové techniky Brno, *Podzimní škola elektronové mikroskopie*.
https://www.isibrno.cz/cs/podzimni-skola-zakladu-elektronove-mikroskopie-2017

[57] B.L. Dutrow, X-ray Powder Diffraction (XRD), https://serc.carleton.edu/research_education/geochemsheets/techniques/XRD.html

[58] PRAKTIKUM Z PEVNYCH LATEK (1B) — F6390, http://www.physics.muni.cz/ufkl/Vyuka/Praktika/F6390-PraktikumFPL-Navody-2018.pdf

[59] G. Binnig, C.F. Quate, and Ch. Gerber **Phys. Rev. Lett.** 56 (1986) 930

[60] https://warwick.ac.uk/fac/sci/physics/current/postgraduate/regs/mpagswarwick/ex5/techniques/structural/afm/

[61] G. Fantner, Advanced bioengineering methods, Atomic Force Microscopy, https://lbni.epfl.ch/

[62] P. Klapetek, *Quantitative Data Processing in Scanning Probe Microscopy.* SPM Applications for Nanometrology, A volume in Micro and Nano Technologies, 2013

[63] https://www.ntmdt-si.com/resources/spm-principles

[64] S. Magonov, J. Alexander, and S. Wu *Advancing characterization of materials with Atomic Force Microscopy - based electric techniques* In Scanning Probe Microscopy of Functional Materials: Nanoscale Imaging and Spectroscopy; Kalinin, S. V.; Gruverman, A., Eds.; Springer: Berlin, Germany, (2010) 33.

[65] X-ray diffraction, Rigaku corporation, www.rigaku.com/en/techniques/xrd

[66] S.A. Speakman, Basics of X-Ray Powder Diffraction, http://prism.mit.edu/xray

[67] P. Scherrer, Bestimmung der Groesse und der inneren Struktur von Kolloidteilchen mittels Roentgenstrahlen, Nachr. Ges. Wiss. Goettingen 26 (1918) 98-100

[68] http://www.eagle-regpot.eu/EAgLE-Equipment_XPS.html

[69] C.J. Powell, A. Jablonski, S. Tanuma et al. J. Electron Spectrosc. Relat. Phenom, 68, (1994)

[70] D. F. Mitchell, K. B. Clark, W. N. Lennard, et al. Surf. Interface Anal, 21 (1994) 44

[71] B. Hergelova, A. Zahoranova, D. Kovacik, et al. Open Chemistry, 13 (2015) 564

[72] P. Willmott, An Introduction to Synchrotron Radiation — Techniques and Applications, J. Wiley & Sons Ltd., 2011.

[73] V. Prysiazhnyi, M. Stupavska, C. Kleber et al. Surf. Coat. Technol., 258 (2014) 1082

[74] http://www.rjlg.com/2014/12/polystyrene-manufacturing-issues/

[75] https://xpssimplified.com/

[76] J. Y. Lee, D. W. Kim, W. S. Kang, J. O. Lee, M Hur, S. H. Han, J. Phys. D: Appl. Phys. 51 (2017) 9

[77] N. Winograd, S. W. Gaarenstroom, Physical methods in modern chemical analysis, vol. 2, Academic Press, New York, (1980)

[78] Surface Analysis — the Principal Techniques, John Wiley & Sons (1997).

[79] D. Briggs, M. Seah, Practical surface analysis, John Wiley & Sons (1990).

[80] D. Briggs, J. T. Grant, Surface analysis by Auger and X-Ray Photoelectron Spectroscopy, IM Publications, (2003)

[81] https://www.phi.com/surface-analysis-techniques/xps-esca.html

[82] Raman Spectroscopy — A Tutorial, http://www.kosi.com/na_en/products/raman-spectroscopy/raman-technical-resources/raman-tutorial.php

[83] What is Raman Spectroscopy?, https://www.nanophoton.net/raman/raman-spectroscopy.html

[84] S.M. Leeds, Characterisation of the Gas-Phase Environment in a Microwave Plasma Enhanced Diamond Chemical Vapour Deposition Reactor using Molecular Beam Mass Spectrometry, 1999, http://www.chm.bris.ac.uk/pt/diamond/stuthesis/chapter2.htm

[85] V. Bursikova, P. Stahel, Z. Navratil, J. Bursik, J. Janca, *Surface energy evaluation of plasma treated materials by contact angle measurement* Masaryk University, Brno, 2004

[86] R.J. Good and C. J. van Oss, *Modern Approaches to Wettability: Theory and Applications* Eds: M. E. Schrader, and G. Loeb, Plenum Press, New York, 1992

[87] W.A. Zisman,*Handbook of Adhesives* Skeist, I., Ed: van Nostrand, NewYork, Chapter 3, 1977

[88] F. M. Fowkes,*Industrial and Engineering Chemistry* 56/12, 40, 1964

[89] , F.M. Fowkes, *J. of Adhesion*, 4, 153, 1972.

[90] A.W. Neumann and R. J. Good,*Techniques of Measuring Contact Angles*, In *Surface and Colloid Science*, Volume II, Experimental Methods, Eds: R.J. Good and R. R. Stromberg, Plenum Pres, New York, 1979. [Oss] C.J. van Oss,*Interfacial Forces in Aqueous Media* Marcel Decker Inc., New York, 1994.

[91] D. Berthelot, *Comp. Rend. Acad. Sci.*, 126, 1703, 1898.

[92] D.Y. Kwok and A.W. Neumann *Adv. Coll. Inter. Sci.* 81 (1999), p. 167.

[93] G. Antonow *J. Chem. Phys.* 5 (1907), p. 372.

[94] D.K. Owens and R.C. Wendt *J. Appl. Pol. Sci.* 13 (1969), p. 1714.

[95] F.M. Fowkes In: *Physico-chemical Aspects of Polymer Surfaces* vol. 2, Plenum, K.L. Mittal, Editor, New York (1983).

[96] S. Wu *Polymer Interface and Adhesion*, Marcel Dekker, New York (1982).

[97] E.N. Dalal *Langmuir* 3 (1987), p. 1009. Inter. Sci. 49 (1974), p. 291.

[98] L.A. Girifalco and R.J. Good *J. Phys. Chem.* 61 (1957), p. 904.

[99] D. Li and A.W. Neumann *J. Colloid Interface Sci.*137 (1990), p. 304.

[100] D.Y. Kwok and A.W. Neumann *Coll. Surf.* A 161 (2000),31

[101] P.K. Sharma, K. Hanumantha Rao, K.S.E. Forssberg and K.A. Natarajan *Int. J. Miner. Proc.* 62 (2001), p. 3.

[102] I.N. Sneddon, Proc. Cambridge Philos. Soc. (1948), 492-507

[103] I.N. Sneddon, Int. J. Eng. Sci. 3 (1965), 47-57

[104] FISCHER-CRIPPS, A. C. (2011). *Nanoindentation* (3th ed.). New York: Springer

[105] W.C. Oliver, G.M. Pharr, J. Mater. Res. 7 (1992), 1564

[106] W.C. Oliver, G.M. Pharr, J. Mater. Res. 19 (2004), 3

[107] M.F. Doerner, W.D. Nix, J. Mater. Res. 1 (1986), 601

[108] D. Tabor, Review of Physics in Technology 1 (1970), 145

[109] D. Tabor, Philos. Mag. A 74 (1996), 1207

[110] MANN, A. B. (2005). Nanomechanical Properties of Solid Surfaces and Thin Films, in B. BHUSHAN (Ed.), Nanotribology and Nanomechanics, An Introduction. Berlin, Nemecko: Springer.

[111] H. King, *Mohs hardness scale*, http://geology.com/minerals/mohs-hardness-scale.shtml

[112] B. Wolf, Crystal Research and Technology 35 (2000), 377

[113] B. Wolf, B. Wolf, A. Richter, New J. Phys. 5 (2003), 15.1

[114] B. Wolf, Phil. Mag. Phil. Mag. Lett. 86 (2006), 5251

[115] L. Zabransky, V. Bursikova, P. Soucek, P. Vasina, T. Gardelka, P. Stahel, O. Caha, V. Perina, J. Bursik, Surf. Coat. Tech. 242 (2014) 62

[116] L. Zabransky, V. Bursikova, J. Daniel, P. Soucek, P. Vasina, J. Dugacek, P. Stahel, O. Caha, J. Bursik, V. Perina, Surf. Coat. Tech. 267 (2015), 32

[117] ZABRANSKY, L. (2017). Studium mechanickych vlastnosti a mikrostruktury tvrdych ochrannych vrstev na bazi uhliku [dizertacni prace]. Masarykova Univerzita, Brno, Ceska republika

[118] J.L. He, W.Z. Li, H.D. Li, Appl. Phys. Lett. 69 (1996), 1402

[119] B. Jonsson, S. Hogmark, Thin Solid Films114 (1984), 257

[120] P. J. Burnett, T. F. Page, J. Mater. Sci.19 (1984), 845

[121] A.M. Korsunsky, M.R. McGurk, S.J. Bull, T.F. Page, Surf. Coat. Tech. 99 (1998), 171

[122] A.C. Fischer-Cripps, P. Karvankova, S. Veprek, Surf. Coat. Tech. 200 (2006), 5645

[123] FISCHER-CRIPPS, A.C. (2000). *Introduction to Contact Mechanics*. Springer, Berlin, 2000

[124] S. Zhang, X. Zhang, Thin Solid Films 520 (2012), 2375

[125] B.R. Lawn, A.G. Evans, J. Am. Cer. Soc. 63 (1980), 574

[126] BROEK, D. (1997). *Elementary Engineering Fracture Mechanics*, Kluwer Academic Publishers, Dordrecht, 1997

[127] M.T. Laugier, J. Mater. Sci. Lett. 6 (1987), 897

[128] G.R. Anstis, P. Chantikul, B.R. Lawn, D.B. Marshall, J. Am. Cer. Soc. 64 (1981), 533

[129] F. Ouchterlony, Eng. Fract. Mech. 8 (1976), 447

[130] J.J. Guo, K. Wang, T. Fujita, J.W. McCauley, J.P. Singh, M.W. Chen, Acta Mater. 59 (2011), 1671

[131] KOHOUT, J., (2013). Nanokrystalicke multikomponentni vrstvy pripravene pulzim magnetronovym naprasovanim [dizertacni prae]. Zapadoceska univerzita v Plzni, Plzen, Ceska republika

[132] D. Martinez-Martinez, C. Lopez-Cartes, A. Fernandez, J.C. Sanchez-Lopez, Thin Solid Films 517 (2009), 1662

[133] D. Galvan, Y.T. Pei, J.Th.M. De Hosson, Surf. Coat. Tech. 201 (2006), 590

[134] A. Leyland, A. Matthews, Wear 246 (2000), 1

[135] A. Leyland, A. Matthews, Surf. Coat. Tech. 177-178 (2004), 317

[136] https://www.iso.org/standard/56626.html

[137] I. Ohlídal, J. Vohánka, Martin Čermák, D. Franta, *Ellipsometry of Layered Systems*, in: Optical Characterization of Thin Solid Films **64**, ed. O. Stenzel and M. Ohlídal, Springer, 2018, 233–267.

[138] I. Ohlídal, D. Franta, *Ellipsometry of Thin Film Systems*, in: Progress in Optics **41**, ed. E. Wolf, Elsevier, 2000, 181–282.

[139] D. Franta and J. Vohánka and M. Čermák, *Universal dispersion model for characterization of thin films over wide spectral range*, in: Optical Characterization of Thin Solid Films **64**, ed. O. Stenzel and M. Ohlídal, Springer, 2018, 31–82.